EURAC research

UNIVERSITÀ DEGLI STUDI DI PADOVA

DIPARTIMENTO DI INGEGNERIA INDUSTRIALE

in cooperation with

EURAC research
Institute for Renewable Energy

Elaboration of the physical model of an air-to-water heat exchanger under condensing and frosting conditions

Author:	Simone Dugaria
Supervisor:	Prof. Michele De Carli
Co-Examiner:	Dott. Ing. Matteo D'Antoni
	Dott. Ing. Roberto Fedrizzi

Bolzano, April 2014

Abstract

In this thesis, a numerical model for coupled heat and mass transfer with condensation and frost accumulation on a fin-and-tube, air-to-water heat exchanger is presented and validated.

During indirect heating of water stream with external surface temperature below the dew point of the air flow, the water vapour contained in the air-stream condensates on the surface. Condensation may result in an overall enhancement of the thermal performance of the heat exchanger, mainly because latent heat transfer is involved. In most cases surface temperature is also below the frost point of air and as a consequence, the water vapour will be deposited on the surface as a porous layer of ice crystals. Frost growth on heat exchanger surfaces affects the thermal performance of heat exchangers in several ways: it increases the thermal resistance between the fin and airflow and decrease the cooling capacity of heat exchangers; it also reduces the airflow and increase the air pressure drop through the heat exchangers.

To determine the thermal performance of the heat exchanger under variable winter conditions, it is essential to develop a detailed computational model capable of computing sensible and latent heat transfer rates under transient boundary conditions. The model should be also able to calculate the energy consumption of the coupled heat exchanger-fan system under variable weather and load conditions, involving different degree of water-vapour condensation and frost formation.

In order to establish the physical relationship on which the numerical model will be based, simultaneous heat and mass transfer model will be implemented. It will be capable to calculate sensible and latent heat rates, outlet water temperature, as well as fan power consumption of a sized heat exchanger.

The developed model will be validated through simulations at different operational conditions and by comparing the results with the analogous monitored data.

The influences of ambient and working conditions that affect latent heat transfer and frost formation will be investigated through a parametric analysis. Quantitative consideration will be derive from the simulations of a real heat exchanger configuration.

Acknowledgements

I can honestly admit that I never had a burning desire to undertake this task. Thanks to all the people of the Solar thermal heating and cooling team for having created a tremendous working environment that stimulates my desire of knowledge and makes me fond of researching. There I found capable colleagues and good friends. In particular, I would like to thank my research associate, Davide Romeli, for his valuable help and his kindness.

I appreciate the guidance and support from my supervisor at European Research Academy (EURAC) of Bolzano, Dr. Roberto Fedrizzi and Dr. Matteo D'Antoni. Thanks for being patient and for answering my many questions and concerns. You provided the right amount of independence and supervision during this year.

I would like to thank my advisor at the University of Padua, Dr. Michele De Carli, for his advice.

Special thanks to my family for their support and help while I worked on this project. This has not been an easy year but you were always by my side to encourage me. Thanks for your help.

Thanks to all my near and far friends for finding the time to chat. I really appreciate the help of Jehan, Danielle and Carrie during the final draft of this work. Stefano, Claudia, Marco and Martin: thank you for listening to me when I needed most. Most important importantly, thanks Martina for being yourself. You have added meaning and love to my life.

Finally, the financial support from EURAC is gratefully acknowledged.

Table of Contents

List of figures

List of tables

Nomenclature

Symbols

A	Area, [m^2]
a_{fin}	Fin concentration, [1/m]
a_{sat}	Slope of saturation line, [-]
C	Heat capacity, [W/K]
c_f	Fanning friction coefficient, [-]
c_p	Specific isobaric heat, [J/(kg K)]
c_{sat}	Effective saturation specific heat, [J/(kg K)]
c_r	Heat capacity ratio, [-]
$\mathcal{D}_{AB}$	Binary mass diffusivity, [m^2/s]
d	Diameter, [m]
d_h	Hydraulic diameter, [m]
E	Energy, [J]
e	Surface roughness, [m]
F_{he}	Heat exchanger temperature correction factor, [-]
f	Friction factor, [-]
f_P	Petukhov correction factor, [-]
$\dot{g}$	Specific mass flow rate, [kg/(m^2 s)]
Gz	Graetz number, [-]
$h_{eq,fin}$	Equivalent fin height, [m]
h	Convective heat transfer coefficient, [W/(m^2 K)]
h_m	Convective mass transfer coefficient, [m/s]
h'_m	Convective mass transfer coefficient, [kg/(m^2 s)]
i	Enthalpy, [J/(kg)]
i_{LG}	Latent heat of condensation/evaporation, [J/(kg)]
i_{LS}	Latent heat of fusion/melting, [J/(kg)]
i_{SG}	Latent heat of frosting/sublimation, [J/(kg)]
j	Heat transfer Colburn j-factor, $[-]$
j_m	Mass transfer Colburn j-factor, [-]
k	Thermal conductivity, [W/(m K)]
K	Overall heat and mass transfer coefficient, [kg/(m^2 s)]
l	Length, [m]
Le	Lewis number, [-]
$\dot{M}$	Effective ass capacity, [kg/s]
m	Mass, [kg]

m_r	Mass capacity ratio, [-]
$\dot{m}$	Mass flow rate, [kg/s]
MW	Molar weight, [kg/mol]
$\dot{n}$	Molar flux, [mol/(m^2 s)]
Nu	Nusselt number, [-]
p	Pressure, [Pa]
P_l	Longitudinal tube spacing, [m]
P_t	Transversal tube spacing, [m]
Pr	Prandtl number, [-]
$\dot{q}$	Heat transfer flux, [W/m^2]
$\dot{Q}$	Heat transfer rate, [W]
$\dot{Q}_S$	Sensible heat transfer rate, [W]
$\dot{Q}_L$	Latent heat transfer rate, [W]
R	Specific thermal resistance, [(m^2 K)/W]
RA	Overall thermal resistance, [K/W]
R_g	Universal gas constant, [kJ/kmol]
R_{junc}	Junction thermal resistance, [(m^2 K)/W]
Re	Reynolds number, [-]
R_f	Fouling factor, [(m^2 K)/W]
R_m	Effective mass transfer resistance, [(m^2 s)/kg]
$r_{eq,fin}$	Equivalent fin radius, [m]
s_{fin}	Fin spacing, [-]
Sc	Schmidt number, [-]
Sh	Sherwood number, [-]
St	Stanton number for heat transfer, [-]
St_m	Stanton number for mass transfer, [-]
t	Thickness, [m]
T	Temperature, [K] or [°C]
U	Specific overall heat transfer coefficient, [W/(m^2 K)]
UA	Overall heat transfer coefficient, [W/K]
$\dot{V}$	Volumetric flow rate, [m^3/s]
v	Fluid velocity, [m/s]
V	Volume, [m^3]
w	Width, [m]
$\dot{W}_{el}$	Electrical power, [W]
x	Absolute humidity, [kg_v/kg_a]
y_{fan}	Relative fan rotational speed, [-]

z	Axial coordinate, [m]
ΔT_{lm}	Logarithmic mean temperature difference, [K]

Abbreviations

ADP	Apparatus dew point
BF	Bypass factor
$LMED$	Logarithmic Mean Enthalpy Difference
$LMTD$	Logarithmic Mean Temperature Difference
NTU	Heat transfer Number of Transport Unit
$NTU_{h\&m}$	Heat and mass transfer Number of Transport Unit
TOL	Heat transfer tolerance

Greek letters

α	Thermal diffusivity, [m^2/s]
β	Heat exchanger effectiveness parameter, [-]
γ	Glycol mass concentration, [kg_{gly}/kg_w]
ε	Overall heat exchange effectiveness, [-]
ε_a	Airside heat exchange effectiveness, [-]
$\varepsilon_{\dot{Q}}$	Heat transfer rate error, [W]
η_{def}	Defrosting efficiency, [-]
η_{fin}	Fin efficiency, [-]
η_s	Extended surface efficiency, [-]
μ	Dynamic viscosity, [kg/(m s)]
ν	Kinematic viscosity, [m^2/s]
ξ	Fin efficiency parameter, [1/m]
ρ	Density, [kg/m^3]
σ	Heat exchanger compactness, [-]
ς	Molar concentration, [mol/m^3]
τ	Time, [s]
φ	Relative humidity, [-]
ϕ_{def}	Dimensionless defrosting parameter, [-]
ω	Rotational fan speed, [rpm]

Subscripts

1	Row-inlet
2	Row-outlet
a	Air

av	Average
b	Bulk
bp	Water boiling point
c	Convection
$cond$	Condensate, condensation
cs	Cross section
CV	Control volume
d	Ducts
da	Dry air
def	Defrosting
dp	Dew-point
dry	Dry surface
eff	Effective
$fins$	Finned
ff	Free flow
fp	(Air) frost point, (Water) freezing point
fr	Frontal section
ft	Frosted tube
gly	Glycol
h	Hydraulic
$h\&m$	Heat and mass transfer
k	Conduction
i	Inside, internal
in	Inlet
int	Interface
l	Lower limit
L	Latent heat transfer
lam	Laminar flow
m	Mass transfer
max	Maximal
min	Minimal
o	Outside, external
out	Outlet
$prime$	Tube prime surface
ref	Reference
s	Surface

S	Sensible heat transfer
sat	Saturation
set	Set point
sub	Sublimation
tp	Triple point
$turb$	Turbulent flow
v	Water vapour
u	Upper limit
w	Water
wb	Wet bulb
wet	Wet surface
wt	Wet tube
∞	Free stream

Upscripts

$*$	Dimensionless quantity
$.$	Rate per time unit
$\bar{}$	Average quantity
j	Iteration order

1 Introduction

The thesis aims to develop a numerical model of an air-to-water heat exchanger supplied with variable speed fan system under condensing and frosting conditions. The development of the model is characterized by the evaluation of the boundary conditions that affect the heat transfer mechanism, where both sensible and latent heat transfer are involved. Particular attention has been given to model the latent heat transfer and to understand the influences of ambient and working boundary conditions on this phenomenon.

Under given circumstances, if the moisture content of the air stream is sufficiently high, water vapour can condensate on the external side of the heat exchanger. Condensation is initiated and sustained when the surface temperature is maintained below the dew-point temperature of the surrounding air. This results in an improvement of the heat transfer capacity due the combination of latent and sensible heat transfer. When the temperature of the external surface is below both frost- and the dew-point temperature, moisture will first condensate on the coil and then freeze. After freezing, frost starts to accumulate and grow. The presence of frost can cause a drop in the supplied air flow rate and an increase of the thermal resistance. A decrease in the heat transfer capacity results as a consequence. Eventually the reduction of the heat transfer capacity can be so high that a frost must be removed. For this reasons, in order to maintain satisfactory performances of heat exchanger that accumulate frost, periodic defrosting is required frost accumulation increases the specific energy consumption, but also defrosting itself consumes energy: the heat exchanger cannot work properly during defrosting time and the additional (loss) heat supplied for the process must be account.

The focus of this work is pointed on air-source heat pump system in heating seasons. Under condensing condition, the improvement of the heat transfer capacity of the heat exchanger causes an enhancement in the heat pump performance. On the other hand, frost formation and the eventual defrosting process continues to be a source of degradation in the performance of heat pump. Better understanding of the combined heat and mass transfer under condensing and frosting conditions can improve significantly the efficiency in the use and the control of air-source heat pump.

To accomplish these objectives, internal and external heat transfer have been investigated. Initially a survey of the available literature on condensation and on modeling of frosted heat exchanger had been conducted. The most important aspect of the literature review was to find a simple frost growing model that can be coupled with a simultaneous heat and mass transfer model.

The modeling work started with the study of a typical fin-and-tube heat exchanger configuration. A geometry simplification process has been done, to define an elementary control volume, on which the equations of the physical problem are applied. The heat and mass transfer problems have been tackled by developing a FORTRAN® based code that in second step has become the basis of a TRNSYS© type. The type is capable to calculate sensible and latent heat rate, outlet water temperature, as well as fan power consumption of a sized heat exchanger for variable weather and load conditions, under different ambient and load conditions.

The so derived numerical code has been validated through monitored data of a real system installation. Thermal and electrical power calculated by the code have been compared with analogous monitored quantities.

A parametric analysis has been conducted through a series of simulations under different conditions. The end of this simulations was to identified the boundary conditions that affect latent heat transfer and frost formation.

Finally, some quantitative considerations on the influences of the ambient and working conditions on the heat and mass transfer capacity have been derived.

2 Heat and mass transfer phenomena

2.1 Heat and mass convection

In practical applications of air-to-water heat exchanger the main heat transfer mechanism is convection. Internal and external convective phenomena occur respectively between the water flow and the tubes surface and between the air stream and the external surface of the heat exchanger.

The analysis of convection heat and mass transfer problems consists essentially in the determination of the key boundary layer parameters: friction coefficient c_f and heat and mass transfer convection coefficients h and h_m, respectively. The knowledge of local and average convections coefficients are of great importance in the determination of the local flux and of the total transfer rate in any convection problem.

As mentioned, the determination of the convection coefficients is not of simple analytical solution. In addition to depending on numerous fluid properties as density, viscosity, thermal conductivity and specific heat, the coefficients depend on the geometry of the surface and flow conditions. This multiplicity of independent variables is attributable to the dependence of convection transfer on the boundary layers that develop on the surface.

A general relationship between thermal conditions in the thermal boundary layer and the local convection heat transfer coefficient h may be obtained by applying Fourier's law to the fluid at the surface, where there is no fluid motion, and energy transfer occurs only by conduction. Combining this law with Newton's law of cooling [1], it may be obtained:

$$h = \frac{\dot{q}}{(T_s - T_\infty)} = -\frac{k_{fluid}}{(T_s - T_\infty)} \cdot \left.\frac{\partial T}{\partial z}\right|_{z=0} \tag{2.1}$$

where $\dot{q}$ is the heat flux at the surface, k_{fluid} is the thermal conductivity of the fluid, T_s and T_∞ are the surface and free stream temperature, respectively.

Similarly to thermal boundary layer, when a binary mixture of species A and B flows over a surface, a concentration boundary layer is developed. The molar flux associated with species transfer is determined by an expression that is analogous to Fourier's law, which is termed Fick's law. At any point in the concentration boundary layer, species transfer is due to both bulk fluid motion (advection) and diffusion. An analogous relationship to Newton's law, can be written for mass transfer. It relates the molar flux to the concentration difference across boundary layer. Since mass density ρ_A and molar concentration ς_A of species A are related by the following relation:

$$\rho_A = \varsigma_A \cdot MW_A \tag{2.2}$$

where MW_A is molecular weight of the species A, species transfer may also be expressed as mass flux $\dot{g}_A$. In analogy with the thermal convection coefficient h, a convective mass transfer coefficient h_m, can be expressed as follows:

$$h_m = \frac{\dot{g}_A}{(\rho_{A,s} - \rho_{A,\infty})} = -\frac{\mathcal{D}_{AB}}{(\rho_{A,s} - \rho_{A,\infty})} \cdot \left.\frac{\partial \rho_A}{\partial z}\right|_{z=0} \quad \left[\frac{\mathrm{m}}{\mathrm{s}}\right] \tag{2.3}$$

where $\mathcal{D}_{AB}$ is the binary diffusion coefficient of the binary mixture of species A and B that flows over the surface, and , $\rho_{A,s}$ and $\rho_{A,\infty}$ are the density values of species A at the surface and of the free stream, respectively.

Through the local convection coefficients it may be possible to determine the surface local heat and species fluxes. By averaging local convection coefficients over the entire area A_s, the total heat and mass transfer rates, $\dot{Q}$ and $\dot{m}_A$ may be expressed as:

$$\dot{Q} = \bar{h}\, A_s\, (T_s - T_\infty) \tag{2.4}$$

and

$$\dot{m}_A = \bar{h}_m\, A_s\, (\rho_{A,s} - \rho_{A,\infty}) \tag{2.5}$$

According to its definition (see equation 2.3), the water vapour to air mass convective transfer coefficient h_m is defined as:

$$h_m = -\frac{\mathcal{D}_{v,a}}{(\rho_{v,s} - \rho_{v,\infty})} \cdot \left.\frac{\partial \rho_v}{\partial z}\right|_{z=0} \tag{2.6}$$

where $\rho_{v,s}$ is vapour density in the closest air portion to the surface interface and $\rho_{v,\infty}$ is the vapour density in the air free stream.

If condensation occurs on the surface, the water vapour density at its proximity assumes the value of saturated air at the interface temperature T_{int}. Therefore, equation 2.6 can be rewritten as:

$$h_m = -\frac{\mathcal{D}_{v,a}}{(\rho_{sat,v}(T_{int}) - \rho_{v,\infty})} \cdot \left.\frac{\partial \rho_v}{\partial z}\right|_{z=0} \tag{2.7}$$

Furthermore, the water vapour density ρ_v present in the moist air stream can be expressed in terms of absolute humidity x_a and air density ρ_a:

$$h_m = -\frac{\mathcal{D}_{v,a}}{\left(x_{sat,a}(T_{int})\rho_a(T_{int}) - x_{a,\infty}\rho_a(T_{a,\infty})\right)} \cdot \left.\frac{\partial (\rho_a x_a)}{\partial z}\right|_{z=0} \tag{2.8}$$

Typically the air density variation for the encountered temperature range can be neglected. Thus, the convection mass transfer coefficient h_m can be express as:

$$h'_m = -\frac{\mathcal{D}_{v,a}}{(x_{sat,a}(T_{int}) - x_{a,\infty})\rho_a} \cdot \left(\rho_a \left.\frac{\partial x_a}{\partial z}\right|_{z=0} + x_a \left.\frac{\partial \rho_a}{\partial z}\right|_{z=0}\right) \qquad \left[\frac{\text{kg}}{\text{s m}^2}\right] \tag{2.9}$$

where the last terms $\left.\frac{\partial \rho_a}{\partial z}\right|_{z=0}$ between brackets is null.

This new form for the convection mass transfer coefficient h'_m presents the advantage to be readily applicable to absolute humidity difference x_a. Moreover, the majority of the literature about water vapour convection in air stream refers to this expression.

2.1.1 Heat and mass transfer analogies

Since the velocity distribution determines the advective component of thermal energy or mass transfer within the boundary layers, the nature of the flow has a profound effect on convective heat and mass transfer rates. Hence, it is essential to determine the flow conditions. In specific it's essential to determine whether the boundary layer is laminar or turbulent.

The onset of turbulence depends on whether the triggering mechanisms are amplified or attenuated in the direction of the fluid, which depends on the dimensionless Reynolds number. The physical significance of the Reynolds number Re is to represent the ratio of inertia to viscous forces in the stream. If the Reynolds number Re is small, inertia forces are insignificant relative to viscous force, the disturbances are dissipated and the flow

remains laminar. However, for a large Re the inertia forces are sufficient to transmit the triggering mechanisms, and a transition to turbulence occurs [1].

Similarly to the velocity boundary layer, just as it induces large velocity gradients at the surface, turbulent mixing promotes large temperature and species concentration gradient adjacent to the surface as well as a corresponding increase in the heat and mass transfer coefficient across the transition zone.

It is useful to note that a strong similarity exist between the two convection coefficients definitions, h and h_m, since the physical phenomena of heat and mass transfer have the same origin.

Fluid motion in which velocities, temperatures, and concentrations gradients are coexisting must comply with several fundamental laws of nature. In particular, at each point of the fluid, conservation of mass, energy and chemical species, as well as Newton's second law of motion, must be satisfied. If the pressure gradient and the viscous dissipation term are negligible, the equations that described the three convection mechanisms are of the same form: each equation is characterized by an advection and a diffusion term. This situation describes low speed, forced convection flows of incompressible fluids (or ideal gas with negligible pressure variation) with no phase change, which can be found in air-to-water heat exchanger.

According to this, other two very important dimensionless similarity parameters must be introduced: Nusselt number Nu, and Sherwood number Sh.

Nusselt number Nu is a depending parameter that represents the dimensionless temperature gradient at the surface, and provides a measure of the local convection heat transfer occurring at the surface.

$$Nu = \frac{h\,l}{k_{fluid}} = \left.\frac{\partial T^*}{\partial z^*}\right|_{z^*=0} \tag{2.10}$$

For a prescribed geometry, Nu can be expressed as universal function of the dimensionless length l^*, Re and Pr.

$$Nu = f(Re, Pr, l^*) \tag{2.11}$$

If these functions were known, it could be possible to found the local heat convection coefficients h, which could be used to calculate the actual local heat flux $\dot{q}$.

Since the average convective heat transfer coefficient $\bar{h}$ is obtained by integrating over the surface of the body, the corresponding average Nusselt number $\overline{Nu}$ must be independent of the dimensionless spatial variable l^*.

$$\overline{Nu} = \frac{\bar{h}\,l}{k_{fluid}} = f(Re, Pr) \tag{2.12}$$

This equation states that many convection heat transfer results, whether obtained theoretically, or experimentally, can be represented in terms of three dimensionless groups, instead of the original parameters. If the functional dependence has been obtained for a particularly geometry, it can be universally applicable (different fluids, velocities and length scales).

Similarly, a dependent dimensionless parameter is defined for mass transfer in a gas glow over an evaporating liquid or a sublimating solid. The Sherwood number Sh is equivalent to the dimensionless concentration gradient at the surface, and it provides a measure of the convection mass transfer occurring at the surface.

As for the Nusselt number Nu, the Sherwood number Sh for a prescribed geometry must be a universal function of l^*, Re and Sc.

$$Sh = \frac{h_m\, l}{\mathcal{D}_{AB}} = \frac{\partial \varsigma_A^*}{\partial z^*}\bigg|_{z^*=0} = f(Re, Sc, l^*) \tag{2.13}$$

Consequently, it is also possible to work with an average Sherwood number $\overline{Sh}$ that depends on only Re and Sc.

$$\overline{Sh} = \frac{\overline{h_m}\, l}{\mathcal{D}_{AB}} = f(Re, Sc) \tag{2.14}$$

Nu and Sh are generally proportional to Pr^n and Sc^n, respectively, where n is a positive exponent less than unity. By knowing this dependence we can use equations 2.11 and 2.13 to obtain:

$$Nu = f(Re, l^*) Pr^n \tag{2.15}$$

and

$$Sh = f(Re, l^*) Sc^n \tag{2.16}$$

Since the physical phenomena of convective heat and mass transfer have the same origin, it is useful to note that this mechanisms are analogous processes, or rather, they are governed by dimensionless equations of the same form. Each of the differential equations is composed by a diffusion and an advection term of the same form. The main implication of this analogy is that the dimensionless relations that govern the two processes must also be the same. Hence the boundary layer temperature and the concentration profiles must also be of the same functional form if the boundary conditions are analogous. This analogy can be observed also in the strong similarity that exists between the expressions of the Prandtl number Pr and Schmidt number Sc.

$$Pr = \frac{\nu_{fluid}}{\alpha_{fluid}} \qquad Sc = \frac{\nu_{fluid}}{\mathcal{D}_{AB}} \tag{2.17}$$

where α_{fluid} is thermal diffusivity of the fluid.

Prandtl number Pr provides a measure of the relative effectiveness of momentum and energy transfer by diffusion in the velocity and thermal boundary layer, respectively.

$$Pr = \frac{\nu_{fluid}}{\alpha_{fluid}} \tag{2.18}$$

where α_{fluid} is thermal diffusivity of the fluid. The Schmidt number Sc provides a measure of the relative effectiveness of momentum and mass transport by diffusion in the velocity and concentration boundary layer.

These parameters allow applying results obtained for a surface experiencing one set of convective conditions to geometrically similar surface. As long as the similarity parameters and dimensionless boundary conditions are the same for two sets of condition, the solutions of the differential boundary layer equations will also be the same.

Introducing another relevant dimensionless parameter for any situation that involves simultaneous convective heat and mass transfer can lead to relate directly the two convection coefficients h and h_m. In fact, an equivalent function $f(Re, l^*)$ could be used to determine one of the two convection coefficients when knowledge of the other one is known:

$$\frac{Nu}{Sh} = \frac{Pr^n}{Sc^n} = \frac{h}{h_m} = \frac{k_{fluid}}{\mathcal{D}_{AB}\, Le^n} = \rho_{fluid}\, c_{p,fluid}\, Le^{1-n} \tag{2.19}$$

Where the Lewis Number Le expresses the ratio of the thermal and mass diffusivities:

$$Le = \frac{\alpha_{fluid}}{\mathcal{D}_{AB}} = \frac{Sc}{Pr} \tag{2.20}$$

The same relationships obtained for the local convective coefficients may be applied to the average coefficients in turbulent, as well as laminar flow.

A second boundary layer analogy is obtained by noting that when there is no pressure gradient dp/dl^*, the velocity, the thermal and the concentration conservation equations for the boundary layer are of the precise same form. From the developed equations it may be obtain:

$$c_f \frac{Re}{2} = Nu = Sh \tag{2.21}$$

where c_f is the local Fanning friction factor in the velocity boundary layer, defined as [1]:

$$c_f = \frac{2\,\mu_{fluid}}{\rho\, V^2} \cdot \frac{\partial v}{\partial z}\bigg|_{z=0} \tag{2.22}$$

where μ_{fluid} is the dynamic viscosity of the fluid.

The previous analogy may also be expressed in the following form, known as Reynolds analogy [1] equation:

$$\frac{c_f}{2} = St\ = St_m \tag{2.23}$$

by replacing Nu and Sh by the thermal Stanton number St and the mass transfer Stanton number St_m, respectively:

$$St = \frac{h}{\rho\, v\, c_p} = \frac{Nu}{Re\, Pr} \tag{2.24}$$

and

$$St_m = \frac{h_m}{v} = \frac{Sh}{Re\, Sc} \tag{2.25}$$

The Reynolds analogy may be used to obtain thermal and concentration boundary layer parameters by knowing the velocity parameter, and vice versa. The accuracy of the analogy, in addition to relying on the validity of the boundary layer approximations, depends on having Pr and Sc values near the unity and dp/dx^* approaching zero.

It has been shown [2][3] that, if certain corrections factors are added to equation 2.23, the analogy may be applied over a wider range of Pr and Sc. In particular, the Chilton-Colburn (or modified Reynolds) analogies have the form:

$$0{,}6 < \mathrm{Pr} < 60 \qquad j = \frac{c_f}{2} = St\, Pr^{2/3} \tag{2.26}$$

and

$$0{,}6 < Sc < 60 \qquad j_m = \frac{c_f}{2} = St_m\, Sc^{2/3} \tag{2.27}$$

where j and j_m are the Colburn j-factors for heat and mass transfer, respectively.

These equations are appropriate in laminar flow only when dp/dx^* is near zero. In turbulent flow these equations remain approximately valid, because the flow conditions

are less sensitive to the effect of pressure gradient [1]. Cleary, if the analogy can be applied at every point on a surface, it also may be applied to the surface average coefficients.

Referring to the presented heat and mass transfer analogies, the convection mass transfer coefficient h'_m for a dehumidifying moist air stream over a cold surface can be more easily expressed as:

$$h'_{m,o} = h_{m,o}\,\rho_a = \frac{h_o}{c_{p,a}}\rho_v = \frac{h_o}{c_{p,a}}(x_a \rho_a) \tag{2.28}$$

To determinate the external h_o and internal h_i convection coefficients of an air-to-water heat exchanger, two approaches could be taken: one analytical and the other empirical.

The first approach involves solving the boundary layer equations for a given geometry. It is only applicable for simple flow situations.

When the analysis of flow conditions becomes more complex, the empirical approach can lead to easier solution. This practical approach involves the calculation of coefficients from empirical relations obtained by performing heat or mass transfer measurements under controlled laboratory conditions and correlating the data in terms of appropriate dimensionless parameters. Because of the complex flow through a heat exchanger, the majority of convective coefficients are based on empirical correlations.

2.2 Heat performance of an air-to-water heat exchanger

From a physical point of view, a heat exchanger is considered as an adiabatic steady-flow system in which the temperature at any point does not change and the rate of heat transfer does not vary with time. Hence, the heat transfer rate between the exchanger and its surrounding is negligible, as well as changes in potential kinetic energy of the fluids.

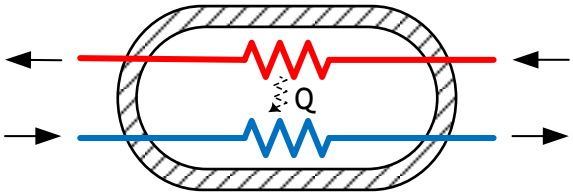

Figure 2.1 Adiabatic heat exchanger system

By applying the overall energy balance, two relationships for the total heat transfer rate $d\dot{Q}$ between hot and cold fluids may be obtained:

$$d\dot{Q}_{hot} = (\dot{m}\ di)_{hot} \tag{2.29}$$

$$d\dot{Q}_{cold} = (\dot{m}\ di)_{cold} \tag{2.30}$$

where i is the specific fluid enthalpy and $\dot{m}$ is the mass flow rate of the fluid.

If the fluids are incompressible or are subject to the ideal gas law, equation 2.29 and can be rewritten as:

$$d\dot{Q} = (\dot{m}\ di)_{cold} = \dot{m}_{cold} c_{p,cold} dT_{cold} = \dot{m}_{hot} c_{p,hot} dT_{hot} = d\dot{Q} = (\dot{m}\ di)_{hot} \tag{2.31}$$

The geometrical characteristics of heat exchangers may influence significantly the performance. It is essential to obtain expressions that relate the total heat transfer rate $\dot{Q}$ to quantities such as the inlet and outlet fluids temperatures, the overall heat transfer coefficient and the total surface area for heat transfer. Such expressions may be obtained by applying an extension of Newton's law. The heat rate transferred between two fluids at different temperature, respectively T_{hot} and T_{cold}, through a base element of area dA may be expressed as:

$$d\dot{Q} = U(T_{hot} - T_{cold})\, dA \tag{2.32}$$

where U identifies the overall heat transfer coefficient referred to the exchange area dA.

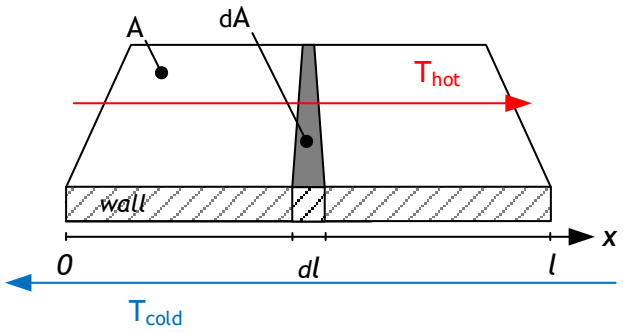

Figure 2.2 Hot and cold fluid streams separated by a wall

The hypothesis of adiabatic system implies that the value of heat transfer rate $d\dot{Q}$ should be equal to the heat given up by the hot fluid or gained by the cold fluid flowing from position A to $A + dA$.

To determine the total heat transfer rate $\dot{Q}$, which is transferred through a heat exchanger should be integrated through the heat transfer area A_{tot}. This integration is usually done with two different approaches, known as Log Mean Temperature Difference (LMTD) method and Effectiveness-NTU (ε-NTU) method.

In general the temperature difference ΔT between hot and cold fluids is not constant. It varies with the position along the heat exchanger. For an ideal counterflow heat transfer between two fluids, the temperature distribution assumes a typical logarithmic trend. Hence, the total heat transfer rate $\dot{Q}_{tot}$ of heat exchanger can be evaluated in the form:

$$\dot{Q}_{tot} = \overline{U}\, A_{tot}\, F_{he}\, \Delta T_{lm} \tag{2.33}$$

where ΔT_{lm} is the logarithmic mean temperature, F_{he} is the correction factor to account for the difference between the real temperature distribution and the temperature distribution of an ideal counterflow heat transfer, and $\overline{U}$ is the average overall heat transfer coefficient for the entire heat exchanger.

The LMTD is useful in all the cases when the inlet temperatures are known and the outlet temperatures are specified or readily determined from the energy balance equations 2.29 and 2.30.

When the heat transfer surface area and the flow passage dimensions are given, as well as the overall heat transfer coefficient, the adoption of LMTD method to determine the heat transfer rate and the outlet fluids temperatures is to avoid. In fact, its application would require iterative approximations for the outlet temperatures.

To avoid these laborious iterations, it is more appropriate to use the ε-NTU method, which gives a straightforward solution. (For a detailed comparison of ε-NTU and LMTD approaches see [4])

The ε-NTU method [4], is a non-dimensional method that allows to group the numerous variables related to the heat performance of a heat exchanger in a smaller number of readily visualized physical significant parameters. These non-dimensional parameters are also useful in allowing a graphical representation of the heat transfer performance (see appendix B for a complete description of the ε-NTU method).

The effectiveness ε is usually expressed as function of the overall number of heat transfer units NTU and the thermal capacity-rate ratio c_r through a specified flow arrangements function in the form:

$$\varepsilon = f(NTU,\ c_r, flow\ arrangement) \tag{2.34}$$

Generally this function has an asymptotic trend for a given capacity-rate ratio: the effectiveness ε approaches asymptomatically the limit imposed by the flow arrangement and thermodynamical considerations, when NTU increase from smaller to larger values.

In the developed model the formulation relating the effectiveness ε to NTU and the thermal capacity-rate ratio c_r for cross-flow heat exchanger with unmixed fluids are taken from ESDU publication [5] and from Laskowski work [6]. These relationships are summarized in the following table, where β is a dimensionless parameter defined as [5]:

$$\beta = 1 - e^{-NTU/row} \qquad C_{min} = C_a \tag{2.35}$$

$$\beta = 1 - e^{-NTU \cdot c_r /row} \qquad C_{min} = C_w \tag{2.36}$$

except for a row number greater than 4 where it equals [6]

$$\beta = 1 - e^{-NTU} \qquad C_{min} = C_w \tag{2.37}$$

Table 2.1 Effectiveness-NTU relationship for unmixed cross-flow

Row order	C_{min}	Relationship
1	C_a	$\varepsilon = \frac{1}{c_r}\left(1 - e^{-\beta \cdot c_r}\right)$
	C_w	$\varepsilon = 1 - e^{-\beta / c_r}$
2	C_a	$\varepsilon = \frac{1}{c_r}\left(1 - e^{-2\,\beta \cdot c_r} \cdot (1 + c_r \cdot \beta^2)\right)$
	C_w	$\varepsilon = 1 - e^{-2\,\beta / c_r} \cdot \left(1 + \frac{\beta^2}{c_r}\right)$
3	C_a	$\varepsilon = \frac{1}{c_r}\left(1 - e^{-3\,\beta \cdot c_r} \cdot \left(1 + c_r \cdot \beta^2(3 - \beta) + \frac{3\,\beta^4 {c_r}^2}{2}\right)\right)$
	C_w	$\varepsilon = 1 - e^{-3\,\beta / c_r} \cdot \left(1 + \frac{\beta^2(3 - \beta)}{c_r} + \frac{3\,\beta^4}{2\,{c_r}^2}\right)$

4	C_a	$\varepsilon = \frac{1}{c_r}\left(1 - e^{-4\,\beta \cdot c_r} \cdot \left(1 + c_r \cdot \beta^2(6 - 4\,\beta + B\beta^2) + \frac{8\,\beta^4 {c_r}^2(2-\beta)}{2} + \frac{8\,{c_r}^3\beta^6}{3}\right)\right)$
	C_w	$\varepsilon = 1 - e^{-4\,\beta/C} \cdot \left(1 + \frac{\beta^2(6 - 4\,\beta + \beta^2)}{c_r} + \frac{8\,\beta^4(2-\beta)}{2\,{c_r}^2} + \frac{8\,\beta^6}{3\,{c_r}^3}\right)$
> 4	C_a	$\varepsilon = \left(\frac{NTU}{1 + 1.238\,NTU} - \beta\right) \cdot c_r + \beta$
	C_w	$\varepsilon = \left(\frac{NTU}{1 + 1.238\,NTU} - \beta\right) \cdot c_r + \beta$

In contrast to the LMTD method, the ε-NTU method provides an explicit expression for the determination of the actual heat transfer rate $\dot{Q}$ through the exchanger if the initial fluids temperatures and C_{min} are known, and it is possible to determine the effectiveness ε of the exchanger:

$$\dot{Q} = \varepsilon\,\dot{Q}_{max} = \varepsilon\,C_{min}\left(T_{hot,in} - T_{cold,in}\right) \tag{2.38}$$

The LMTD and ε-NTU presented some applicability limits, due to the assumptions on which the methods are based. The two methods are steady-state concepts and may not be applied to transient analyses. When the fluids properties are strongly dependent from the temperature, the methods will be no longer accurate: in fact, both approaches assume constant values for the specific heats. Also the assumption of constant overall heat transfer coefficient over the entire heat exchange surface may not be verified. The greatest limitation of the LMTD and ε-NTU concerns the evaluation of only (moved it) sensible heat transfer. These methods are not applicable in all those cases, where sensible and latent heat transfer occurs.

Common applications of air-to-water finned tubes heat exchangers involve air dehumidification when the surface temperature is under the adjoin air dew point temperature. As consequence, vapour moisture is separated from the atmospheric air and the airside is wetted (by liquid condensed water or frost). Besides transfer of sensible heat, there is a vapour mass transfer and latent heat transfer because of condensation.

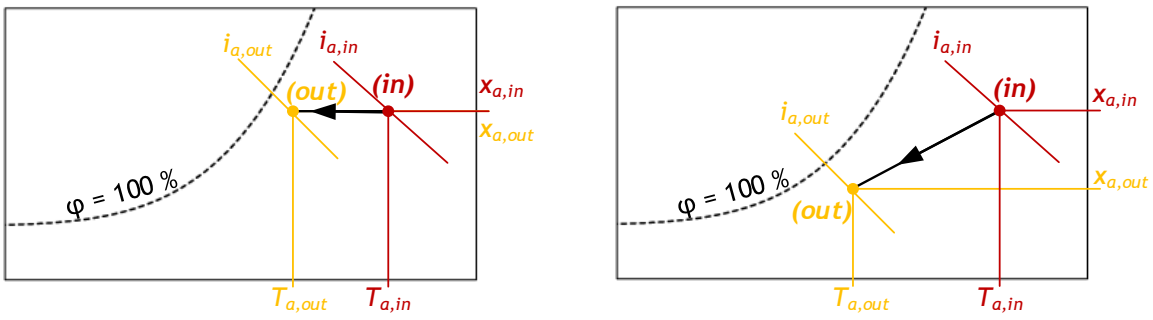

Figure 2.3 Pshychrometric chart for sensible cooling process (left) and for cooling and dehumidifying process (right)

In literature a large number of works about theoretical and computational predictions of vapour condensation and frost formation in the presence of non-condensable gas have been written. The majority of those publications are focused on the heat and mass transfer of air-water vapour mixture. The first theoretical method to predict condensation and mass transfer controlled by mass concentration gradient through a non-condensable gas was developed by Colburn & Hougen [7]. Over the years, this model has been modified and improved by many authors. In particular, the increase of currently available numerical calculation capacity allows to apply theoretical and experimental results on distributed-parameters numerical simulations using computer programs such Computational Fluid Dynamic (CFD) software. Distributed-parameters model are very accurate, mainly because it is possible to predict the condensing transfer rates through the simultaneous solutions of heat and mass transfer balance of interrelated micro-scale elements. Even if the computational resources were strongly increased in the last decades, CFD-simulation techniques still requires a high computational cost, which would be too high for the purpose of this work. Hence, it has been considered to be more suitable to choose a lumped-parameters approach, which usually involves semi-analytical models and experimental correlations to predict the performance of the heat exchanger. In practice, lumped parameter model is particularly convenient to apply because it is not needed to account for the spatial distribution of air temperature and humidity nor for water temperature.

When a lumped parameter method is applied, it is critical to determine the driving force of the heat and mass transfer. The driving force for sensible heat transfer is only the temperature difference between hot and cold-side of the heat exchanger. In case of simultaneous transfer of heat and mass driving force results the difference in moist air enthalpy (accounting humidity and temperature difference) rather than a difference in the air dry-bulb temperature only.

In this condition convectional LMTD and ε-NTU methods cannot be directly applied to predict the heat exchanger performance. To also permit the evaluation of latent heat transfer, the two methods were modified from their original form. The derived methods are usually presented in terms of enthalpy difference. There are two general approaches: the first and more used approach takes directly into account the air enthalpy difference; the second approach is presented through the definition of an Equivalent Dry Temperature EDT. The enthalpy difference is replaced by an equivalent temperature difference, that allows to operate in an equivalent dry process. The equivalent dry bulb temperature can be obtained from adopting a constant process line in the pshychrometrics chart (see Mirth & Ramadhyani [8]). Vardhan & Dhar [9] described the numerical procedure to apply this method. The resulting calculation scheme made the total computational time for a whole coil very long. Wang and Hihara [10] presented a new iterative solution that simplifies the calculation scheme and reduces the calculation time. However, the resulting computational time would be still too high for our purpose. Thus, the attention has been pointed on the first kind of methods.

In literature it is easy to find simultaneous sensible and latent heat transfer method based on the Logarithmic Mean Enthalpy Difference LMED. A fundamental model for cooling coils, largely adopted for many data reductions, was presented by Threlkeld [11] in 1970. His solution is presented in terms of LMED between the inlet and outlet flow streams. Similar to the LMTD method, these methods are better suited for design purpose in all those situations, where the inlet and outlet fluids conditions are known. For given coil geometry and inlet conditions, the solution requires an iterative procedure with respect to the outlet conditions. As for the classical temperature based effectiveness-NTU method, in those

situations results to be more convenient the enthalpy-based effectiveness-NTU (ε-NTU) method.

ε-NTU enthalpy based methods reported in literature are usually available for cooling tower (see [12] as example). The studies applied to heat exchanger, where air and water streams are separated, are rare. The adopted method in this work is based on the study of Braun [13]. His thesis reports a simple method to predict the performance of cooling coils that presents wet and dry sections.

For an infinitesimal portion of the exchanger, neglecting the energy flow associated with condensate draining from the coil [11], the energy balance applied to the air stream takes the form:

$$\begin{aligned} d\dot{Q}_a &= \dot{m}_a\left(di_{a,dry} + di_v\right) \\ &= \dot{m}_a c_{p,a} dT_a \\ &+ \dot{m}_a\left(x_a\left(c_{p,v}T_a + i_L\right) + -(x_a + dx_a)\left(c_{p,v}(T_a + dT_a) + i_L\right)\right) \end{aligned} \tag{2.39}$$

where x_a is the air absolute humidity, $c_{p,v}$ is the water vapour specific heat and i_L is the latent heat due to condensation or frost formation depending on the situation.

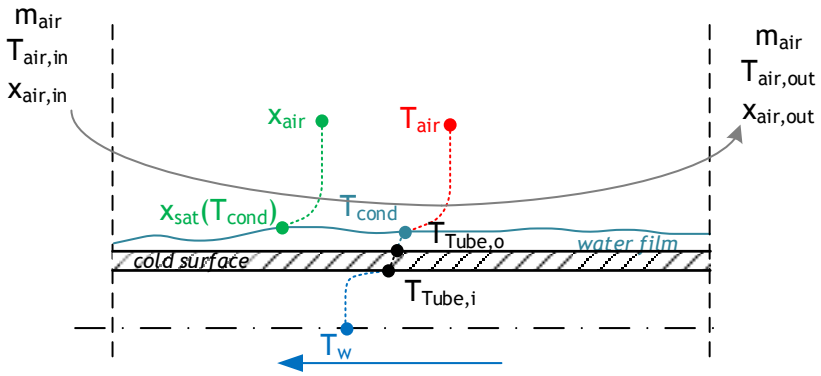

Figure 2.4 Schematic cooling and dehumidifying of moist air on a cold surface

The enthalpy difference caused by the temperature variation on the water vapour fraction of the humid air can be neglected. Hence, equation 2.40 becomes:

$$d\dot{Q}_a = \dot{m}_a\left(di_{a,dry} + di_v\right) \approx \dot{m}_a c_{p,a} dT_a + \dot{m}_a(x_a + dx_a)i_L \tag{2.40}$$

The energy balance applied to the water can be expressed as follow:

$$d\dot{Q}_w = \dot{m}_w di_w = \dot{m}_w c_{p,w} dT_w \tag{2.41}$$

Maintaining the assumption of adiabatic system, the water $d\dot{Q}_w$ and air $d\dot{Q}_a$ heat transfer must be identical:

$$d\dot{Q}_w = \dot{m}_w c_{p,w} dT_w \approx \dot{m}_a di_a = d\dot{Q}_a \tag{2.42}$$

If the saturation enthalpy $i_{sat,a}$ were linear with respect to the temperature, equation 2.43 could be solved analytically for the outlet condition. Experiments show that the saturation enthalpy is not linear with respect to the temperature (see [11] and [14]).

In his simple, yet fundamental model for cooling coils, Threlkeld [11] identifies and describes the process line on the psychrometrics chart for cooling and dehumidifying of moist air by a cold surface. He suggests that over a small range of temperature, such as

about 5°C, the enthalpy of saturated air i_{sat} may be linearized without introducing significant error:

$$di_{sat,a}(T) = a_{sat} + c_{sat}(T)dT \tag{2.43}$$

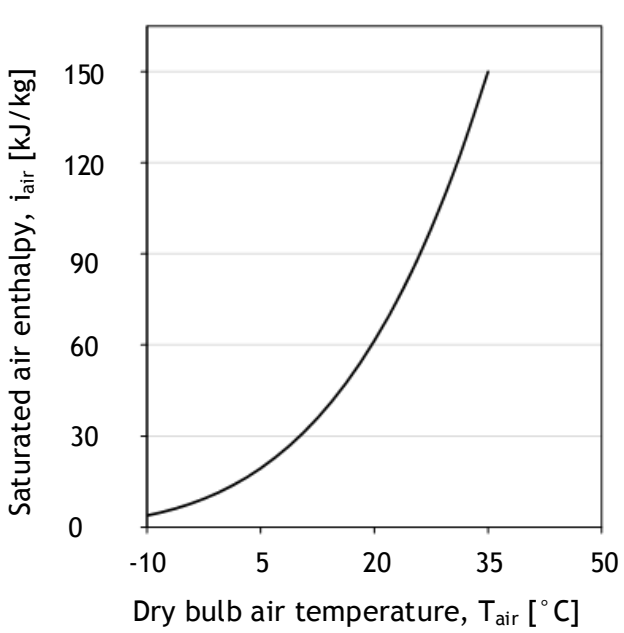

Figure 2.5 Enthalpy of saturated air as a function of tempreature for standard atmospheric pressure

The analytic solution to the heat and mass transfer balances obtained by Threlkeld was developed by assuming a linear relationship for saturation air enthalpy, with respect to the surface and water temperature.

Similarly to the air enthalpy linearization assumed by Threlkeld, Braun et al. [15] introduced an effective saturation specific heat c_{sat}, which expresses the gradient of saturated air enthalpy $i_{sat,a}$ with respect to the temperature evaluated at the water temperature only:

$$c_{sat}(T) = \left.\frac{di_{sat,a}}{dT}\right|_{T_w} \tag{2.44}$$

Hence, assuming:

$$di_{sat,a}(T_w) = c_{sat}(T)dT_w \tag{2.45}$$

equation 7.4 can be rewritten in terms of only air enthalpies:

$$\left(\dot{m}_w \frac{c_{p,w}}{c_{sat}(T)}\right) di_{sat} \approx \dot{m}_a di_a \tag{2.46}$$

Note that this equation is analogous to the differential equation that results for a sensible heat transfer (equation 2.31) with c_{sat}, di_{sat} and di_a replaced by $c_{p,w}, dT_w$ and di_a. In analogy with the ε-NTU temperature based method, the first term of the equation is the effective water mass flow rate, also note as water mass capacity:

$$\dot{M}_w = \dot{m}_w \frac{c_{p,w}}{c_{sat}(T)} \tag{2.47}$$

whereas the air mass capacity $\dot{M}_a$ coincides with the air mass flow rate $\dot{m}_a$. In their work [15] Braun et al. assumed that the heat exchanger effectiveness relationship may be derived in terms of a constant value of c_{sat} by choosing an appropriate average slope between the inlet and the water conditions:

$$c_{sat} = \frac{i_{sat,a}(T_{w,out}) - i_{sat,a}(T_{w,in})}{T_{w,out} - T_{w,in}} \tag{2.48}$$

Usually the heat exchanger effectiveness is defined as the ratio of the actual $\dot{Q}$ to maximum possible $\dot{Q}_{max}$ heat transfer rates. In Braun's method, as a consequence of assuming c_{sat} as average slope between the inlet and the water conditions, rather than an overall effectiveness ε (as for the sensible heat transfer), an airside effectiveness ε_a should be used.

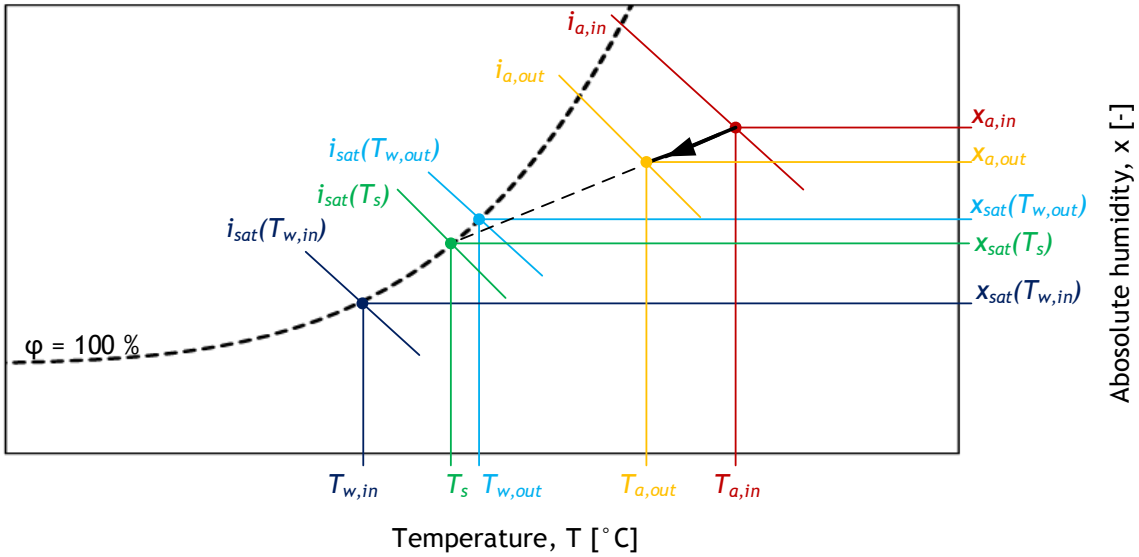

Figure 2.6 Air cooling and dehumidifying process and effective saturated air conditions for water and surface temperatures

The air-side effectiveness ε_a is defined as the ratio of the actual heat transfer rate $\dot{Q}$ to the maximum possible air-side heat transfer rate $\dot{Q}_{a,max}$ that would occur if the outlet air stream are saturated at the temperature of the inlet water (i.e. $i_{a,out} = i_{sat,a}(T_{w,in})$):

$$\varepsilon_a = \frac{\dot{Q}}{\dot{Q}_{a,max}} = \frac{\dot{Q}}{\dot{m}_a(i_{sat,a}(T_{w,in}) - i_{a,in})} \tag{2.49}$$

In analogy, with the definition of the overall NTU defined for the sensible heat transfer, the overall $NTU_{h\&m}$ number for heat and mass transfer (or for sensible and latent heat transfer) is defined as:

$$NTU_{h\&m} = \frac{\bar{K} A_{tot}}{\dot{M}_a} \tag{2.50}$$

where $\bar{K}$ is the average overall mass transfer coefficient over the surface A_{tot}. Braun's model neglected the presence of the condensate layer, because its insulating effect is

usually of minor importance compared to the air convection as suggested by Threlkeld [11].

It's particularly useful to calculate the overall NTU_m as combination of the airside ($NTU_{a,h\&m}$) and the waterside (NTU_w) partial NTU:

$$NTU_{h\&m} = \frac{NTU_a}{1 + \frac{NTU_a}{NTU_w} m_r} \tag{2.51}$$

where m_r is the mass capacities ratio and is always refered to the air (and no more to the minimum heat capacity between the two fluids):

$$m_r = \frac{\dot{M}_a}{\dot{M}_w} = \frac{\dot{m}_a}{\dot{m}_w \left(\frac{c_{p,w}}{c_{sat}}\right)} \tag{2.52}$$

Because the waterside involves only sensible heat transfer, the waterside NTU_w follows its definition for the sensible heat transfer:

$$NTU_w = \frac{\overline{U}_w A_w}{C_w} \tag{2.53}$$

In contrast, the airside $NTU_{a,h\&m}$ will differ for dry and wet portion due the different heat and mass transfer coefficients and fin efficiency (see next paragraphs). For the wetted part $A_{a,wet}$ of the heat transfer area, a different definition of $NTU_{a,h\&m}$ (from the sensible heat transfer case) is needed:

$$NTU_{a,h\&m} = \frac{\overline{K}_a A_{a,wet}}{\dot{M}_a} \tag{2.54}$$

where $\overline{K}_a$ is the airside overall heat and mass transfer coefficient.

For the dry part $A_{a,dry}$ the following expression remains valid:

$$NTU_{a,h} = \frac{\overline{U}_a A_{a,dry}}{\dot{C}_a} \tag{2.55}$$

As for the sensible heat transfer, the wall resistance can be added to the airside or to the waterside. Usually it is added to the waterside in term of thermal resistance because no mass transfer occurs in the wall.

The forms of the equation that relates the heat exchange effectiveness ε, to the overall NTU, and to the heat capacities ratio c_r can be also maintained to express the airside effectiveness ε_a as function of the overall $NTU_{h\&m}$ and m_r:

$$\varepsilon_a = f(NTU_{h\&m}, m_r, flow\ arrangement) \tag{2.56}$$

In the developed model the temperature-based and the enthalpy-based effectiveness-NTU methods are applied respectively, when only sensible heat transfer and when simultaneous sensible and latent heat transfers occur.

In order to combine the two methods under a common form, the temperature-based ε-NTU method can be attributed to a restricted version of the enthalpy-based ε-NTU method where no dehumidification takes place. In fact when only sensible heat transfer is occurring, the two methods are equivalent (see appendix B) if the effective saturation specific heat c_{sat} is substituted by the air specific heat $c_{p,a}$ and the saturated air enthalpy

at the inlet water temperature $i_{sat,a}(T_{w,in})$ is substituted by an effective air enthalpy at the inlet absolute humidity $x_{a,in}$ and at the inlet water temperature $T_{w,in}$:

$$i_a(T_{w,in}) = f(x_{a,in}, T_{w,in}) \tag{2.57}$$

$$c_{sat} = c_{p,a} \tag{2.58}$$

2.2.1 Overall heat and overall mass transfer coefficients

When only sensible heat transfer occurs, the presented approaches ($LMTD$ and $\varepsilon - NTU$ methods) to predict the exchanger performance require to quantify the average overall heat transfer coefficient $\bar{U}$. Its determination is one of the most complex issues to evaluate in a heat exchanger. If no significant entrance effects or changes in physical properties occur, the local heat transfer coefficient U could be assumed to be constant on all the heat transfer area A_{tot}. Under this assumption local U and overall $\bar{U}$ heat transfer coefficient coincides.

The overall heat transfer coefficient is the combination of the various thermal resistances in the path of heat flow between the two streams. The reciprocal of the average overall heat transfer coefficient $\bar{U}$ is the average overall thermal resistance $\bar{R}$, which for a heat exchanger, can be assumed to be composed of a series of thermal resistances [4]:

- hot flow convection thermal resistance $R_{c,hot}$, including the temperature ineffectiveness of extended surface or fin area;
- conduction thermal resistances of the material layer between hot and cold fluids R_k;
- thermal resistance of the wall-fins junction R_{junc};
- cold flow convection thermal resistance, including the temperature ineffectiveness of extended surface or fin area $R_{c,cold}$;
- fouling thermal resistances $R_{f,hot}$ and $R_{f,cold}$ to allow for scaling in service on both hot and cold sides.

An equivalent thermal circuit expressing this idea is presented in the following figure:

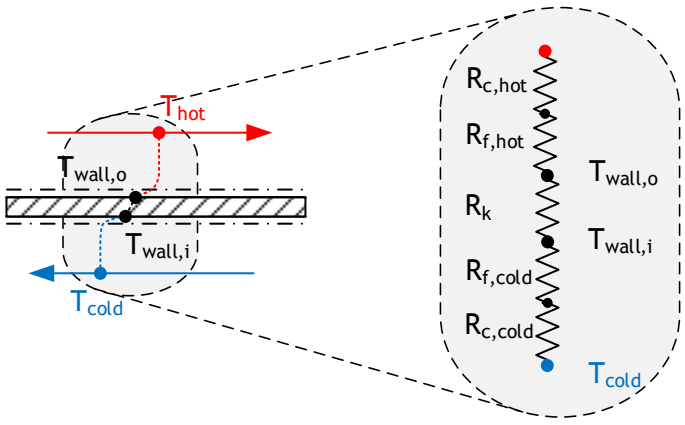

Figure 2.7 Thermal circuit representation for steady state heat transfer between two fluids separated by a solid wall

Accordingly, with the effect of surface fouling and extended surface effects, the overall thermal resistance $\bar{R}$ of the thermal circuit presented in Figure 2.7 can be expressed as

overall heat transfer coefficient based on either cold side or hot side surface of the exchanger:

$$\bar{R}A = \frac{1}{\bar{U}A} = \frac{1}{(\bar{U}A)_{cold}} = \frac{1}{(\bar{U}A)_{hot}} = \\ = \frac{1}{(\eta\, h\, A)_{cold}} + \frac{R_{f,cold}}{(\eta\, A)_{cold}} + R_k + R_{junc} + \frac{R_{f,hot}}{(\eta\, A)_{hot}} + \frac{1}{(\eta\, h\, A)_{hot}} \tag{2.59}$$

The calculation of the product $\bar{U}A$ does not matter on which area it is based as long as it is specified in its definition.

As for the overall heat transfer rate, it is possible to express an overall mass transfer coefficient $\bar{K}_m$ as follows:

$$d\dot{m}_{fluid} = \bar{K}_m dA\left(\rho_{fluid,\infty} - \rho_{fluid,s}\right) \tag{2.60}$$

The overall mass transfer coefficient $\bar{K}_m$ can be evaluated accounting for the mass transfer resistances R_m present between the fluid free stream and the specified surface.

For simultaneous heat and mass transfer, the overall heat and the overall mass transfer coefficient can be coupled obtaining the overall heat and mass transfer coefficient $\bar{K}$ (or overall latent heat transfer coefficient). This coefficient expresses the local average effective mass transfer for a fluid on a surface A between its enthalpy value at free flow and its surface conditions:

$$d\dot{Q} = \bar{K} dA\left(i_{fluid,\infty} - i_{fluid,s}\right) \tag{2.61}$$

In air-to-water heat exchanger, an overall mass transfer $\bar{K}_a$ may be associated at the airside if the moist air stream modifies its contained vapour fraction:

$$\bar{K}_a = \frac{d\dot{Q}_a}{dA\left(i_{a,\infty} - i_{a,s}\right)} \tag{2.62}$$

The airside coefficient $\bar{K}_a$ takes into account not only the convection mass transfer resistance R_m, but also the effective mass resistance associated to the thermal conduction resistances of the airside.

$$\bar{K}_a = \frac{1}{\frac{1}{R_a} + \left(\frac{1}{R_{k,m}}\right)_a} \tag{2.63}$$

The airside convective mass transfer resistance can be expressed as:

$$R_a = \frac{1}{\left(h'_m\, \eta_{fin}\right)_a} \tag{2.64}$$

where the η_{fin} is the extended surface effectiveness for simultaneous heat and mass transfer (see paragraph 2.4.3 and 2.4.4). h'_m is the convective mass transfer coefficient.

If an additional layer (like a liquid water or frost) is present on the area A_a, which the airside coefficient $\bar{K}_a$ refers to, its insulating effect can be taken into account by associating to it the thermal conduction resistance R_k and the effective mass transfer resistance $R_{m,k}$. Threlkeld [11] introduced the use the slope of the saturated air enthalpy at the temperature of the additional layer as conversion factor:

$$R_{m,k} = R_{m,k}\left(\frac{1}{\frac{di_{sat,a}}{dT}\Big|_{T_{layer}}}\right) \tag{2.65}$$

Since the conductive resistance of the condensate is usually of minor importance, Threlkeld [11] suggested that a precise evaluation of the saturated air enthalpy slope at the layer temperature is usually not necessary. This value can be substituted with the slope at the water temperature that coincides with the effective saturation specific heat c_{sat} proposed by Braun [13]. This approximation has been considered valid also for the frost layer. Hence, the effective mass transfer resistance $R_{m,k}$ results:

$$R_{m,k} = R_{m,k}\frac{1}{c_{sat}} \tag{2.66}$$

2.3 Internal heat transfer

For internal heat transfer is intended the heat transfer that occurs from the water bulk condition to the interface between the free air stream and the external coil surface.

The specific internal (or waterside) overall heat transfer resistance R_i takes into account of the convection between water bulk condition and internal tube surface and of the radial conduction in the tube. In addition to these two components, the effects of fouling and of tube-fins junction can be account.

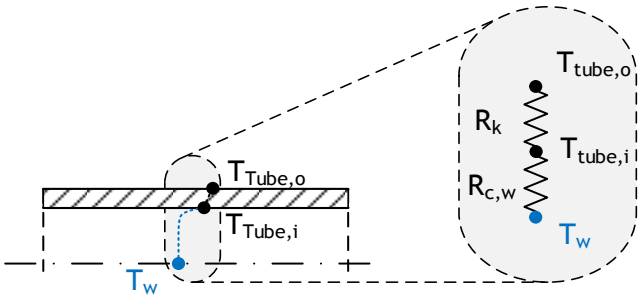

Figure 2.8 Temperature profile of a tube portion and equivalent thermal circuit

When condensation or frost formation occurs, on the external coil surface can be present a layer of liquid water or frost, respectively. This layer acts as an additional insulation present on the external surface of the tubes. Hence, a conductive thermal resistance must be added at the overall internal thermal resistance.

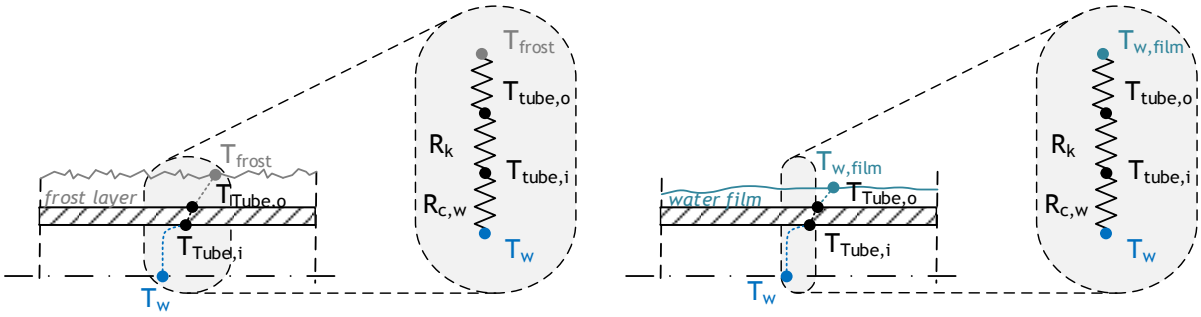

Figure 2.9 Temperature profile of frosted and wetted tube portions and equivalent thermal circuits

Once the internal convective heat transfer coefficient h_i is determined the internal overall overall heat transfer rate coefficient $(UA)_i$ can be determine. For an unfrosted surface it results:

$$(UA)_i = A_i \frac{1}{\frac{1}{h_i} + \frac{\frac{d_i}{2} ln\left(\frac{d_o}{d_i}\right)}{k_{tube}}} \tag{2.67}$$

Whereas, for a surface presenting a frost layer characterized by a thickness t_{frost} and a thermal conductivity k_{frost}, the internal overall heat transfer rate coefficient $(UA)_i$ becomes:

$$(UA)_i = A_i \frac{1}{\frac{1}{h_i} + \frac{\frac{d_i}{2} ln\left(\frac{d_o}{d_i}\right)}{k_{tube}} + \frac{\frac{d_o}{2} ln\left(\frac{d_o + 2 \cdot t_{frost}}{d_o}\right)}{k_{frost}\left(d_o \cdot l_t \frac{N_{strings}}{A_i}\right)}} \tag{2.68}$$

Since no phase change occurs in the inner flowing water of an air-to-water heat exchanger, the mass transfer due convection inside tubes doesn't have to be considered.

The internal heat transfer rate calculation between the water bulk condition and the internal tube surface hinges on the determination of the convective heat transfer coefficient for different flow conditions.

The fluid temperature inside a duct varies across its section and, in contrast with external flows, no well-defined free stream condition can be identified. Hence, is necessary the definition of the mean bulk temperature $T_{w,b}$ over the tube cross section. In accordance with Newton's law of cooling, the mean bulk temperature $T_{w,b}$, multiplied by the mass flow rate $\dot{m}_w$ and the specific heat $c_{p,w}$, provides the rate at which enthalpy is advected with the fluid as it moves along the duct:

$$\dot{q} = h_i\left(T_s - T_{w,b}\right) \tag{2.69}$$

Hence, it follows that the mean bulk temperature $T_{w,b}$ may be defined as [1]:

$$T_{w,b} = \frac{\int_{A_{cs}} \rho_w \, v_{w,av} \, c_{p,w} \, T_w \, dA}{\dot{m}_w \, c_{p,w}} \tag{2.70}$$

The evaluation of the internal convective heat transfer coefficient h_i, requires to determine how $T_{w,b}$ varies with the position along the tube. This temperature distribution is also useful to relate the total convection heat transfer $\dot{Q}$ to the temperatures difference at the tube inlet and outlet in the form:

$$\dot{Q}_w = \dot{m}_w c_{p,w}\left(T_{w,b,in} - T_{w,b,out}\right) \tag{2.71}$$

Internal flows involve the existence of entrance and fully developed regions. In the entry region, the velocity and the temperature are subjected of continuous changing of their profiles across the tube section. The flow is said to be fully developed, when the velocity (or the temperature) profile no longer changes with increasing of the distance from the entrance border. The extent of the velocity entry regions depends on whether the flow is laminar or turbulent. Usually, this condition can be identified by the Reynolds number Re_i. In the developed model the internal Reynolds number Re_i for water flow inside a tube is defined as:

$$Re_i = \frac{\rho_w \, v_{w,av} \, d_{h,i}}{\mu_w} = \frac{\dot{m}_w \, d_{h,i}}{A_{cs} \, \mu_w} \tag{2.72}$$

where $d_{h,i}$ is the hydraulic diameter of the tube, defined in the following equation where P is the wetted internal tube perimeter:

$$d_{h,i} = \frac{4 \, A_{cs}}{P} \tag{2.73}$$

Because in the model only round tube are considered, the internal hydraulic diameter coincides with the internal tube diameter hydraulic d_i.

The critical Reynolds number Re_i corresponding to the onset of turbulence inside a tube is typically near 2300, although much larger numbers are needed to achieve fully turbulent conditions ($Re_i \approx 10000$).

Analytical solutions and experimental correlations to determine the convection coefficients h_i are usually expressed in terms of internal Nusselt number Nu_i. These formulations are expressed for fully developed velocity and temperature profiles, for thermal entry length only, fully developed velocity profile only and for combined thermal and hydrodynamic entry length [16].

The solutions for thermal fully developed flow are usually available for constant surface temperature T_s or constant specific rate of heat transfer $\dot{q}$. The temperature distribution associated to fully developed laminar flow of an incompressible, constant property fluid can be determined through the solutions of the differential momentum and energy equations.

For laminar entry region, analytical solutions for both velocity and thermal entry length have been obtained (i.e. [16],[17] and [18]). Usually the location at which heat transfer occurs is preceded by an unheated starting length. Thus, is a commonly assumed that the thermal condition develops in the presence of fully developed hydrodynamic profile.

Table 2.2 Most common Nusselt number correlations for laminar flow in circular tube

Correlation	Authors	Applicability range
$Nu = 3.66 + \frac{0.0668 \, Re \, \mathrm{Pr} \, d_{h,i}/l_{tube}}{1 + 0.04 \left(Re \, \mathrm{Pr} \, d_{h,i}/l_{tube}\right)^{2/3}}$	Hausen [17]	Valid for thermal entry length, hydrodynamic fully developed flow in a round tube at constant wall temperature $Pr \geq 5$
$Nu = 1.86 \cdot \left(\frac{Re \, Pr}{d_{h,i}/l_{tube}}\right)^{1/3} \left(\frac{\mu}{\mu_s}\right)^{0.14}$	Sieder & Tate [19]	Valid for thermal and hydrodynamic entry length, circular tube at constant wall temperature $0.6 \leq Pr \leq 5$ $0.0044 \leq \left(\frac{\mu}{\mu_s}\right) \leq 9.75$

$1/Gz > 0.03$	$Nu = 4.364 + 0.0722\ Gz$	Shah & London [20]	Valid for hydrodynamic fully developed flow in circular tube and constant heat flux between tube wall and fluid $\left(Gz = \frac{d_{h,i}\ Re\ Pr}{l_{tube}}\right)$
$1/Gz \leq 0.03$	$Nu = 1.953\ Gz^{1/3}$		

In literature, it is possible to find many other expressions of the laminar Nusselt number Nu for different cross section and surface conditions. These results have been compiled in a monograph by Shah & London [20] and in updated review by Shah et al. [21]

In the model, internal flows are considered laminar when the Reynolds number Re_i results under 2000. In this case, the adopted correlations are the two presented by Shah & London [20] in terms of Nusselt number Nu. It has to be mentiondend that in the evaluation of the the Graetz number Gz the tube length l_{tube} must be substitute by the length of the equivalent circuit length $l_{t,ref}$ in a row defined in chapter 4:

$$Gz = \frac{d_{h,i}\ Re_i\ Pr_w}{l_{t,ref}} \tag{2.74}$$

Because of its paramount importance in a large number engineering problems, turbulent flow inside round tubes has been intensively studied by many authors. These studied results in developing a large number of empirical correlations. A list of the most used correlation and their application range could be found in the work of Incropera et al. [1] (Other correlations are given in [16], [22], [23] and [12]). Since, the turbulent problem results much more complicated to study than the laminar one, no analytical solutions are available.

Table 2.3 Examples of Nusselt number correlations for fully developed turbulent flow in circular tube

Correlation	Authors	Applicability range
$Nu = 0.023\ Re^{4/5} Pr^n$ $n = 0.4$ for heating $n = 0.3$ for heating	Winterton [24]	Fully developed (hydrodynamically and thermally) turbulent flow in smooth circular tube $0.6 \leq Pr \leq 160$ $Re \geq 10000$ $\frac{d_{h,i}}{l_{tube}} \geq 10$
$Nu = 0.027\ Re^{4/5}\ Pr^{1/3} \left(\frac{\mu}{\mu_s}\right)^{0.14}$	Sieder & Tate [19]	Fully developed (hydrodynamically and thermally) turbulent flow in

		smooth circular tube $0.7 \leq Pr \leq 16700$ $Re \geq 10000$ $\frac{d_{h,i}}{l_{tube}} \geq 10$
$Nu = \frac{(f/8) \cdot (Re - 1000) \cdot Pr}{1 + 12.7\,(f/8)^{1/2}(Pr^{2/3} - 1)}$	Gnielinski [25]	Fully developed (hydrodynamically and thermally) turbulent flow in smooth circular tube $0.5 \leq Pr \leq 2000$ $3000 \leq Re \leq 500000$ $\frac{d_{h,i}}{l_{tube}} \geq 10$

The first correlations are the most used equations named Dittus-Boelter's and reviewed Dittus-Boelter's correlations. As pointed by Incropera et al. [1], errors as large as 25 % may results from the use of these two correlations. Such errors may be reduced to less than 10 % through the use of more recent, but generally more complex correlations (see [21], [26]). The third correlation reported in Table 2.3, which applies for both uniform surface heat flux and temperature, is valid over a large Reynolds number Re range (including transition region). It requires determining the friction factor f (see paragraph 2.3.1). In fact, for turbulent flow, the heat transfer coefficient h_i increase with wall roughness. However, although the general trends is to increase h_i with f, the increase in the friction factor is proportionally larger: when f is approximaly four times the corresponding value for smooth surface, h_i no longer changes [1].

Even if fully internal developed turbulent flow are usually reach for Reynolds number Re_i around 10000, in the model it has been consider turbulent flow for Reynolds number Re_i over 4000. This is possible thanks to the use of Gnielinski's correlation [25], which was developed also for transitional flow. As reported by Kröger [12], to account for the different behaviour when a fluid is heated or cooled, it is opportune to correct Gnielinski's correlation with Petukhov factor $f_P[26]$. This factor is defined as:

$$\begin{aligned} T_w > T_a \qquad & f_P = \left(\frac{Pr_w}{Pr_a}\right)^{0.25} \\ T_w < T_a \qquad & f_P = \left(\frac{Pr_w}{Pr_a}\right)^{0.11} \end{aligned} \tag{2.75}$$

Hence, the equation used for turbulent flow results:

$$Nu = \frac{(f/8) \cdot (Re_i - 1000) \cdot Pr_w}{1 + 12.7\,(f/8)^{1/2}(Pr^{2/3} - 1)} \cdot f_P \tag{2.76}$$

where the friction factor f is calculated as reported in paragraph 2.3.1.

Since entry length for turbulent flow are typically short, errors of less than 15% are associated assuming that the average Nusselt number Nu_i for the entire duct is equal to the value associated with the fully developed region.

For the transitional region, typically for internal Reynolds number Re_i between 2300 and 10000, caution should be exercised when applying turbulent flow correlation. Incropera et al. [1] suggest that for a first approximation a smaller Re_i can be used in the turbulent correlation. However, Gnielinski's correlation provides a higher level of accuracy because it was specifically developed for the transition region too.

In this model, as adopted by Bettoni & D'Antoni [27], a linear interpolation between the Shah & London's correlation at Re_i = 2000 and the corrected Gnielinski's correlation at Re_i = 4000 has been considered.

It has to be mentioned that during normal operations, internal surfaces become often fouled as result of subsequent depositions of film or scale. This accumulation can greatly reduce the heat transfer rate between water and the adjoining surface. Fouling inside tubes is governed by varied and complex phenomena. In general it mainly depends on the nature of the flowing fluid and on the internal surface conditions.

Considerable effort (see [28] and [29]) has been directed towards the understanding of fouling mechanism, nevertheless no reliable techniques are yet available for the prediction [22] of the internal fouling factor $R_{f,i}$. Hence fouling effects has been not considered in the development of the model.

Assuming a steady-state, one dimensional conduction between two surface of a solid, the analogy between heat and electrical charge diffusion, leads to the following expression of the conductive heat transfer flux $\dot{q}_k$:

$$\dot{q}_k = \frac{1}{R_k}\left(T_{s,i} - T_{s,o}\right) \tag{2.77}$$

where R_k is the thermal resistance for conduction in a wall, $T_{s,o}$ and $T_{s,i}$ are the external and internal surface temperatures, respectively.

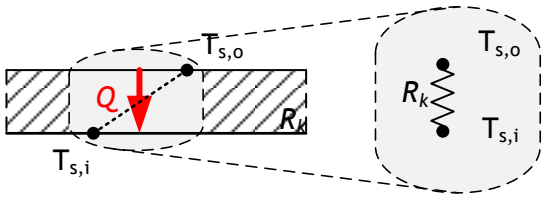

Figure 2.10 One-dimensional steady-state heat conduction through a solid wall

The expression of the thermal conduction resistance R_k depends on the value of the thermal conductivities k_{wall} and on the temperature distribution within the solid, which is established from the solution of the heat conduction equation for a proper geometry:

$$R_k = f(k_{wall}, wall\ geometry) \tag{2.78}$$

In literature (see [22], [1] and [23]) may be found expressions of the thermal conduction resistance R_k for the more common wall geometry applied in heat transfer.

If the thermal specific conductivity of the wall material k_{wall} is known, its conduction resistance R_k can be obtained by the analysis of the heat diffusion through the barrier between hot and cold surface.

The most common tube geometry applied to heat exchanger is the hollow cylinder. Generally, heat flow through a cylinder wall is characterized by a two-dimensional conduction, across and along the tubes. Since the axial heat transfer along heat exchanger

tubes is usually negligible compared to the radial heat transfer, one-dimensional heat transfer hypothesis may be considered valid.

Furthermore, it can be assumed steady-state conduction because the surface temperature at each point remains constant with time.

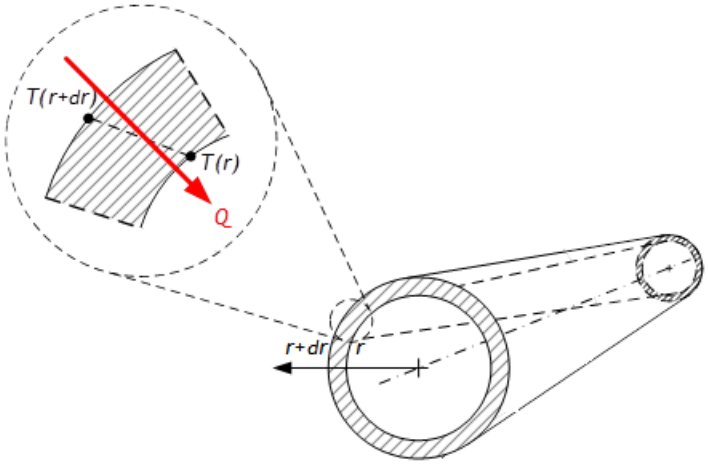

Figure 2.11 One-dimensional heat conduction in a hollow cylinder

Since the properties of the wall material have no significant variations in the working temperature range of air-to-water heat exchanger, the thermal heat conductivity of the tube k_{tube} is considered to be constant.

From the formulation of the temperature distribution in a thick-walled hollow cylinder of constant thermal conductivity k_{tube} [1], the heat flux expression can obtained:

$$\dot{q}_k(r) = -k_{tube}\frac{dT(r)}{dr} = -\frac{k_{tube}}{r}\frac{T_{s,o} - T_{s,i}}{ln(r_o/r_i)} \tag{2.79}$$

Rearranging the previous relationship in accordance to equation 2.76, leads to express the conductive thermal resistance of a circular tube as:

$$(R_k A)_{tube} = \frac{ln(r_o/r_i)}{k_{tube}\, A_{tube,i}/r_i} = \frac{ln(r_o/r_i)}{k_{tube}\, 2\,\pi\, l_{tube}} \tag{2.80}$$

where l_{tube} is the is the length of the tube.

Usually in an air-to-water the thickness of the tubes is small, mainly because the pressure range of the water flow is relatively narrow. This, combined with a high value of the wall thermal conductivity k_{wall}, can lead to a negligible conduction resistance compared to water- and air-side thermal resistances.

Under dehumidifying condition, the water vapour contained in the air stream can deposit on the external surface as liquid condensate film or as frost layer.

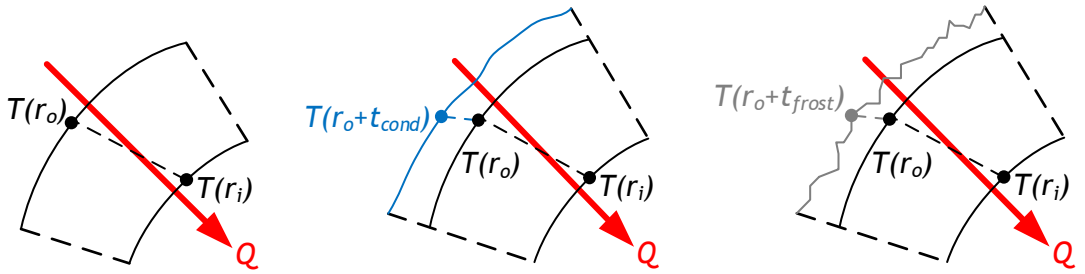

Figure 2.12 One-dimensional heat conduction in a tube under dry, wet and frosted conditions

When liquid condensation occurs, neglecting the water flowing due to gravity or to external forces, it can be assumed that the film thickness t_{cond} and its thermal conductivity k_{cond} are constant values [11] along the surface (see paragraph 2.4). Hence, the deposited water film can be treated as an additional hollow cylinder around the tube.

In accordance with the analysis of the previous paragraph its conductive thermal resistance can be evaluated as:

$$(R_k A)_{cond} = \frac{ln\left((d_o + t_{cond})/d_o\right)}{k_{cond}\, A_{tube,o}/r_o} = \frac{ln\left((d_o + t_{cond})/d_o\right)}{k_{cond}\; 2\,\pi\, l_{tube}} \tag{2.81}$$

The resulting specific thermal resistance of a wetted cylindrical tube is consequently given as:

$$R_{k,wt} = \frac{ln(d_o/d_i)}{k_{tube}/r_i} + \frac{ln\left((d_o + t_{cond})/d_o\right)}{k_{cond}/r_o} \tag{2.82}$$

Coney et al. [30] conducted a theoretical study on heat transfer performance of fin-tubes heat exchanger under dehumidifying condition. They concluded that the effect of condensate film thermal resistance can be neglected without introducing significant error for normal conditions encountered in practice. Their theoretical predictions has been confirmed by experimental study [31].

Thermal conduction in frosted tube requires some additional considerations, the thermal conductivity k_{frost} in frost layer is not a constant value along the it thickness t_{frost}. This can be attribute at the fact that a frost layer is usually formed by consecutives frost depositions, which leads to different values of density due water vapour permeation and frost growth process (see paragraph 2.7). Furthermore, the thickness t_{frost} of a frost layer is usually not uniform along the surface. Thus, also the frost layer thickness t_{frost} is not a constant value.

Assuming an average value of the frost thermal conductivity $\bar{k}_{frost}$ and the relative average frost thickness $\bar{t}_{frost}$, it is possible to extend the previous result to this case. The (average) conductive thermal resistance $(R_k A)_{frost}$ of a frost layer grown on the external side of a cylinder can be determined as follow:

$$(R_k A)_{frost} = \frac{ln\left(\left(d_o + \bar{t}_{frost}\right)/d_o\right)}{\bar{k}_{frost}\, A_{tube,o}/r_o} = \frac{ln\left(\left(d_o + \bar{t}_{frost}\right)/d_o\right)}{\bar{k}_{frost}\; 2\,\pi\, l_{tube}} \tag{2.83}$$

Thus, the specific thermal resistance of a frosted cylindrical tube results

$$R_{k,ft} = \frac{ln(d_o/d_i)}{k_{tube}/r_i} + \frac{ln\left(\left(d_o + \bar{t}_{frost}\right)/d_o\right)}{\bar{k}_{frost}/r_o} \tag{2.84}$$

The specific thermal resistance of the tube-fins junction R_{junc} depends very strongly on manufacturing method and on the difference between the thermal expansion coefficients of the two materials.

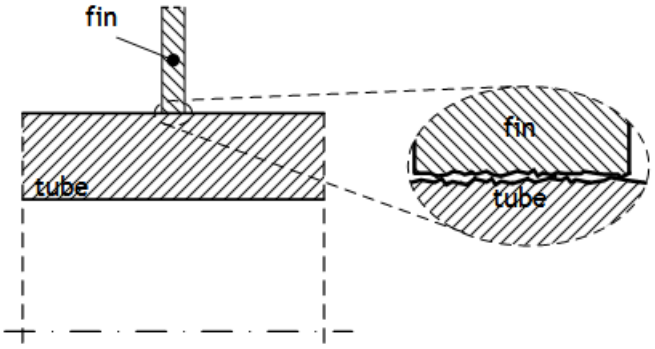

Figure 2.13 Contact gap of tube-fins junction

The imperfect metal-to-metal contact results in a thermal contact resistance component $R_{contact}$ of the junction. Furthermore, if the quality of finned wall is poor or at high temperature, where the fins tend to expand away from the wall, a gap could exist between the two surfaces with no contact pressure. As results an expansion thermal resistance component R_{exp} of the junction must be added:

$$R_{junc} = R_{contact} + R_{exp} \tag{2.85}$$

The subject of thermal metal-to-metal contact resistance has been studied by numerous investigators. Graphical representations of results for particular finned tube under given conditions are reported by Coetzee & Kröger [32]. These diagrams show the dependence of contact resistance from outside heat transfer coefficient, outside temperature and production contact pressure. The developed analytical methods to evaluate contact and gap components of the junction thermal resistance R_{junc} are of difficult application in practical use. These methods request the known of many distinctive parameters of materials, manufacturing and junction-surface conditions, which usually are not available.

Elsherbini et al. [33] conducted an experimental investigation of thermal contact resistance in an aluminium plain-fin and copper tube heat exchanger with collarless fins. They examined two different coil: one in the as manufactured condition and the other with brazed fin-tube joints. The results show significant contact resistance only in the production heat exchanger when operating under dry conditions. Brazed fins present insignificant value of the junction resistance R_{junc}. Furthermore, when frost is formed on the surface, the contact resistance of the production heat exchanger drops drammatically to the brazed fins value. These results were in accordance with previous studies.

The studied geometry presents brazed fins, hence in the developed model the fin-tube junction resistance R_{junc} is neglected.

2.3.1 Internal pressure drop and friction factor

Pressure drop is one of the variables that have great effect on the performance and on the operating cost of a heat exchanger. In particular, it allows determining the power consumption required to fan and pumping. In fact, if $\dot{m}$ is the mass flow rate, the pumping power $\dot{W}$ requires to get the fluid through the heat exchanger against the pressure drop Δp becomes:

$$\dot{W} = \dot{m}_w \, \Delta p \tag{2.86}$$

To determine the pressure drop Δp needed to sustain the internal flow, it is usual to work with the Moody friction factor f, which is a dimensionless parameter defined as [1]:

$$f = -\frac{d_{h,i}}{\rho \, {v_{av}^2}/{2}} \cdot \frac{dp}{dx} \tag{2.87}$$

It is important to note that the Moody friction factor f is a different parameter from the Fanning friction factor c_f. In fact, according to equation 2.22 and 2.86, the two parameters are related in the form:

$$f = 4 \, c_f \tag{2.88}$$

To develop a practical relationship for the friction factor is essential to characterize the velocity profile.

For laminar flow of an incompressible, constant property fluid in a fully developed region of a tube, the velocity profile may be readily determined. Since in this region the radial velocity component v_r and the gradient of the axial velocity component $\partial v_z / \partial z$ are everywhere zero, the axial velocity component v_z is independent from the axial position z. Recognizing that in the fully developed region the net momentum flux is everywhere zero, the momentum conservation requirement reduces to a simple balance between sheer and pressure forces in the flow [22].

Once the hydrodynamic profile of the flow is known, it is possible to relate the friction factor f of a hydrodynamic fully developed laminar flow to the Reynolds number Re, in the form:

$$f = c \, \frac{1}{Re_i} \tag{2.89}$$

where c is a constant depending on the cross sectional form of the duct.

Since for fully developed turbulent flow, the analysis is much more complicated than for laminar flow, a purely theoretical approach is to avoid. In this case some empiricism is introduced in its derivation because a semi-empirical velocity profile is used in the analysis.

Experiments show that, in addition to depending on the Reynolds number Re, the friction factor f is a function of the tube surface condition, evaluated through the relative surface roughness e/d_h. For smooth surface, the friction factor has a minimum and increases with the surface roughness. Friction factors f for a wide Reynolds number range are presented in the Moody diagram.

Valid alternatives to the use of Moody diagram are simpler but approximated expressions, like the next equation, developed [34] for turbulent flow and smooth reasonable surface condition:

$$f = (1{,}82\log(Re_i) - 1{,}64)^{-2} \tag{2.90}$$

This equation is used in the model to quantify the friction factor f needed in the correlation for the internal convective heat transfer coefficient.

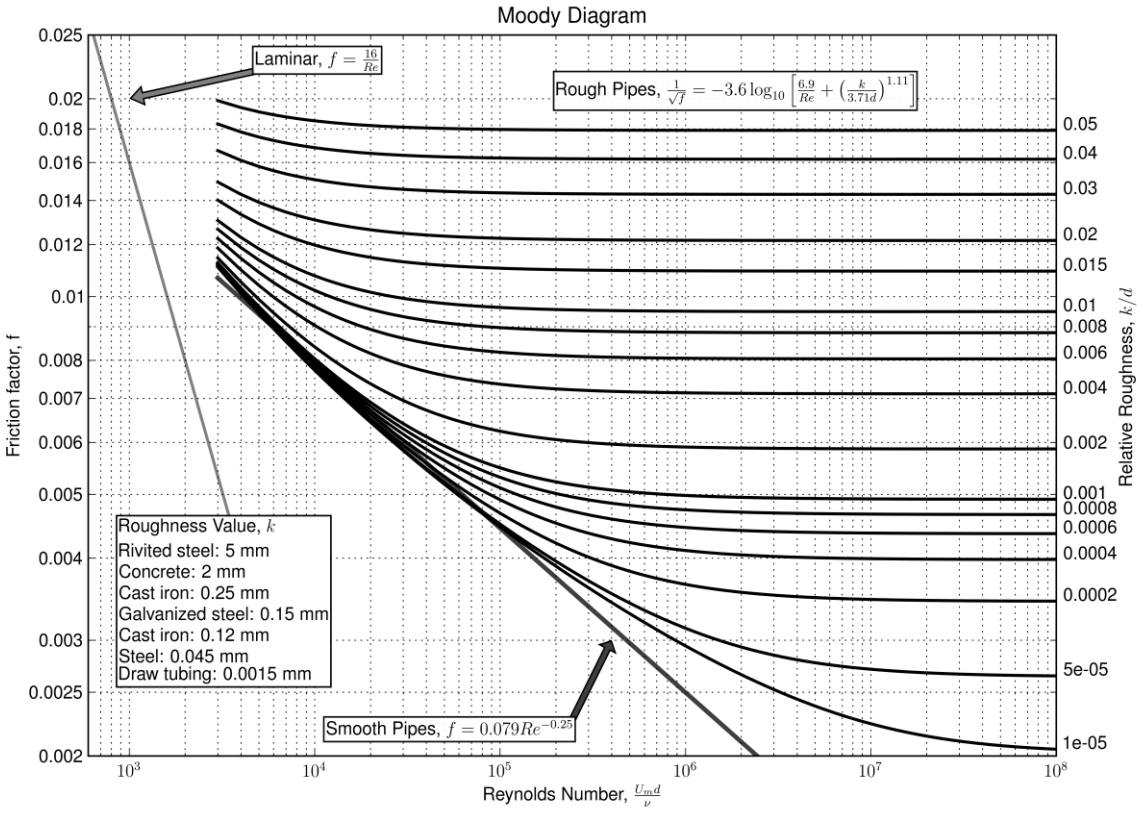

Figure 2.14 Moody diagram

If the flow conditions (Re) and the inside surface condition (e/d_h) of the duct are known, the pressure drop over the length of the tube l can be determined according to next the relationship [22]:

$$\Delta p = f\left(\frac{l}{d_h}\right)\frac{\rho\, v_{av}^2}{2} \tag{2.91}$$

However, it is important to clarify that the determination of the total pressure drop requires also the evaluation of the local pressure losses, due the hydraulic resistance of local variation in the flow condition (presence of valves, curves, abrupt variation of tube diameter), and the pressure losses in the rest of the hydraulic circuit.

2.4 External heat and mass transfer

In practical applications of air-to-water heat exchanger, the dominant thermal resistance is on the air-side. In fact the air specific thermal properties are really low compared to those of water. This results in low values of the external convective heat transfer coefficient h_o. For this reason, fins are attached to the external surface of the heat exchanger in order to extend the heat transfer area A_o and improve the heat exchanger performance. The addition of fins also increases the thermal conductive resistance over

the portion of tubes where the fins are attached. However, the global effects is an enhancement in the heat transfer rate between the surface and the adjoining air.

Fins are attached to the primary surface by brazing, soldering, welding, adhesive bonding or mechanical expansion, or extruded or integrally connected to tubes. They can assume a variety of geometry — plain, pin, wavy, interrupted fins. The major categories of extended surface heat exchangers are individually finned tubes and flat fins with or without enhancements/ interruptions on an array of tubes. Banks of finned tubes usually present annular fin or plain. Annular fin is one that is circumferentially attached to a cylinder, whereas plain fin is a sheet of high conductive material that is attached to one or more tubes.

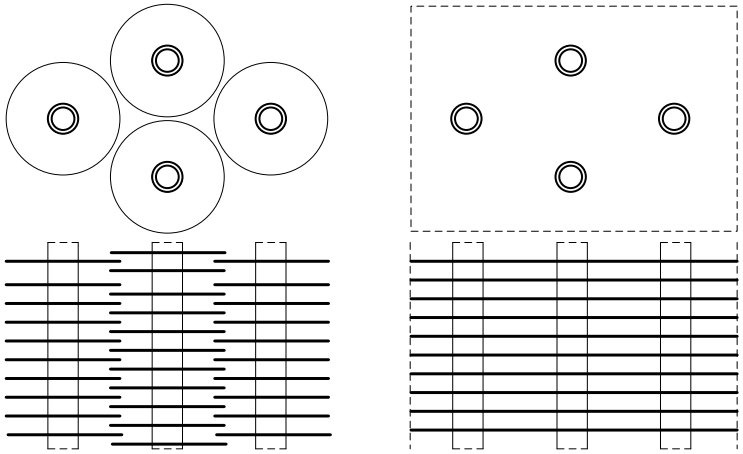

Figure 2.15 Schematic of typical finned-tube heat exchanger: annular plain fins and countinuous plain fins

High efficiency heat exchangers use enhanced fin geometry, such as louvered, interrupted and slit fins. Plain fins are more common in compact configuration, as in air-to-water heat exchangers. This geometry, is used in the air-conditioning/refrigeration industry as well as in applications where the pressure drop on the fin side prohibits the use of enhanced flat fins.

The primary interest is knowing the extent to which particular extended surfaces of fin arrangements could improve heat transfer from a surface to the surrounding fluid. It is important to know the influence degree to which the heat transfer rate is varied by applying fins to a surface.

Extended surface performance is commonly expressed in terms of heat transfer coefficient and fin efficiency η_{fin}, which is defined as the ratio of the actual fin heat transfer rate to the heat transfer rate that would exist if the entire fin surface were at the base temperature. Determining the heat flow through a fin requires the knowledge the temperature distribution along the fin.

2.4.1 Convective heat and mass transfer coefficients for forced flow across a finned bank of tubes

In general, convective heat transfer coefficient h_o is a complex function of the surface geometry, fluid properties and flow conditions. It can be expressed in terms of Colburn j factors, as seen in the paragraph 2.1:

$$0{,}6 < \mathrm{Pr}_a < 60 \qquad j = St_o\, Pr_a^{\,2/3} \tag{2.92}$$

The thermal Stanton number St_o is related to the Nusselt Nu_o, to Reynolds Re_o and Prandtl Pr_a numbers according to the next equation:

$$St_o = \frac{Nu_o}{Re_o\, Pr_a} \tag{2.93}$$

The definition of the Reynolds number Re_o for external flow is based on the maximum flow velocity v_{max} and the external hydraulic diameter of the passage $d_{h,o}$:

$$Re_o = \frac{\rho\, v_{max}\, d_{h,o}}{\mu} \tag{2.94}$$

The maximum flow velocity is determined as follow:

$$v_{max} = \frac{\dot{m}_a}{\rho_a\ A_{ff}} \tag{2.95}$$

where A_{ff} is defined as the minimum free-flow area available for the flow, identified by the evaluation of the compactness the finned passages σ:

$$A_{ff} = \sigma\, A_{fr} \tag{2.96}$$

where A_{fr} is the external frontal area of the heat exchanger.

Hence, for a compact heat exchanger, thermal Stanton number St can be determined as follow:

$$St_o = \frac{Nu_o}{Re_o\, Pr_a} = \frac{h}{\dot{m}_a\, c_{p,a}}\, A_{ff} \tag{2.97}$$

As for internal flows, the heat transfer coefficient of convection over an external surface is characterized by its flow condition. In particular, for flow over staggered tube banks, the transition from laminar to turbulent flow is more gradual than in flow through a single tube, whereas for aligned tube bundles the transition phenomena resemble those observed on tube flow. In either case, transition from laminar to turbulent flow begins at a Re_o of about 100, and the flow becomes fully turbulent at Re_o of about 3000 [22].

In general, heat transfer enhancement is favoured by the more tortuous flow over a staggered arrangement, particularly for small Reynolds number ($Re_o \leq 100$). Since the air-side thermal resistance is usually much greater than that on the water side, fins were applied to the air-side surface to enhance its heat transfer area. To determine the overall fins efficiency of the array of fins $\eta_{s,o}$, is essential to known their efficiency η_{fin} and the ratio of fin to total heat transfer surface $A_{o,fin}/A_o$.

The available relationship for convective heat transfer coefficients, h in flow over an air-to-liquid heat exchanger are based entirely on experimental data, because the airflow is too complex to be treaded analytically (However analytical study were effectuated [21])

In their classic work, Kays & London [4] provide a large number of Colburn-j factor data for different compact heat exchangers core using air as working fluid. They include many types of fins design, as well as different cross-section duct configurations. For each configuration the value of the geometrical parameters, among which $d_{h,o}$, σ and $A_{o,fin}/A_o$, are listed. 10^3

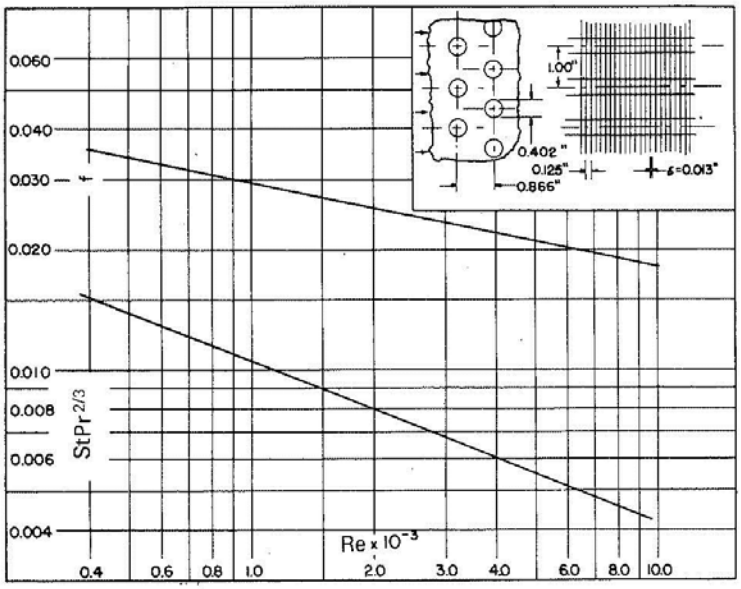

Figure 2.16 Compact heat exchanger finned circular tube, surface 8.0-3/8T: Colburn ***j*** factor (and friction factor ***f***) [4]

Experimental heat transfer data for representative coils, where typically plotted as Colburn-j factor j_o against Reynolds number Re_o in the form:

$$j_o = c_1 \, {Re_o}^{c_2} \tag{2.98}$$

Elmahdy & Biggs [35] reported that for Reynolds number Re_o range from 200 to 2000, the coefficients c_1 and c_2 are constants for a particular coil and are dependent only on its geometrical characteristics, namely fin thickness t_{fin}, spacing s_{fin} and height h_{fin} and coil hydraulic diameter $d_{h,o}$.

$$c_1 = f\left(t_{fin}, h_{fin}, d_{h,o}\right) \quad ; \quad c_2 = f\left(t_{fin}, s_{fin}, h_{fin}\right) \tag{2.99}$$

In the developed model, the two the coefficients c_1 and c_2, which relate the Colburn-j factor j_o and Reynolds number Re_o in equation 2.97, are calculated according to Elmahdy & Biggs [35]. After analysing experimental heat transfer data for twenty different heat exchangers, they found that the coefficients can be expressed as:

$$c_1 = 0.159 \left(\frac{t_{fin}}{h_{eq,fin}}\right)^{0.141} \left(\frac{d_{h,o}}{t_{fin}}\right)^{0.065} \tag{2.100}$$

and

$$c_2 = -0.323 \left(\frac{t_{fin}}{h_{eq,fin}}\right)^{0.049} \left(\frac{s_{fin}}{t_{fin}}\right)^{0.077} \tag{2.101}$$

where t_{fin} is the fin thickness, $h_{eq,fin}$ is the fin height, $d_{h,o}$ is the external hydraulic diameter and s_{fin} is the fin spacing. As specified by the authors, for continuous flat plate fin, the fin height $h_{eq,fin}$ is evaluated through the equivalent fin radius base on an equivalent circular area of a non-circular fin (see paragraph 2.4.2). The coefficients c_1 and c_2 are calculated accounting the possible variation of the geometrical parameters due the presence of the frost layer at each row.

The reported equations are only valid where the values of the dimensionless group used in the regression analysis fall in the range of variables considered. The applicability range of the equations are reported in next table.

Table 2.4 Dimensionless groups used in the regression analysis of Elmahdy & Biggs [35]

Dimensionless group		$\frac{d_{h,o}}{t_{fin}}$	$\frac{t_{fin}}{h_{eq,fin}}$	$\frac{2 \cdot r_{eq,fin}}{P_l}$	$\frac{s_{fin}}{t_{fin}}$	$\frac{2 \cdot r_{eq,fin}}{P_t}$	$\frac{d_o}{2 \cdot r_{eq,fin}}$	σ	Re_o
Validity range	**from**	3	0.01	0.87	2	0.76	0.37	0.35	200
	To	33	0.45	1.27	25	1.4	0.85	0.62	2000
Calculated value for Sortech AG re-cooler RCS 08		23.6	0.011	*1.6*	16	0.8	*0.35*	*0.674*	\

Table 6.1 shows that three of the seven calculated dimensionless group for the chosen coil geometry (Sortech AG re-cooler RCS 08), are slightly outside the applicability range of Elmahdy & Biggs. That can be explain by the difference in the tubes bank arrangement. In fact, none of the 20 heat exchangers used in their experiment present a longitudinal tube pitch P_l half of the transversal tube pitch P_t as the studied geometry present. This two parameters are involved in the determination of the equivalent fin radius $r_{eq,fin}$, the equivalent fin height $h_{eq,fin}$, and the coil compactness σ. Hence, they have directly and indirectly consequence on the all the dimensionless groups (except for the 4th).

Without taking into account of the frost layer, the resulting values of the the coefficients c_1 and c_2 are 0,104 And -0,321, respectively. Hence,

$$j_o = 0{,}104\ {Re_o}^{-0{,}321} \tag{2.102}$$

Furthermore a graphical comparison between the diagrams for the most similar geometry reported by Kays and London [4], namely surface 8.0-3/8T for finned circular tubes, and the equation obtained from Elmahdy & Biggs's were done. This comparison shows that the two results are in good agreement.

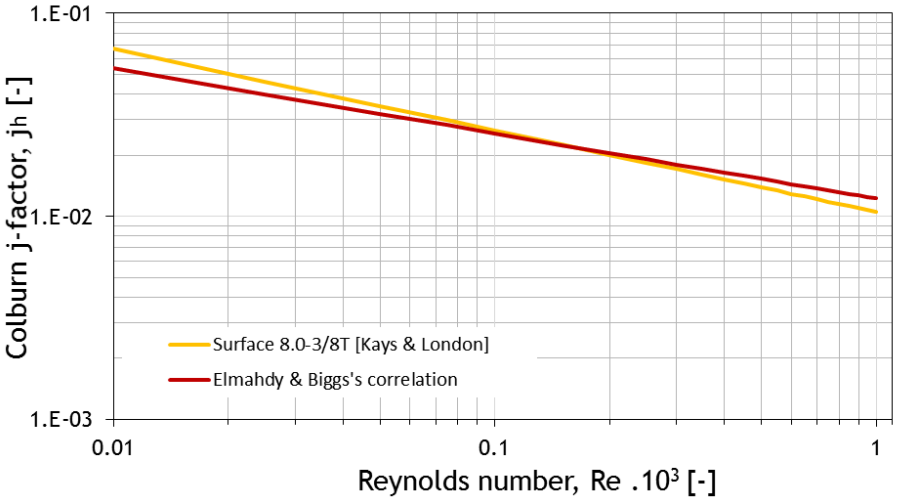

Figure 2.17 – Comparison between Colburn-j factor j_o against Reynolds number Re_o for surface 8.0-3/8T surfaces [4] and for resulting equation 2.102

The condensate retained on the surface of a heat exchanger has hydrodynamic effects by changing the surface geometry and the airflow pattern. Furthermore, the water layer on the surface increases local surface thermal resistance.

As pointed by Threlkeld [11] it is very difficult to accurately predict the external heat transfer coefficient. Many experiments were conducted by different authors to obtain valid correlations for heat transfer to external surfaces both for dry- (cooling without dehumidification) and for wet-surface condition (cooling and dehumidification). The results shown different trends for convective heat transfer coefficient over wet surfaces compared to that obtained in dry condition.

In 2001 Park and Jacobi developed a robust review on air-side performance characteristics of round- and flat-tube heat exchangers [36]. They reported that most investigations of heat exchanger performance under wet conditions consider only fully wet surface (when its temperature is lower than the dew point throughout the entire heat exchanger). Although partially wet conditions occur in application (when condensation is taking place only on a part of the surface), researchers have avoided this situation because it complicates experimental interpretation. It would be necessary to consider the dry- and wet-surface fin area separately for proper fin efficiency calculation. Unfortunately, observations of local surface conditions are difficult and may not be very effective, because the presence of dropwise condensation is sometimes difficult to judge visually.

McQuiston [37] found an increase of both heat transfer and friction under wet conditions and reported that is higher for dropwise condensation than filmwise condensation. McQuiston [38] also reported that the increase of the Colburn j-factor under wet conditions was insignificant at very low Reynolds numbers. As earlier explained by Guillory & McQuiston [39], condensate on a smooth wall can have a similar effect as that due to increasing surface roughness. The effect of surface roughness and a transition from laminar to turbulent flow under wet conditions reported by Tree and Helmer [40] may explain the enhanced heat transfer at high Reynolds numbers. Jacobi & Goldschmidt [41] explained that condensate at low Reynolds numbers is retained in a way that has detrimental effect on heat transfer: the effect diminishes as the air velocity increases and less condensate is retained.

Many other investigators agree with McQuiston on the increase of the friction factor under wet condition, but there is not uniform agreement that the heat transfer coefficient increases under wet conditions.

As example, Wang et al. [43] found that the Colburn j-factor decreases under wet condition for low Reynolds numbers (Re_o < 2000), and that is nearly the same or slightly higher than dry conditions for high Reynolds numbers (Re_o > 2000). In their work, Korte & Jacobi [42] showed in an experimental study of condensate drainage characteristics that the mass of retained condensate decreases as air velocity increases. The presence of the condensate can degrade heat transfer by occupying surface area and even blocking airflow. The decreased retention at high velocities explains why both friction and heat transfer coefficients under wet conditions differ from dry conditions by less at higher Reynolds numbers for plain-fin-and-tube heat exchangers.

Discrepancies were found in the literature also on the effect of relative humidity. These can probably be attributed to the differences in wet-fin efficiency calculation method. Many authors [43] [44] found a negligible effect of relative humidity on the convective heat transfer coefficient factor under fully wet surface adopting Threlkeld derived fin efficiency methods.

Hence, because it's impossible to identify a common trends for the heat transfer characteristics under condensing condition, the convective heat transfer rate calculated

using Elmadhy & Biggs [35] correlation for dry condition is maintained for wet condition too.

Although the frosting condition is similar to condensation in that it includes simultaneous heat and mass transfer to the surface, the frosting condition is different from condensation because of the absence of drainage: the condensate water vapour accumulates as frost on external surface. Therefore, Park and Jacobi [36] reported that true steady-state performance data cannot be obtained for frosting condition in the same way as for the condensing condition. The change of performance during the test period are time dependent. The overall heat transfer coefficient initially increases by a surface roughness effect and later decreases due to the growing insulating effect of the frost layer (frost layer thickness, density, and thermal conductivity).

In Park and Jacobi reviews [36] is reported that since that early work, there have been discrepancies as to the change of overall heat transfer coefficient with time.

Emery and Siegel [45] fitted the ratio of heat transfer coefficient under frosting conditions to that under dry conditions as a function of the difference between the air free-stream specific humidity and the saturated specific humidity at the surface temperature. They reported that the initial influence of frost on heat exchanger performance depend on frost growth history which is determined by several operational parameters, but the frost effect after the early period depends only on specific humidity. They found that the heat transfer coefficient, after an early degradation, remains nearly constant for frost accumulation from 8 to 50 kg/m^2. They suggested the combined effects of an increase of local air velocity and an increase of frost thermal conductivity by frost densification compensate for the increase of frost thickness.

Rite and Crawford [46] reported a constant frosting rate over a test period of several hours and a small influence of the airflow rate on the frosting rate. They explained these findings as due to the increased local air velocity and mass transfer coefficient accompanying a blockage effect. Rite and Crawford found an increase in overall heat transfer coefficient over the test period, and they attributed it to an increase in heat transfer coefficient through the surface roughness effect by frost.

Kondepudi and O'Neal [47] reported that the overall heat transfer coefficient remains nearly constant in time while the airflow rate is maintained constant. They suggested that the heat transfer coefficient decrease reported by others might have been caused by a decrease in airflow rate.

All experiments by Emery and Siegel [45], Rite and Crawford [46], and Kondepudi and O'Neal [47] were conducted while the air flow rate was maintained constant, and their reports showed a constant or slightly increasing heat transfer coefficient over the test period.

In usual application, the airflow rate is determined by a fixed fan power and the accumulation of frost is likely to be accompanied by a decrease in heat transfer coefficient.

In the model the effect of the frost layer has been considered to have two opposite effects on the heat transfer rate: the obstruction of the free flow area, cause an increment in the convective heat transfer rate due to the increased external Reynolds number whereas the presence of an additional insulating layer cause a increment in the surface conductive thermal resistance. The effect of the initial surface roughness resulting in the rise of turbulent intensity and of the heat transfer coefficient is neglected. This because no practical criteria were developed to define to initial time during this phenomenon occurs.

Furthermore, in literature no correlations that can take into account of this effect were found.

2.4.2 Extended surface effectiveness

Even though conduction within the fins is actually two-dimensional, the analysis may be simplified to one-dimensional steady-state conduction. In fact the temperature differences in the transverse direction are small compared to the difference between surface and the surround.

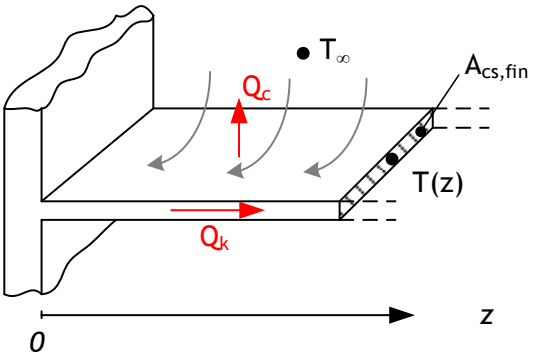

Figure 2.18 One dimensional conduction in fin of constant cross section.

Furthermore, although the installation of fins will alter the surface convection coefficient, this effect is commonly neglected and the also the thermal conductivity of the fin k_{fin} could be assume constant.

The steady-state energy balance applied to an infinitesimal control volume of a fin with constant cross-sectional area $A_{cs,fin}$, as well as convective heat transfer coefficient h and thermal conductivity k_{fin}, is expressed as [23]:

$$\frac{\partial^2 T(x)}{\partial z^2} - \frac{h\, P_{cs,fin}}{A_{cs,fin}\, k_{fin}} (T(z) - T_\infty) = 0 \tag{2.103}$$

where $P_{cs,fin}$ is the perimeter of the fin cross-section and T_∞ is the free stream temperature of the adjoining fluid.

Often to compact the expression, a parameter ξ, which represent the physical and geometrical properties of the fin, is introduced as

$$\xi = \sqrt{\frac{h\, P_{cs,fin}}{k_{fin}\, A_{cs,fin}}} \qquad \left[\frac{1}{\mathrm{m}}\right] \tag{2.104}$$

It useful to note that the fin parameter ξ can be interpreted as a modified expression of the Biot number Bi, a fundamental dimensionless number in conduction problem that involve surface convection effects. It provides a measure of the temperature drop in a solid relative to the temperature difference between the surface and the adjoining fluid. The expression of the Biot number Bi for a fin is:

$$Bi = \frac{h\, A_{cs,fin}}{k_{fin}\, P_{cs,fin}} \tag{2.105}$$

The Biot number Bi may be also associated with the more intuitive interpretation as ratio between conductive and convective thermal resistances.

The solution of the one-dimensional fin equation is subjected to the assignment of appropriate boundary conditions at the base and at the tip of the fin. Usually for the fin base temperature $T(0)$ is assumed the temperature of at the prime surface on which the fin is attached $T_{s,prime}$. At the fin tip several different physical situations are possible: for long fin, the fin tip temperature $T(l_{fin\,tip})$ could be assumed equal to the fluid temperature T_∞; because the cross-sectional area is usually small compared to the lateral area of the fin, in many situations the heat transferred from the fin tip can be neglected; a physically more realistic situation is the one where heat convective transfer between fin tip and surrounding fluid is accounted.

Once the temperature distribution is known, the heat transfer rate through the fin $\dot{Q}_f$ can be determined. In general, it can be expressed in the form:

$$\dot{Q} = f\left(\xi, l_{fin}, \left(T_{s,prime} - T_\infty\right)\right) \tag{2.106}$$

where l_{fin} is the fin characteristic length, which depends from its geometry.

The fin effectiveness ε_{fin} is defined [1] as the ratio of the actual fin heat transfer rate $\dot{Q}_{fin}$ and the heat transfer rate that would exist without the fin $\dot{Q}$. Therefore, it follows:

$$\varepsilon_{fin} = \frac{\dot{Q}_{fin}}{\dot{Q}} = \frac{\dot{Q}_{fin}}{h\,A_{cs,fin}\left(T_{s,prime} - T_\infty\right)} \tag{2.107}$$

Fin effectiveness ε_{fin} expresses the ratio of conductive and convective thermal resistance. To enhance the heat transfer, the fin overall thermal resistance must not exceed that due to convection at the exposed base.

The results of heat transfer analysis are usually presented in terms of fin efficiency η_{fin}. The fin efficiency provides the ratio to the actual heat rate transfers through the fin $\dot{Q}_{fin}$ and the maximum heat rate at which a fin could dissipate $\dot{Q}_{fin,max}$. This rate would be reached if the entire surface of the single fin were at the base temperature $T_{s,prime}$. Hence, with a uniform convective coefficient h, the fin efficiency η_{fin} could be defined as [1]:

$$\eta_{fin} = \frac{\dot{Q}_{fin}}{\dot{Q}_{fin,max}} = \frac{\dot{Q}_{fin}}{h\,A_{fin}\left(T_{s,prime} - T_\infty\right)} \tag{2.108}$$

where A_{fin} is the surface area of the fin.

It could be imagined that with condition, the isothermal heat transfer surface would be reduced from A_{fin} to $\eta_{fin}\,A_{fin}$, with constant convective heat transfer coefficient h. Thus, the fin efficiency η_{fin} characterizes the finite conduction resistance of the fin, which leads to a temperature gradient along the fin.

Fin efficiency η_{fin} depends strongly on the geometric characteristic of the fin and, once the temperature distribution is known, can be expressed as:

$$\eta_{fin} = f\left(\xi, l_{fin}, fins\ geometry\right) \tag{2.109}$$

In Gardner's work [48] can be found relationships for η_{fin}, m and l_{fin} for a large number of fin geometries.

For practical applications, an extended heat transfer surface is composed by the fins surfaces A_{fins} and the unfinned portion of the prime surface. As for the fin, the performance of an array of fins and the unfinned prime surface, can be characterized by the definition of the overall surface efficiency η_s, or surface effectiveness [23]:

$$\eta_s = \frac{\dot{Q}}{h\, A_{tot}\left(T_{s,prime} - T_\infty\right)} \tag{2.110}$$

where $\dot{Q}$ is the heat transfer rate through the total (fins plus unfinned prime) surface area A_{tot}.

The previous equation expresses the ratio of the actual heat transfer rate and the maximum possible heat rate, resulting if the entire surface A_{tot} were maintained at the temperature $T_{s,prime}$. If the convective coefficient h is assumed to be equivalent for fins and the unfinned prime surfaces, the heat transfer rate $\dot{Q}$ can be express as:

$$\dot{Q} = h\left(T_{s,prime} - T_\infty\right)\left(A_{fins}\eta_{fin} + \left(A_{tot} - A_{fins}\right)\right) \tag{2.111}$$

Thus, the extended surface efficiency η_s is related to the efficiency of a single fin η_{fin} through the next equation:

$$\eta_s = 1 - \frac{A_{fins}}{A_{tot}}\left(1 - \eta_{fin}\right) \tag{2.112}$$

What is observed in nearly all published papers is that, whatever the fin type (plain, louvered, slit), the fin efficiency calculation is always performed by analytical methods derived from circular fin analysis.

Fin efficiency η_{fin} equations for dry plain circular fins under the aforementioned assumptions are reported in many handbooks [1][22][23]. The analytical solution for circular fin on a round tube with adiabatic fin tip is given by equation 2.112 [1], where I_n and K_n are the modified Bessel functions of first and second kind:

$$\eta_{fin} = 2\frac{r_{tube}}{\xi \cdot h_{fin}^2}\left[\frac{K_1(\xi r_{tube})I_1\left(\xi r_{fin}\right) - K_1\left(\xi r_{fin}\right)I_1(\xi r_{tube})}{K_1\left(\xi r_{fin}\right)I_0(\xi r_{tube}) + K_0(\xi r_{tube})I_1\left(\xi r_{fin}\right)}\right] \tag{2.113}$$

where, r_{tube} and r_{fin} are the external tube and the fin radius respectively and h_{fin} is the fin height calculated as follow:

$$h_{fin} = \sqrt{r_{fin}^2 - r_{tube}^2} \tag{2.114}$$

Several studies have been performed in order to simplify this circular fin efficiency formulation by avoiding the use of modified Bessel functions. Among all the approximations, the Schmidt approximation [49] is the most widely used one:

$$\eta_{fin} = \frac{tanh\left(\xi \cdot h_{fin}\right)}{\left(\xi \cdot h_{fin}\right)} \tag{2.115}$$

In the developed model, only continuous plate fins are considered because typically fin and tube heat exchangers are composed of this kind of extended surfaces. The fins are metal sheets pierced through by the tube bank. The tube lay-out could be in inline or in staggered configuration with a clear advantage for the staggered lay-out.

In order to express the fin efficiency of such continuous plate fins, the fin is divided in unit cells. Considering that all the tubes are at the same temperature, the adiabatic zones of the fins determine the unit cells, as presented in figure 2.17. The considered fin shape is rectangular for the inline configuration and hexagonal for the staggered lay-out. Perrotin & Clodic [50] compared the two most used methods to calculate the efficiency of these rectangular or hexagonal fins from the circular fin efficiency with adiabatic fin tip

condition: the sector method and the equivalent circular fin method: The sector method is a semi-analytical method where the plain fin surface is divided in several circular sectors generated from the tube axis and fitting the fin geometry profile. In the equivalent circular fin method the fin efficiency is calculated considering an equivalent circular fin radius. Perrotin & Clodic reported that the most accurate method results the sector method. Nevertheless, the equivalent circular fin method is simpler (it requires lower computational time) and is more widely used.

For the calculation of the equivalent circular radius, two approaches are possible. The first one, originally presented by Gardner [48], consists in considering a circular fin having the same surface area as the rectangular or hexagonal fin. The other method is the Schmidt method [51] in which correlations are developed in order to find an equivalent circular fin having the same fin efficiency as the rectangular fin (equation 2.115) or the hexagonal fin (equation 2.116):

$$r_{fin,eq} = 1{,}27\frac{P_t}{2}\sqrt{\frac{\sqrt{{P_l}^2 + \left(\frac{P_t}{2}\right)^2}}{\frac{P_t}{2}} - 0{,}3} \qquad \text{for hexagonal fin sector} \qquad (2.116)$$

$$r_{fin,eq} = 1{,}28\frac{P_t}{2}\sqrt{\frac{P_l}{P_t} - 0{,}2} \qquad \text{for rectangular fin sector} \qquad (2.117)$$

Once the equivalent circular fin radius is calculated the respective equivalent fin height $h_{fin,eq}$ (equation 2.113) can be used to evaluate the fin efficiency η_{fin}. Perrotin & Clodic showed that the circular fin of the same area and the Schmidt circular fin methods are generally comparable but advantage is given to Schmidt method which significantly more accurate for hexagonal fin profiles.

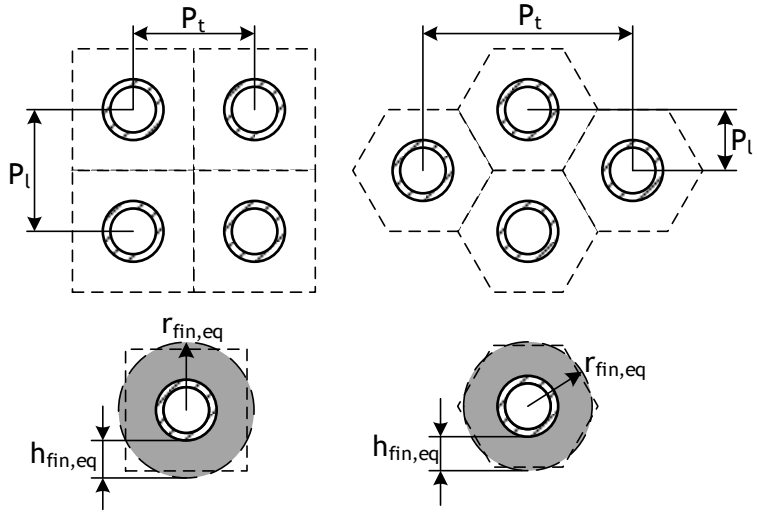

Figure 2.19 Inline a staggered configuration and fin adiabatic boundaries

Since the fin performance under wet conditions may be very different from the dry conditions, sufficient attention is needed to the wet fin performance analysis. The fin performance is dramatically influenced by the combined heat and mass transfer associated with the cooling and dehumidification of air. The condensation of moist air over the fin surfaces attributes to the decrease of fin efficiency. During cooling and dehumidifying of

moist air by a cold extended surface, a two phase flow situation exists. Furthermore, when the moisture in air condenses on the cooling surface, it results in a simultaneous heat and mass transfer. Hence, the approach for dry finned surface would be erroneous. The requirement of accurate calculation methods for the wet fin efficiency mainly exists in two fields concerning dehumidification coil study: one is in cooling coil simulation where the heat exchangers are commonly simulated based on arbitrarily small control volumes; the other is in reduction methods for coil test, where experimental data are deduced to the heat transfer coefficient to the primary surface based on the fin efficiency.

In practice, the fin surfaces of a dehumidifying heat exchanger may be fully dry, fully wet or partially wet depending on the difference between the adjoining air dew-point temperature and the surface temperature. If the fin-base temperature is higher than the air dew-point, there is only sensible heat transfer and is usually termed fully dry condition. However, if the fin tip temperature is lower than the dew point temperature of the moist air, sensible and latent heat transfer occur at the same time over the entire fin surfaces. This condition is identified as fully wet condition. Occasionally, a partially wet condition is seen: part of the fin tip temperature is higher than the dew point temperature whereas the rest of the fin temperature is below the dew point.

Most experimental investigations of dehumidifying heat exchangers reported in literature have been limited to fully wet operating condition in order to avoid difficulties associated with a analyzing partially wet heat exchangers [52]. The number of papers addressing heat transfer performance of heat exchangers under partially wet condition is limited. Recently, Xia & Jacobi [53] formulated a logarithmic enthalpy difference methods for fully dry, fully wet, partially and frosted surfaces. Pirumpugd et al. [55] combined a partially wet fin efficiency with a numerical integration method that adds the performance of individual fin segments. Their data reduction method has the unique advantage in analyzing complex coolant circuitry under partially wet condition. However, implementing these methods may require extensive computation and it can be complex [56]. For this reasons, in this work the partially wet fin condition has be neglected.

In literature several studies has been devoted to analyzing fin efficiency with condensation from moist air. In the fundamental work of McQuiston [14] can be found the system of equations in dimensionless form that describe moist-air heat transfer on rectangular fins:

$$\frac{\partial^2 T^*_{fin}}{\partial\left(\frac{y}{l_{fin}}\right)^2}+\frac{\partial^2 T^*_{fin}}{\partial\left(\frac{x}{l_{fin}}\right)^2}+(\xi^2\cdot x)\left(T^*_a-T^*_{fin}\right)\left(1+\frac{i_L}{c_{p,a}}\frac{x_a-x_{sat}\left(T_{fin}\right)}{T_a-T_{fin}}\right)=0 \tag{2.118}$$

$$\frac{\partial^2 T^*_a}{\partial\left(\frac{x}{l_{fin}}\right)^2}-NTU_{fin}(T^*_a-T^*)=0 \tag{2.119}$$

$$\frac{\partial^2 x^*_a}{\partial\left(\frac{x}{l_{fin}}\right)^2}-NTU_{fin}(x^*_a-x_{sat}{}^*)=0 \tag{2.120}$$

under the boundary conditions:

$$\left.\frac{\partial^2 T^*_{fin}}{\partial y}\right|_{y=l_{fin}}=0\quad;\quad\left.\frac{\partial^2 T^*_{fin}}{\partial x}\right|_{x=0}=0\quad;\quad\left.\frac{\partial^2 T^*_{fin}}{\partial x}\right|_{x=l_{fin}}=0 \tag{2.121, 2.122, 2.123}$$

$$x^*_a|_{x=0}=1\quad;\quad T^*_a|_{x=0}=0\quad;\quad T^*|_{x=0}=0 \tag{2.124, 2.125, 2.126}$$

where T_a^* and T_{fin}^* are respectively the dimensionless air and fin temperature; x_a^* and $x_{sat}{}^*$ are the dimensionless absolute humidity of the adjoining air and of the saturated air at the fin temperature; ξ is the fin parameter and NTU_{fin} is the thermal number of transport unit associated to the fin. These dimensionless value are defined as follow:

$$T_a^* = \frac{T_a - T_{fin,base}}{T_{a,in} - T_{fin,base}} \quad ; \quad T^* = \frac{T_{fin} - T_{fin,base}}{T_{a,in} - T_{fin,base}} \tag{2.127, 2.128}$$

$$x_a^* = \frac{x_a - x_{sat}(T_{fin,base})}{x_{a,in} - x_{sat}(T_{fin,base})} \quad ; \quad x_{sat}{}^* = \frac{x_{sat}(T_{fin}) - x_{sat}(T_{fin,base})}{x_{a,in} - x_{sat}(T_{fin,base})} \tag{2.129, 2.130}$$

$$\xi = \sqrt{\frac{h_o\, P_{cs,fin}}{k_{fin}\, A_{cs,fin}}} \tag{2.131}$$

$$NTU_{fin} = \frac{h_o\, x}{G_a\, s_{fin} c_{p,a}} \tag{2.132}$$

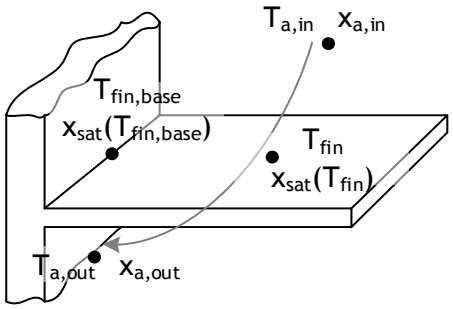

Figure 2.20 Rectangular fin with cooling and dehumidifying of moist air (simile a fig 11.7 in Srinivasan)

If the variation of the environmental conditions over in the x-direction are neglected (i.e. uniform environmental conditions over the fin length), the presented system of equation can be reduced to a one-dimensional analysis: equations 2.128 and 2.129 can be ignored.

To determine the wet fin efficiency, it is necessary to model the combined heat and mass transfer on the cooling surface in detail. Two methods are proposed to model the combined heat and mass transfer. One is the single-potential method that considers the enthalpy difference between the owing air stream and the saturated air at water surface temperature in the heat transfer calculation. The other is the dual potential method which considers the sensible heat transfer due to temperature difference of moist air and cooling surface and the latent heat transfer due to the absolute humidity difference between the adjoining air stream and the saturated air independently.

In the 1970 Threlkeld [11] proposed a solution of the resultant one-dimensional system of equations ignoring variations in the downstream direction. By assuming a uniform condensate film thickness t_w over the entire fin and by defining fictitious air enthalpy at different surface temperatures, Threlkeld has shown that the solution for dry fin efficiency also applies for the wet fin efficiency:

$$\eta_{fin,wet} = f(\xi_{wet}, l_{fin}, fins\ geometry) \tag{2.133}$$

and

$$\eta_{s,wet} = 1 - \frac{A_{fins}}{A_{tot}}(1 - \eta_{fin,wet}) \tag{2.134}$$

This conclusion is valid only if the heat transfer coefficient for the dry fin is replaced by an effective heat transfer coefficient in which the water thermal resistance is taken into account:

$$h_{eff,o} = \frac{1}{\left(\frac{c_{p,a}}{c_{sat}(T) h_o}\right) + \frac{t_{cond}}{k_w}} \tag{2.135}$$

where $c_{sat}(T)$ is the slope of the enthalpy-temperature curve for saturated air, t_{cond} is the condensate water thickness and k_{cond} is the thermal conductivity of the water film. Under Threlkeld assumption, the parameter ξ_{wet} for a longitudinal wetted fin of thickness t_{fin}, perimenter $P_{cs,fin}$ and section area $A_{cs,fin}$ introduced in chapter 6 becomes:

$$\xi_{wet} = \sqrt{\frac{h_{eff,o}\, P_{cs,fin}}{k_{fin}\, A_{cs,fin}}} = \sqrt{\frac{h_{eff,o}}{k_{fin}\left(t_{fin}/2\right)}} \tag{2.136}$$

Hence, it can be observed that the wetted fins analysis diverges from the dry fin analysis for the expression of the fin parameters ξ_{wet}.

In 1975, McQuiston [14] improved his previous works by studying the wet surfaces efficiency of a straight longitudinal fin. He assumed that the difference between the enthalpy of air adjacent to the fin and that of saturated air at the fin surface temperature is the potential for combined heat and mass transfer. In his work, McQuiston doesn't take into account of the resistance effect of the condensate film thickness t_{cond}. By approximating the saturation curve on the psychrometric chart by a straight line over a small range of temperature, the slope of the saturation $a_{sat}(T)$ line between two temperatures may be expressed as:

$$a_{sat}(T) = \frac{x_{sat}(T_1) - x_{sat}(T_2)}{T_1 - T_2} \tag{2.137}$$

Hence, the parameter ξ results

$$\xi = \sqrt{\frac{h_o\, P_{cs,fin}}{k_{fin}\, A_{cs,fin}}\left(1 + \frac{a_{sat}(T)\cdot i_L}{c_{p,a}}\right)} = \sqrt{\frac{h_o}{k_{fin}\left(t_{fin}/2\right)}\left(1 + \frac{a_{sat}(T)\cdot i_L}{c_{p,a}}\right)} \tag{2.138}$$

Again, equation 2.138 can be reduced in its conventional form by introducing the effective convective heat transfer rate $h_{o,eff}$ that under McQuiston's assumptions becomes:

$$h_{eff,o} = h_o\left(1 + \frac{a_{sat}(T)\cdot i_L}{c_{p,a}}\right) \tag{2.139}$$

It can be noted that for a dry the slope of saturation a_{sat} is null and the effective convective heat transfer rate $h_{o,eff}$ coincides with the usual convective heat transfer rate h_o.

The simplifying assumption of McQuiston seems to be valid only when the driving potential difference for mass transfer is large such that the small variation in the absolute humidity associated with varying temperature can be neglected.

The ARI Standard 401-81 [57] applied an earlier studied of Ware & Hacka [58]. They adopted a similar approach to that of Threlkeld, however they didn't account for the presence of the water film (therefore it's thermal resistance) and the water film temperature is replaced by the one of the surface. They recommended the following expression for the heat transfer coefficient for wet conditions:

$$h_{eff,o} = \left(\frac{h_o}{c_{p,a}}\right) c_{sat}(T) \tag{2.140}$$

where $c_{sat}(T)$ is defined as follow:

$$c_{sat}(T) = \frac{i_{sat,a}(T_1) - i_{sat,a}(T_2)}{T_1 - T_2} \tag{2.141}$$

Coney et al. [30] proposed a one-dimensional conjugate model that allows the coupling between the fin temperature and the condensate film, assuming a constant convective heat transfer coefficient along the fin. In their formulation, the value of the saturation absolute humidity is related to the fin temperature by a second-degree polynomial. They computed the temperature distribution along the fin height and the fin efficiency as a function of the relative humidity of the inlet air. The paper of Coney et al. also gives the results for the condensate thickness t_{cond}, however the study concluded that the effect of film thermal resistance can be neglected without introducing significant error for normal conditions encountered in practice. Their theoretical predictions has been confirmed by experimental study [31].

In 1991, Chen [59] performed a rigorous two-dimensional analysis of fin efficiency with combined heat and mass transfer and solved the system of equation numerically. A second-degree polynomial relationship between temperature and humidity ratio has been used. Chen's analysis considered that the air path line on the psychrometric chart along the fin base is not the same as that along the fin tip, while a simple air path line was assumed in the development of conventional one-dimensional fin model.

Srinivasan et al. [60] in the 1997 presented a critical assessment on the various method available for calculating fin efficiency in practical fin configurations with condensation, moist air cooling and boiling on extended surfaces. This work reported that the fin efficiency equation (of a single phase flow) with constant heat transfer for two flow situations may affect by serious error. They compared the one-dimensional fin efficiency with various values of air relative humidity predicted by McQuiston's model and ARI Standard 401-81 with Chen's model results. The value predicted by Chen's model vary significantly from the predictions of McQuiston, with more pronounced deviation at low values of relative humidity. This is majorly attributed to the different treatment of the dimensionless condensation factor introduced by Coney: McQuiston assumed a constant value whereas Chen based his study on a more accurate second-degree polynomial. The values given by the ARI Standard 401-81 model results to be in good agreement with the results of Chen.

As pointed by the previous literature review, the ARI Standard 401-81 based on the model of Ware & Hacka provides a simple and valid approach for predicting fin efficiency in moist air cooling by a cold extended surface. Hence, the fin efficiency η_{fin} is calculated by replacing the dry convective heat transfer coefficient h_o with the effective heat transfer coefficient $h_{eff,o}$ calculated with the conventional expression form dry fin efficiency given in literature as suggest by Ware & Hacka [58].

Hence, the fin parameter ξ under condensing and frosting condition results:

$$\xi = \sqrt{\frac{h_{eff,o}\, P_{cs,fin}}{k_{fin}\, A_{cs,fin}}} = \sqrt{\frac{h_{eff,o}}{k_{fin}\left(t_{fin}/2\right)}} \tag{2.142}$$

where the effective heat transfer coefficient $h_{eff,o}$ is calculated assuming a unitary Lewis number Le and assuming the effective saturation specific heat c_{sat} as slope of the

enthalpy-temperature curve for saturated air as suggested by Braun et al. [15] (average slope between the inlet and the water conditions, see equation 2.49):

$$h_{eff,o} = \left(\frac{h_o}{c_{p,a}}\right) c_{sat} \tag{2.143}$$

The approximation of a unitary Lewis number Le relies heavily on the mass transfer rate. It's usually true for dilute mixture like water vapour in air near the atmospheric pressure (temperature well below the corresponding boiling point). This implies that changes in the thermal and mass concentration distributions progress at approximately the same rates in mixture that undergo simultaneous heat and mass transfer diffusion process. In 2008, Wang [54] published a detailed analysis on heat and mass analogy of fin-and-tube heat exchanger. A total number of 36 fin-and-tube heat exchangers having plain fin geometry were tested in a controlled environment. It is found that the ratio of $h/h_m c_{p,a}$ is insensitive to change of fin spacing at low Reynolds number Re and it is not constant: a slight drop of the ratio of $h/h_m c_{p,a}$ has been see with the decrease of fin spacing and with the rise of the Reynolds number Re. This is associated with the more pronounced influence during condensate removal. Moreover, during the dehumidifying process, the temperature gradient is directly responsible for establishing the concentration gradient, suggesting the heat transfer and mass transfer are not independent as suggested by the Chilton-Colburn analogies. The reported variations of this ratio were limited in the range of 0,6 – 1,1. Experimental data of Hong & Webb [44] confirms that this value varies between 0,7 a 1,1. Also Pirumpugd et al. [55] reported that the values of the ratio $h/h_m c_{p,a}$ are generally between 0,6 and 1,2. The aforementioned studies all showed the applicability of the unitary Lewis number approximation.

The previous fins treatments is valid only if fouling is negligible. If fouling is significant, the convective coefficient h in the definition of the fin efficiency η_{fin} should be replaced by a partial overall heat coefficient $\overline{U}_p$. According to Kröger [12], fouling on the finned surface of an air-to-water heat exchanger affects the exchanger performance on the air side, resulting in a net reduction of the heat transfer rate. Although the effects on the overall heat transfer coefficient are small, the reductions on the airflow rate and on the mean temperature difference may reduce performance significantly. This effects can be treated by introducing the fouling factor R_f, in term of thermal resistance. (see [28] and [29]). In general its value depends on the operating temperatures, fluid velocity and length of service of the heat exchanger. The partial overall heat coefficient $\overline{U}_p$ includes the convective coefficient h and the fouling factor R_f between one fluid and its adjoining surface only. In general, it can be express in the form [1]:

$$\overline{U}_p = \frac{h_o}{(1 + h_o)} R_{f,o} \tag{2.144}$$

Fouling on external surfaces seems to be a transient phenomenon, that strongly depends on the surrounding condition (season, whether, location). Hence, some uncertainty exists concerning effect of external fouling on the performance of heat exchanger. This uncertainty is due to the extremely wide range of the diverse nature of the material that can cause fouling and to the number of flow arrangements adopted in practical systems. Even if many experiments were conducted, the results depends strongly on the exact type of heat exchanger and on the type and magnitude of the fouling layer: common trends were recognized but no practical relationship are available to predict the external fouling factors $R_{f,o}$.

As mentioned, the fin parameter ξ can be interpreted as ratio between conduction and convection thermal resistances. When a frost layer is present on the external surface of the fin, its additional insulating effect must be taken into account for the calculation of ξ.

An exact solution for a two-dimensional frost layer on a one-dimensional fin has not appeared in the open literature, nor has the applicability of such an approximation been explored for cases such as the one of interest. For most heat exchangers operating under frosting conditions, the fin is thinner than the frost, and both the fin and frost thicknesses are much smaller than the fin length. Furthermore, the frost thermal conductivity is much smaller than the fin conductivity (less than 1% for an aluminium fin). Thus, it is expected that in some cases it will be appropriate to simplify the problem to a one-dimensional frost layer on a one-dimensional fin; moreover, such an approach is anticipated to yield simpler expressions for temperature and fin efficiency than the case of a two-dimensional layer on a two-dimensional substrate. In comparison to prior fully two-dimensional solutions, this kind of solution has the advantage of involving relatively simple calculation.

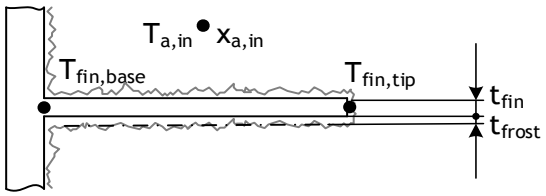

Figure 2.21 Rectangular fin with additional frost layer

In their study, [56] Dopazo et al. suggested that the frosted fin can be treat as a fin characterized by one dimensional conduction through two consecutive layer. Thus, considering that a frost layer characterized by a constant thickness t_{frost} and a constant thermal conductivity k_{frost} along a rectangular fin of thickness t_{fin} and thermal conductivity k_{fin}, the fin parameter ξ results:

$$\xi = \sqrt{\frac{h_o}{\left(k_{fin}\left(t_{fin}/2\right) + k_{frost}\, t_{frost}\right)}} \tag{2.145}$$

If the frost surfaces temperature is under the adjoining air dew point, heat and mass transfer simultaneously occur on the surfaces. Under this condition, the fin parameter ξ becomes:

$$\xi_{wet} = \sqrt{\frac{h_{o,eff}}{\left(k_{fin}\left(t_{fin}/2\right) + k_{frost}\, t_{frost}\right)}} \tag{2.146}$$

The assumption of a unitary Lewis Le number is also adopted to evaluate the effective heat transfer coefficient $h_{eff,o}$

Kim et al. [61] in their study, observed that due to fin and heat conduction, frost thickness decreases exponentially toward the fin tip, while considerable frost growth occurs near the fin base. Earlier Tso et al. [62] reported the same frost uneven frost growth on fin an tube. Furthermore they measured that tube row where the coolant inlet locates, which has lower wall temperature, has more frost accumulation and growth. Experiments conducted by Getu & Bansal [63] shows a different frost growth tendency. They reported that the frost thickness on the fin can be either greater than or equal to or lower than the thickness

on the tube depending on the fin position for frost-fin and frost-tube interface temperature. They explained that the different surfaces geometry (flat and round), the position of the fins and tubes and the flow pattern on the entire heat transfer surface are of the coil were much more influential than the difference between frost-fin and frost-tube interface temperature. Cui et al. [64] in their experiments observed that frost tends to grow on the windward sides of tubes compared with the leeward and the accumulation neat the frontward tubes is more than in the back tubes.

Hence, is to emphasize that an average frost-coil interface temperature was used to evaluate frost property for each row for the sake of simplicity and for reducing the fin and tube thickness difference. Hence, it has been assumed a uniform average frost thickness for tubes and fins, irrespective of specific position on the coil row.

2.5 Latent and sensible heat transfer of a dehumidifying moist air

When the external surface temperatures T_s are higher than the adjoining air dew point temperature $T_{a,dp}$, there is only sensible heat transfer occurring on the external air side of the heat exchanger. In this condition the previous presented $LMTD$ and the $\varepsilon - NTU$ methods can be directly applied to predict the heat exchanger performance.

In practical applications of air-to-water finned tubes heat exchangers, air dehumidification in often involved. This condition is reached when the surface temperatures T_s are under the adjoing air dew point temperature $T_{a,dp}$. Under dehumidifying conditions, latent and sensible heat transfer occur.

A real heat exchanger is not able to cool all the entering air to saturation and then dehumidifying it. Some of the air flowing through the heat exchanger core impinges on the water tubes or the fins and is cooled to an effective surface temperature, usually called apparatus dew point (ADP) temperature T_{ADP}. The rest of the air passes through unchanged. The ADP temperature T_{ADP} is the temperature at which all air will be cooled to if heat exchanger were 100 % effective. The apparatus dew point must be located on the saturation curve and on the same line where the entering and leaving air psychrometric coordinates can be found, refer to the psychrometric chart below:

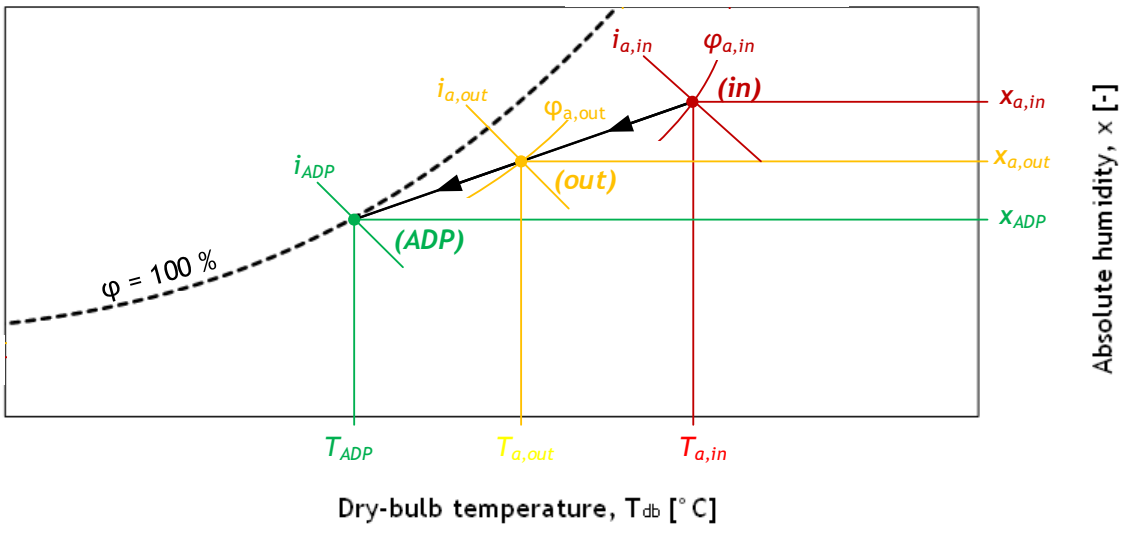

Figure 2.22 Psychrometric chart with ADP and bypass factor

In the model, for each row, the the ADP temperature T_{ADP} is identified by the interface temperature T_{int} between air stream and external surfaces (frost or row wall). This temperature T_{int} is calcaulated as area-weighted average value between temperature of the tube T_{tube} and of the fin the half of its equivalent height T_{fin} :

$$T_{int} = \frac{T_{tube}(A_o - A_{fins}) + T_{fin} \cdot A_{fins}}{A_o} \tag{2.147}$$

where T_{fin} is calculated by applying the same principles used to calculated the fin efficiency η_{fin}:

$$T_{fin} = (T_{tube} - T_{a,in}) \frac{cosh\left(\xi \cdot {}^{h_{fin,eq}}/_{2}\right)}{cosh(\xi \cdot h_{fin,eq})} + T_{a,in} \tag{2.148}$$

The row-tube temperature T_{tube} is simply estimated as mean temperature of the tube on the row:

$$T_{tube} = T_{av} + \frac{\dot{Q}_w}{(UA)_i} \tag{2.149}$$

where the value of $(UA)_i$ depends on the presence of frost as seen in paragraph 2.3 and row heat transfer rate $\dot{Q}_w$ and average water temperature T_{av}, results

$$\dot{Q}_w = (T_{w2} - T_{w1})\, \dot{m}_w c_{p,w} \tag{2.150}$$

$$T_{w,av} = \frac{T_{w2} + T_{w1}}{2} \tag{2.151}$$

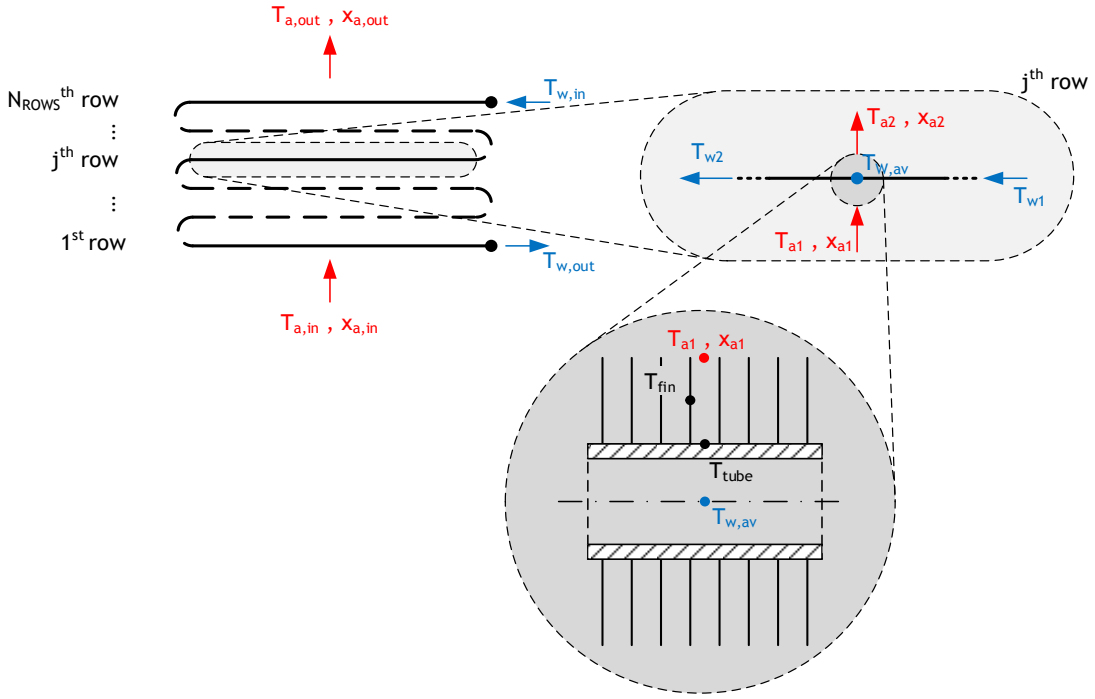

Figure 2.23 Global- and row-local temperature for a reference water circuits

The bypass factor BF is commonly used to express the cooling coils efficiency. It describes the percentage of the air that does not come into contact with the cooling coil and is not cooled to the ADP. It express how close the leaving air conditions are to the ADP. The

bypass factor BF is usually a function of the airflow, the number of rows, the fin spacing and many other construction attributes of the heat exchanger. The bypass factor can be found through the use of the enthalpy, dry bulb temperature or absolute humidity as follow reported:

$$BF = \frac{i_{a,in} - i_{a,out}}{i_{a,in} - i_{a,sat}(T_{ADP})} = \frac{T_{a,in} - T_{a,out}}{T_{a,in} - T_{ADP}} = \frac{x_{a,in} - x_{a,out}}{x_{a,in} - x_{a,sat}(T_{ADP})} \quad (2.152)$$

By applying Braun's ε-NTU enthalpy-based method [13], the delivered air heat transfer $\dot{Q}_a$ and the leaving air enthalpy $i_{a,out}$ can be calculated as:

$$i_{a,out} = i_{a,in} - \frac{\dot{Q}_a}{\dot{m}_a c_{p,a}} \quad (2.153)$$

The bypass factor BF can be immediately evaluated by using equation 2.152 . Then the outlet air dry-bulb temperature $T_{a,out}$ and the absolute humidity $x_{a,out}$ are respectively accounted as follows:

$$T_{a,out} = T_{ADP} \cdot BF - (1 - BF) \cdot T_{a,in} \quad (2.154)$$

$$x_{a,out} = x_{a,sat}(T_{ADP}) \cdot BF - (1 - BF) \cdot x_{a,in} \quad (2.155)$$

Once the dehumidifying and cooling rates are known, it is possible to evaluate the sensible and the latent air heat transfer rates.

The sensible air heat transfer rate $\dot{Q}_{a,S}$ is calculated by multiplying the dry-bulb temperature difference for the thermal air capacity:

$$\dot{Q}_{a,S} = (\dot{m}_a c_{p,a}) \cdot (T_{a,in} - T_{a,out}) \quad (2.156)$$

To evaluate the latent heat transfer rate is necessary to estimate the water specific latent heat of condensation $i_{L,cond}$. This parameter is usually dependent on the condensing water T_w temperature only. In the model, the correlation reported in the book of Rogers & Yau [65] has been adopted:

$$i_{L,cond} = (2500{,}8 - 2.36 \cdot T_w + 0.0016 \cdot {T_w}^2 + 0.00006 \cdot {T_w}^3) \quad \left[\frac{kJ}{kg}\right] \quad (2.157)$$

This correlation is valid for temperature from -40°C to 40°C .

Then, the latent heat transfer rate $\dot{Q}_{a,L}$ is calculated as follows:

$$\dot{Q}_{a,L} = \dot{m}_a \cdot i_{L,cond} \cdot (x_{a,in} - x_{a,out}) \quad (2.158)$$

To takes into account for the latent air heat transfer rate $\dot{Q}_{a,L}$ heat transfer, the water specific latent heat of condensation $i_{L,cond}$ must be substitute in equation 2.157 with the respective values water for water sublimation $i_{L,sub}$. This value can be evaluated through the correlation reported by Rogers & Yau [65], whose is available in the temperature range between -40°C and 0°C :

$$i_{L,sub} = (2834{,}1 - 0.29 \cdot T_w + 0.004 \cdot {T_w}^2) \quad \left[\frac{kJ}{kg}\right] \quad (2.159)$$

and

$$\dot{Q}_{a,L} = \dot{m}_a \cdot i_{L,sub} \cdot (x_{a,in} - x_{a,out}) \quad (2.160)$$

It has to be mentioned that when the air stream is near the saturation condition, the predicted outlet air absolute humidity $x_{a,out}$ and temperature $T_{a,out}$ using the bypass factor BF can correspond to a point in the fog zone. Hence, to avoid erroneous calculation, those values are substitute with the values on the saturation line at the previously estimated outlet water enthalpy $i_{a,out}$. This condition is represented in the following psychrometric chart.

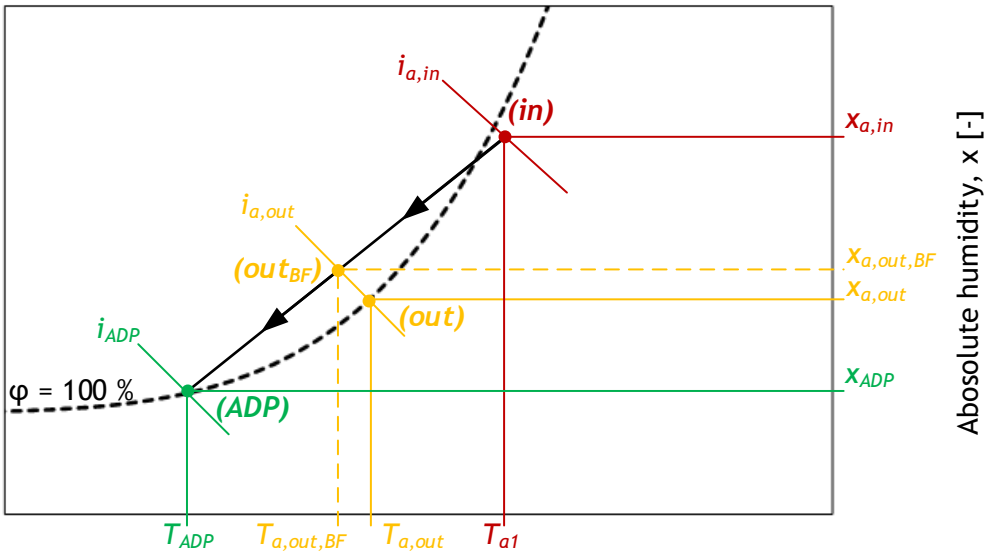

Figure 2.24 Erroneous prediction of the outlet air condition using the bypass factor

2.6 Frost formation and defrosting process

In spite of its importance, heat exchanger frosting research remained latent for many years. Over a period of more than 50 years, nearly 150 studies have been published on frost growth on heat exchanger surfaces. O'Neal & Tree [67], Padki et al. [68] and Da Silva et al. [69] summarized many of the papers published until the last decade. Considerably work have been done regarding experimental investigation of frost formation but they are still inconsistences and open fields of research. This come from a different number of assumptions, different experimental conditions and geometries. Many authors have analysed and mathematically described the frost formation process using different levels of mathematical and numerical assumption. Some authors adopted one- or two-dimensional modelling, modelling of boundary layer near air-frost interface, homogenous frost distribution, superheated principles.

Researches on frosting phenomena of heat exchanger are mainly classified in three field: frost properties such as thermal conductivity and density of frost, frost formation and growth, and heat exchanger performance under frosting condition. For the first groups using locally simplified geometry, such as flat plate or cylindrical surface, many experimental and numerical studies have been performed under various conditions. Some of studies investigated the frost growth numerically and validated the numerical models with experimental data. Other studies proposed empirical correlations for the frost properties after performing experiments for various frosting parameters. The studies of the

third group, investigate the effects of frosting behaviour and thermal performance of heat exchanger under various operating conditions. However, analytical studies for the thermal performance of heat exchanger dealt with frost formation too simplistically by either proposing models without robust validations or using correlations for heat transfer coefficient that were derived for a specific heat exchanger experimentally. Therefore, it is undesirable to apply their results to applications where a different shape of heat exchanger is considered.

More recently distributed time-dependent parameters approaches were adopted ([70],[71],[66]). This models can be reach a higher level of accuracy compared to the previous studies but they increase significantly the computation time. For this reason, it has been choose to avoid the use of this kind of model.

As pointed by Lenic [72], in the majority of the cases, the frost layer is considered as a porous structure containing iced mesh and air gaps. This can be assumed to be valid only for part of the whole frost formation process. In fact frosting is typically a transient phenomenon. The whole frost formation period is usually divided in two ([73],[74]) or three different ([75], [76], [77], [78]) periods. The most accredited qualitative theory of frost growing is the one developed in the 1977 by Hayashi et al. [75]. They conducted experiments on frost formation over a cold surface in different possible condition. It results that formation process is divided in crystal growth period, frost growth period and fully development period.

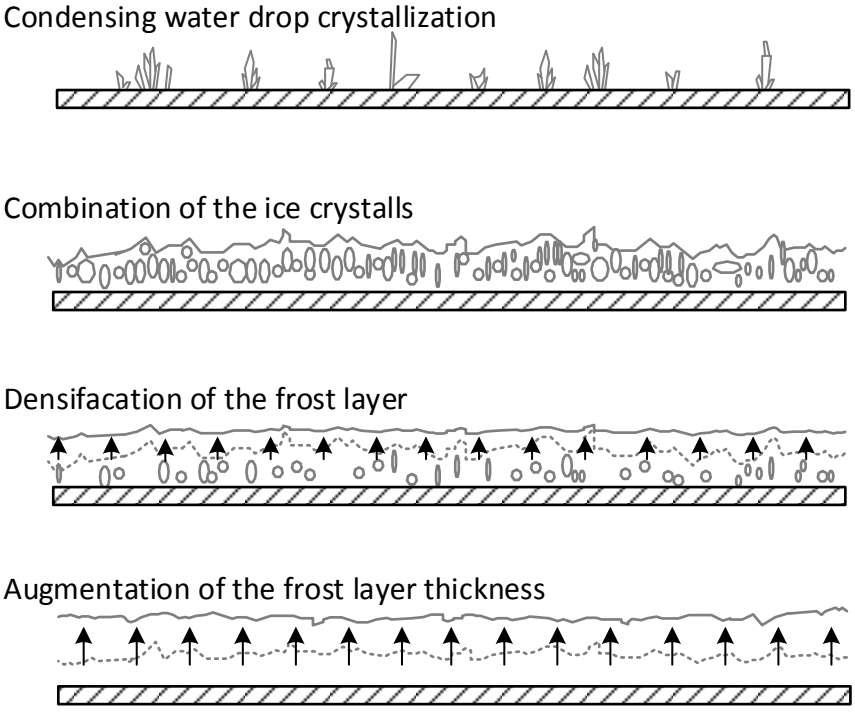

Figure 2.25 Schema of formation and growth of frost layer [72]

At the early stage, smaller water vapour drops in the moist air condensate or sublimate on the cold surface, acting as the nuclei of the future crystallization. They grow and connect together with their neighbours. The newly coalescent ice crystals grow on these nuclei and

spread in all directions simultaneously. This initial period has a dominant influence on the further growth process. In this period the frost thickness increases obviously and the frost layer surface becomes rugged visibly.

The second stage is characterized by densification of a porous layer. The small liquid droplets, the ice crystals and the air molecules fill the gaps among the ice branches or icicles. In this period, most of the mass transfer from the moist air to the frost layer contributes to density increase while the variation of the thickness is almost not notable as that in the first period.

As the frost grows, latent heat releasing causes an increase in the surface temperature. The fully developed period occurs when the frost surface temperature has become equal to the melting point. The frost deposited will partially melt and seep through the pores of the porous frost layer, eventually reaching the cold surfaces, where it freeze into ice. This thinning and densification due to melting and refreezing process is known as permeation. This cyclic process of condensing/sublimating and permeation occurs until a thermal equilibrium is reached. It lead to an additional densification of the frost layer and an augmentation of the frost thermal conductivity. During this stage, the frost shows homogenous and porous characteristics and the frost layer surface will become smooth gradually.

During the whole frost process, the mass transfer comprises two parts: one is from the water vapour to frost layer due to frost formation and growth occurring in the initial period and growth period, while the other is from the frost layer to liquid film or to water vapours resulting of the melting process taking place in the fully developed period.

In order to avoid the use of more accurate that will unacceptably higher computational time, in the present work a simple semi-empirical approach to frost formation and growth is used. In the developed model, the frost growth is assumed to be as a quasi-steady state phenomenon. Steady state conditions are assumed to exist for sufficiently small time intervals but the overall analysis will remain transient in nature. The formed frost layer is treated as porous layer and uniform properties obtained by averaging local frost properties. Frost distribution is homogenous (constant thickness t_{frost}) over the area that present a surface temperature below the inlet air dew-point and the frost point. The thermal conductivity k_{frost} is considered to vary only with frost density ρ_{frost}. The effects of the vapour diffusion into the frost layer is evaluated on the basis of Seker et al. [79] approach.

During a time-step dt under frosting conditions, the rate of deposition $d(m_{frost})$ is expressed as loss of humidity in the air as water vapour condenses on the cold coil surfaces:

$$d(m_{frost}) = \dot{m}_a \cdot (x_{a,in} - x_{a,out}) \cdot dt \tag{2.161}$$

The temperature T_{frost} at which the frost form is supposed to be the coil-air interface coincident with the apparatus dew-point (ADP) temperature T_{ADP} introduced in the previous paragraph.

The thermal conductivity of a frost k_{frost} can assume very different values between 0,024 W/(m K) and 2,4 W/(m K) (thermal conductivity of pure ice). It depends mainly on its density which can approximately vary from 20 kg/m^3 to 920 kg/m^3 (density of pure ice). The initial frost density ρ_{frost} of the deposited frost layer is evaluated by employing the

Hayashi's correlation [75] between frost density and the temperature of frost surface T_{frost} expressed in °C only:

$$\rho_{frost} = 650\, e^{(0{,}277\, T_{frost})} \tag{2.162}$$

Equation 2.162 is widely considered for frost growth modelling. It applicable between the frost temperature T_{frost} of 273,15 K (0°C) and -248,15 K (-25°C). This correlation is known to predict higher value when the frost surface rises to the frost-point. Another limitation of Hayashi's correlation is ascribed to its dependence on frost temperature only without regard to the temperature of the surface. As pointed by Bullard & Chandrasekharan [80], it also fails below 263,15 K (-10°C). Since the encountered values of the frost surface temperature T_{frost} rarely reaches values below 263,15 K (-10°C), the last limitation doesn't affect the results of this work. Thus, the correlation which is better suited to applications between 272,15 K (-1°C) and 264,15 K (-9°C), is being extended to the whole range of temperatures encountered. Furthermore, in literature there are no other correlations available in this range of temperature.

When the heat exchanger surface is unfrosted the thickness of the deposited frost $d(t_{frost})$ is calculated assuming that all the rate of deposition $d(m_{frost})$ in the time step will form a frost layer at the evaluated frost density ρ_{frost}:

$$t_{frost} = \frac{d(m_{frost})}{\rho_{frost} \cdot A_{frost}} \tag{2.163}$$

where A_{frost} represent the area of the surface under frosting condition

When the heat exchanger surface results already frosted, a reparation of the deposited water vapour $d(m_{frost})$ is necessary to take into account for the vapour diffusion into the frost layer. Part of deposited frost mass upon the heat exchanger surface increases the frost density while the rest increases the frost thickness:

$$m_{frost} = m_{frost,\rho} + m_{frost,t} \tag{2.164}$$

In this work to account for the densification effectt, the diffusion model originally developed by O'Neal & Tree [67] is adopted. The amount of water vapour increasing the density $m_{frost,\rho}$ can be related to the total deposited vapour m_{frost} as follow:

$$m_{frost,\rho} = m_{frost} \frac{(i_{a,in} - i_{a,out})}{D} \tag{2.165}$$

where D is an effective diffusion coefficient, that, following the interpretation of Seker et al. [79] can be evaluated as follows:

$$D = \frac{k_{frost}}{D_{v,a}} \left(\frac{1 + (\rho_{frost}/\rho_{ice})^{1/2}}{1 - (\rho_{frost}/\rho_{ice})} \right) \frac{R_g^2 \cdot T_{frost}^4}{p_{sat}(T_{frost})(i_{L,sub} \cdot T_{frost} - R_g T_{frost}^2)} + i_{L,sub} \tag{2.166}$$

where R_g is universal gas constant expressed in kJ/(kmol K), $p_{sat}(T_{frost})$ is the saturation air pressure at the frost temperature T_{frost}, ρ_{ice} is the pure ice density and, is the water vapour-air diffusion coefficient. This last parameter can be evaluated using the relationship suggested in ASHRAE Hanbooks and originally developed by Sherwood & Pigford [81]:

$$D_{v,a} = 0{,}926 \left(\frac{1}{p_a}\right) \left(\frac{T_a^{2.5}}{T_a - 245}\right) \cdot 10^{-3} \qquad \left[\frac{m^2}{s}\right] \tag{2.167}$$

where T_a and p_a are the air and pressure of air expressed in K and kPa respectively. This correlation is valid up to 1100 °C.

Assuming that the present frost layer is characterized by mass $m_{frost,0}$, thickness $t_{frost,0}$ and density $\rho_{frost,0}$, for the sequent time-step under frosting condition, the change of frost density and frost thickness can be determined as follow:

$$d(\rho_{frost}) = \frac{m_{frost,\rho}}{A_{frost} \cdot t_{frost,0}} \tag{2.168}$$

$$d(t_{frost}) = \frac{m_{frost,t}}{A_{frost} \cdot \rho_{frost,0}} \tag{2.169}$$

These values are added to the values of frost thickness and frost density of previous time step in order to obtain the values of the current time-step:

$$m_{frost} = m_{frost,0} + d(m_{frost}) \tag{2.170}$$

$$t_{frost} = t_{frost,0} + d(t_{frost}) \tag{2.171}$$

$$\rho_{frost} = \rho_{frost,0} + d(\rho_{frost}) \tag{2.172}$$

Once the frost density ρ_{frost} reach the level of pure ice (assumed to the conventional value of 920 kg/m^3) the depositing water vapour is assumed to increase the frost thickness without densification effect, $d(\rho_{frost})$ results null. In other words, the frost layer increase with a constant density.

The empirical relationship of Yonko & Sepsy's [82], which can be considered more close to the reality [66], is used in this work to expresses the effective thermal conductivity of frost k_{frost}. It is a function of the frost density ρ_{frost} only:

$$k_{frost} = \left(0.02422 + 7.214 \cdot 10^{-4} \cdot \rho_{frost} + 1.1797 \cdot 10^{-6} \cdot \rho_{frost}^2\right) \cdot 10^{-3} \tag{2.173}$$

The correlation is limited to ρ_{frost} below 576 kg/m^3. Because their correlation predicts the thermal conductivity of pure ice within 10 %, the previous equation is used for the entire range of frost densities encountered.

2.7 Fan performance evaluation

To provide a continuous air flow across the forced (or induced) draft heat exchanger, it is necessary to use a fan. Due to the lower density of air compared to of water, the electrical power consumption of the fan system can be much larger than the electrical power need to pump the water. Hence, modern heat exchangers adopt high efficiency, speed controlled, sickle-blade, axial flow fans to reduce [12] operation consumption (and operation cost) as well as noise.

The performance of fans are usually determined in standard test facilities. Each fan of given size, operating at a specified rotational speed is characterized by a performance curve. Even for a fixed size and fixed rotational speed, the power and pressure requirements vary over the variability range for different flow rates.

If the thermal conditions of a heat exchanger vary, in particular the required heat transfer rate, it is opportune to work with a variable rotational speed. Variable speed operation involves adjusting the fan rotation rate to meet the changed flow rate, due the different heat transfer request.

Since it is usually inconvenient to carry out fan test at each speed and density values, conversion rules are used to determine the fan performance at specified rotational speed and fan inlet air density. These conversion rules are known as fan laws or as affinity laws.

For geometrically similar fans, the performance data can be collapse onto a single dimensionless curve. Under these conditions, by applying the fan laws, it is possible to correlate change in flow rate, pressure and power when the speed, size or inlet density is changed. The volumetric flow rate $\dot{V}$ of a fan is directly proportional to the fan rotational speed ω.

The first fan law relates these two parameters:

$$\frac{\dot{V}_1}{\dot{V}_2} = \left(\frac{d_1}{d_2}\right)^3 \frac{\omega_1}{\omega_2} \tag{2.174}$$

The second fan law relates the fan total pressure, or fan static pressure p, to the fan rotational speed ω. The static pressure is proportional to the square of the rotational speed:

$$\frac{p_1}{p_2} = \left(\frac{d_1}{d_2}\right)^2 \left(\frac{\omega_1}{\omega_2}\right)^2 \left(\frac{\rho_1}{\rho_2}\right) \tag{2.175}$$

The last fan law relates the fan static pressure, and the impeller power, to the fan rotational speed in the form:

$$\frac{\dot{W}_1}{\dot{W}_2} = \left(\frac{d_1}{d_2}\right)^5 \left(\frac{\omega_1}{\omega_2}\right)^3 \left(\frac{\rho_1}{\rho_2}\right) \tag{2.176}$$

The tree main fan laws given above can be combined and rearranged to derivate other fan laws.

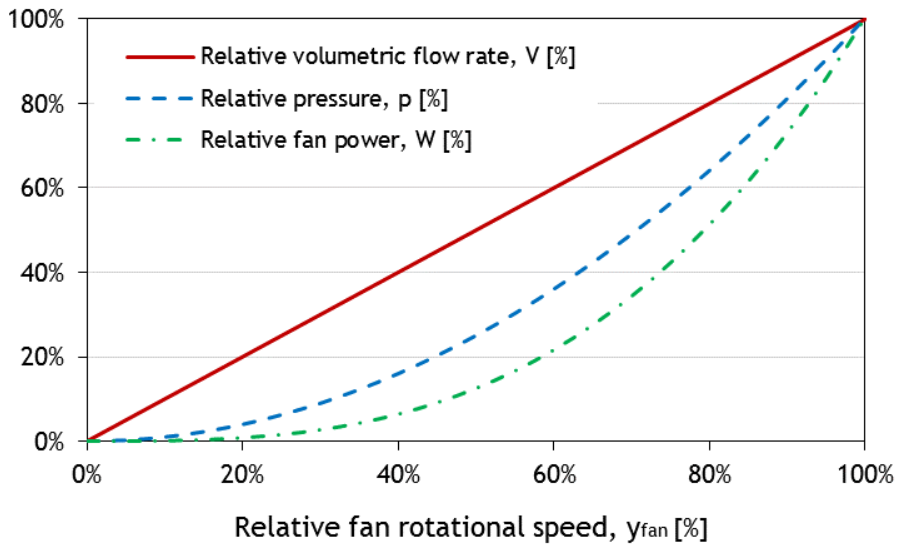

Figure 2.26 Fan law diagram for costant density and variable fan rotational speeds

Fan laws rely on the fact that the performance curves are homologous and the ratios are the same for relative points of rating on each curve.

Fan laws can't be applied if the pressure does not vary as the square of the flow rate and if the system has been physically altered or, for some reason, it operates on a different system requirements curve.

To evaluate the pressure drop across a bank of finned tubes, McKetta [85] reported simple empirical correlations. These correlations shows that the pressure drop may be express as a function of face velocity v_∞, number of tube rows N_{rows}, and of the concentration of fins per length of heat transfer surface a_{fin}:

$$\Delta p = f(a_{fin}, N_{rows}, v_\infty) \tag{2.177}$$

An alternative method to determine the pressure drop in a heat exchanger core is reported by Kays & London [4]. It provides equations to evaluate pressure drop given the core velocity and geometry. For a normal air flow to tube banks the suggested pressure equation is:

$$\frac{\Delta p}{p_{a,in}} = \frac{v_{a,max}^2}{2\, p_{a,in}\, \rho_{a,in}} \left((1+\sigma^2)\left(\frac{\rho_{a,in}}{\rho_{a,out}} - 1\right) + f \frac{A}{A_{ff}} \frac{\rho_{a,in}}{\rho_{a,av}} \right) \tag{2.178}$$

The value of the friction factor to use in the given equations can be found in tables and diagrams represented the best interpretations of test data [4].

In the model the air pressure drop has not be considered because the fan performance are evaluated using correlations that relate the induced volumetric flow rate $\dot{V}_{fan}$ and the electrical consumption $\dot{W}_{el,fan}$ of a single fan to the relative fan rotational speed y_{fan}:

$$y_{fan} = \frac{\omega}{\omega_{max}} \tag{2.179}$$

In the model the volumetric flow rate $\dot{V}_{fan}$ induced by a single fan at a given fan rotational speed ω is calculated as follow:

$$\dot{V}_{fan}(\omega) = \dot{V}_{fan}(\omega_{max}) \cdot \left(c_{v1,fan} \cdot y_{fan}^4 + c_{v2,fan} \cdot y_{fan}^3 + c_{v3,fan} \cdot y_{fan}^2 + c_{v4,fan} \cdot y_{fan}\right) \tag{2.180}$$

where $\dot{V}_{fan}(\omega_{max})$ is the volumetric flow rate at the maximal fan rotational speed ω_{max}.

The four coefficients $c_{v,fan}$ of equation 2.184 are taken from the best fitting curve of monitoring data developed by Bettoni & D'Antoni [27]:

Table 2.5 Dimensionless coefficients for the volumetric flow rate correlation [27] (equation 2.184)

Coefficient order	**Dimensionless coefficient**
j	$c_{vj,fan}$
1	-3,0121
2	7,2403
3	-6.4414
4	3.2129

In the next figure in reported the curve described by equation 2.185 is compared to the linear relationship between relative fan rotational speed and y_{fan} and volumetric flow rate $\dot{V}_{fan}$:

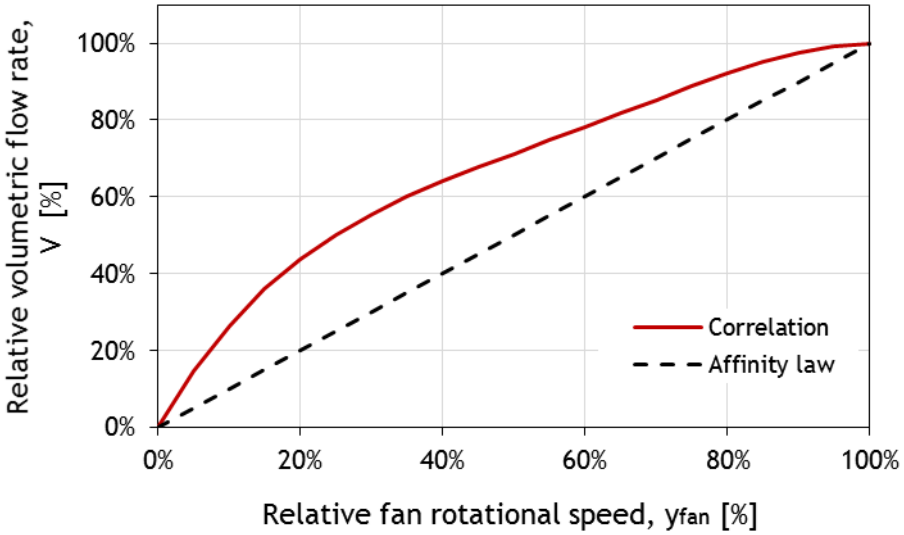

Figure 2.27 Predicted realative volumetric flow rate

The electrical consumption of a single fan $\dot{W}_{el,fan}$ is evaluated through a polynomial function of the relative rotational speed y_{fan}. The following equation described the best fitting curve of the available monitoring data collected by Bettoni & D'Antoni [27]:

$$\dot{W}_{el,fan}(\omega) = \dot{W}_{el,fan}(\omega_{max}) \cdot \left(c_{p1,fan} \cdot y_{fan}^4 + c_{p2,fan} \cdot y_{fan}^3 + c_{p3,fan} \cdot y_{fan}^2 + c_{p4,fan} \cdot y_{fan} + c_{p5,fan}\right) \quad (2.181)$$

where $\dot{W}_{el,fan}(\omega_{max})$ is the electrical power required by a single fan that is working at its maximal rotational speed ω_{max}. The five coefficients obtained from the analysis conducted on the monitoring data are reported below:

Table 2.6 Dimensionless coefficients for the correlation (equation 2.185)

Coefficient order j	**Dimensionless coefficient** $c_{pj,fan}$
1	-2.468795
2	4.862549
3	-1.503527
4	0.279465
5	0

If no monitoring data are available, according to the affinity laws, a cubic relationship between the relative fan rotational speed is used instead of equation 2.185. This cubic relationship is corrected by multiplying it for the ration between the inlet $\rho_{a,in}$ and a reference value $\rho_{a,ref}$ of the air density:

$$\dot{W}_{el,fan}(\omega) = \dot{W}_{el,fan}(\omega_{max}) \cdot y_{fan}^{3} \left(\frac{\rho_{a,in}}{\rho_{a,ref}} \right) \tag{2.182}$$

In figure 2.28, it can be noted that the predicted values are in good agreement with the monitoring data except for fan rotational speed near the maximum. To avoid predicting erroneous values at high relative fan rotational speed, the developed correlation has been upper limited at the electrical power consumption value $\dot{W}_{el,fan}(\omega_{max})$ monitored at the maximal fan rotational speed ω_{max}.

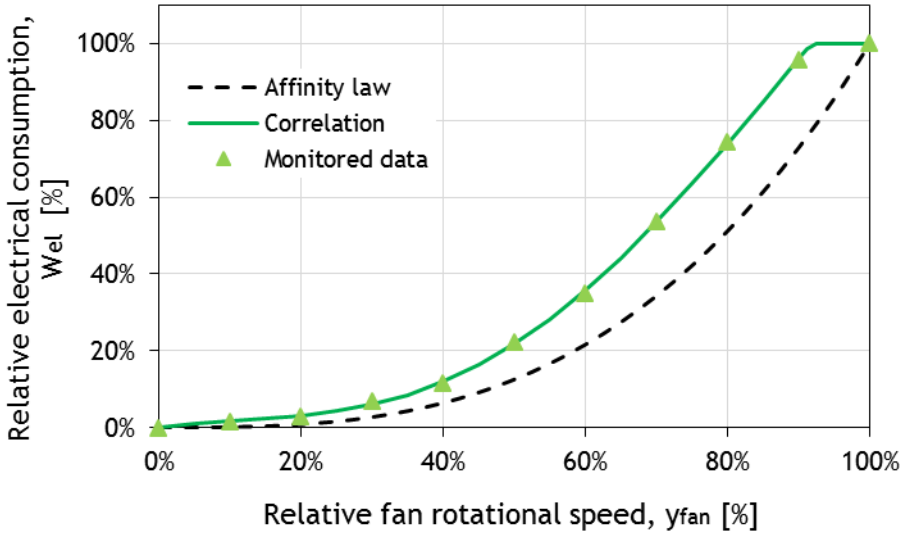

Figure 2.28 Monitored data, predicted values of the relative electrical power consumption

2.7.1 Fan working mode

In this work, the control strategy of the fan is based on four different fan working mode [27] depending on the specified set point and external control signal:

- Working mode 0: the fan will work at its maximal capacity only when the specified outlet water reference temperature results higher than the inlet water temperature. In fact this is the only condition where the water stream needs to be heated. Otherwise the fan won't work.
- Working mode 1: the fan rotational speed is varied in the allowed range until the specified outlet water reference temperature is reached or until the maximal or the minimal fan rotational speed is reached.
- Working mode 2: similarly to the working mode 1, the fan rotational speed is varied in the allowed range until the outlet water reference temperature is reached or until the maximal or the minimal fan rotational speed is reached. In this case the outlet water reference temperature is not directly specified as for working mode 0 and 1, but it is calculated based on a specified temperature difference from the inlet air temperature.

- Working mode 3: in this mode, no outlet water reference temperature is declared and the fan will work at a fixed rotational speed imposed by an external control signal.

3 Model development

Most experimental and analytical investigations on dehumidifying heat exchangers reported in literature have been limited to fully wet operations conditions. Park & Jacobi [36] reported that heat transfer correlations from studies of fully wet heat exchanger may be inadequate for partially wet heat exchanger and can produce underprediction of the actual heat transfer rate. In fact under partially wet condition the delivered heat transfer rate can be higher because the higher effective heat transfer potential (i.e. enthalpy difference) and sometimes by increased heat transfer coefficient.

Partially wet condition can occur when the surface temperature of a heat exchanger is not uniform. In particular, in dehumidifying heat exchanger the temperature of a single-phase liquid, such as water, increases continuously along the tube-side flow path. A correct approach to the problems, should involve area-partitioning method, where the heat exchanger is divided in three regions: fully dry, partially wet and fully wet. In fully dry part, both fin-tip and fin-base temperatures are over the dew-point temperature of the adjoining air stream and no dehumidification takes parts. For fully wet region these temperatures are below the dew-point and the air absolute humidity decreases. In partially wet portion, the tube temperature is below the dew-point, but the fin-tip temperature is higher. This approach can be directly applied only if the tube-side temperature along the flow path is known, otherwise it will involves a iterative procedure that gets more complex as more complex becomes the coolant circuitry as mentioned in chapter 2.

Applying the before described method will involve an increasing in the division of the heat exchanger area with the simulation-time. In fact, for time-steps under frosting condition the determined fully and partially wet region will present changes in their geometrical and air flow characteristics. These variations must be taken into account in the sequent time-step: at first the heat exchanger area has to be divided in the regions which present common geometrical characteristics and then, each of these regions must be sub-divided into its fully dry, fully wet and partially wet part. As the simulation-time increased, the number of regions and the computational time will increase as consequence.

Hence, to avoid significant underestimation of the heat transfer rate and at the same maintaining a contained computational time, the heat exchanger is analyzed row-by-row by a fully-wet fully-dry approach. The row will be treats under fully wet or fully dry condition depending if the calculated surface temperature is below or over the dew-point temperature of the adjoining air stream. Furthermore, no work has been found in literature about frosting under partially wet condition.

3.1 Geometry characterization

The developed model refers to an air-to-water heat exchanger arranged in a multirow-multipass overall counterflow configuration with unmixed crossflow at each row.

The heat exchanger coil is a gas forced blown bank of plain finned tubes, inside which the working fluid is flowing. The tubes axes are perpendicular to the gas stream and arranged in a staggered configuration divided in strings and rows.

To minimize the pressure drop in the tubes and enhance the heat transfer rate the working fluid is usually divided in several circuits. These circuits evolve in overall counterflow to the gas stream. The different combinations of tubes in the same or in the sequent rows characterize each circuit.

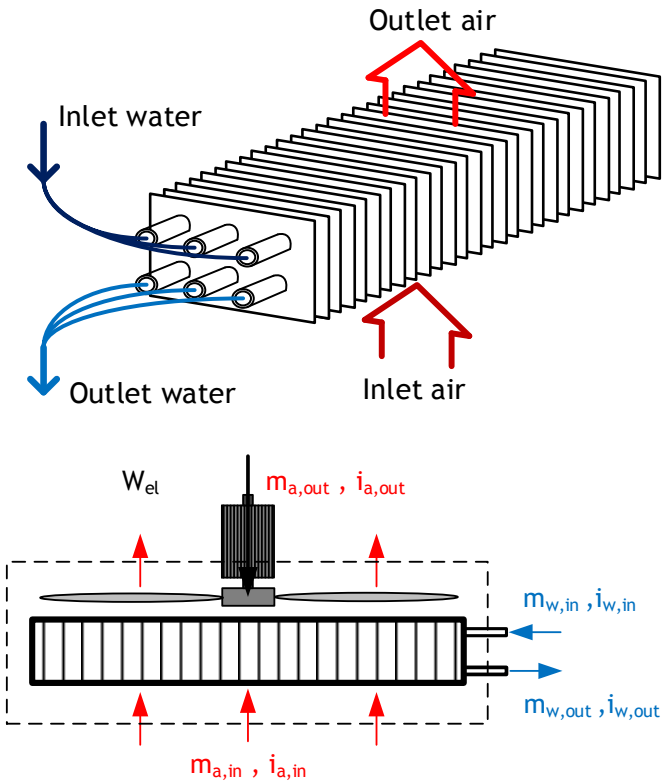

Figure 3.1 Bank of finned tubes and multirow (crossflow) overall counterflow arrangement

The original heat exchanger on which the model is based, is air-to-water hybrid cooler RCS 08 provided by SorTech AG. The aim of this choose is to get a model based on the actual standard commercial product for heat exchanger (To see the specific characteristic of SorTech AG RCS 08 see Appendix A). This model is designed to meet the special requirements of adsorption chiller. It features controlled rotational speed EC fans fresh and water spraying system which allows hybrid cooling in summer mode.

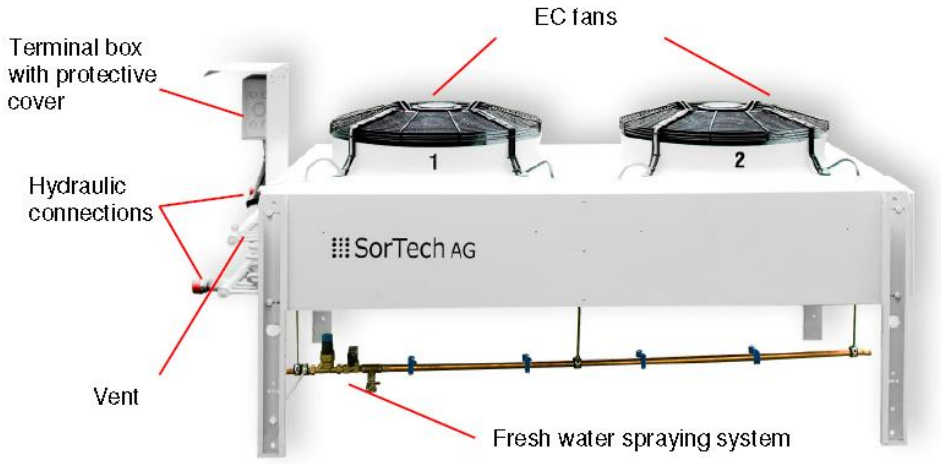

Figure 3.2 Sortech AG RCS 08

The total internal A_i and external heat transfer area A_o are respectively around 9 m^2 and 222 m^2.

Figure 3.3 Sortech AG RCS 08 – Front water circuits pattern

Figure 3.4 Sortech AG RCS 08 – Back water circuits pattern

To uniform the pressure drop in the coil, the water flow is divided in 12 circuits ($N_{circuits}$) across 6 rows (N_{rows}) and 21 strings ($N_{strings}$). Consequently, the number of tubes N_{tubes} is 126.

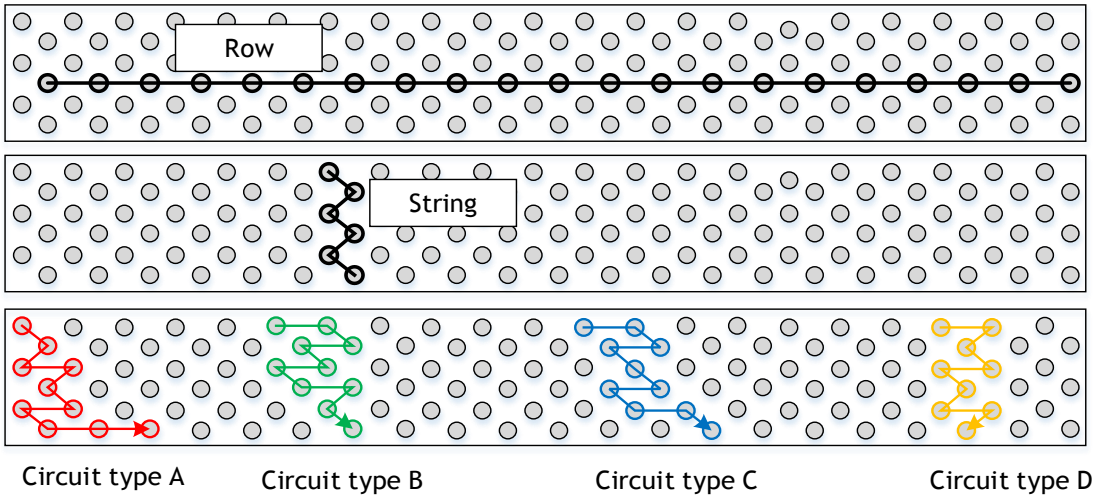

Figure 3.5 Strings, rows and circuits idenfication on Sortech AG RCS 08

The coil is composed by copper round tubes and epoxy plain fins. The longitudinal pitch P_l between tubes of sequent row is 25 mm, whereas the transversal pitch P_t between tubes on the same row is 50 mm. The internal tube diameter d_i is 12 mm and the external tube diameter d_o is 14mm. Fins with a thickness t_{fin} of 0.15 mm and 2.4 mm spacing s_{fin} are added to enhance the external heat transfer area.

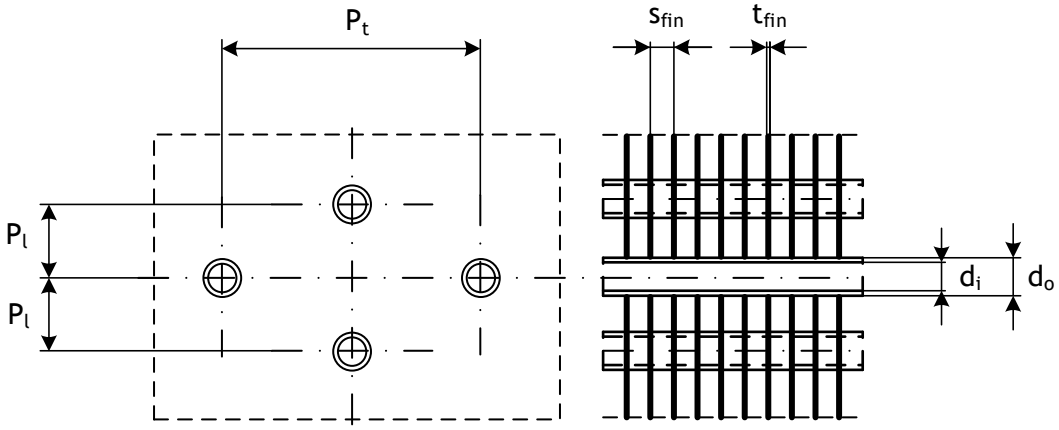

Figure 3.6 Particulars of Sortech AG RCS 08 tubes and fins geometries

The length of the fan casing l_{fan} (0.925 m) allows to calculate the length of the duct in the tube direction l_d. This length is equivalent to the length of a tube pass l_t (1.85 m) (tube length in a row):

$$l_d = l_t = l_{fan}\, N_{fans} \tag{3.1}$$

consequently, the total length of the tubes located on the same row $l_{tubes,row}$ (38.85 m) is:

$$l_{t,row} = l_d\, N_{strings} \tag{3.2}$$

The frontal area of the coil is simply calculated as:

$$A_{fr} = l_d \cdot w_d \tag{3.3}$$

where the duct width w_{duct} is equal to the fan casing width is around 1,95 m^2.

The total number of fins N_{fins} present on the coil can be calculated as follow:

$$N_{strings} = \frac{l_t}{s_{fin}} \tag{3.4}$$

To evaluate the minimum free flow area A_{ff} across the coil (1,31 m^2) , it is necessary to account for the obstruction due to the presence of tubes and fins. Hence, known the transversal pitch P_t, the external tube diameter d_o and the fin dimensions t_{fin}, s_{fin}, the minimum free flow area results:

$$A_{ff} = \Big(\big(s_{fin} - t_{fin}\big)(P_t - d_o)\Big) \cdot N_{strings} \cdot N_{fins} \tag{3.5}$$

The heat exchanger compactness σ is defined as the ratio between the minimum free flow A_{ff} and the frontal A_{fr} areas:

$$\sigma = \frac{A_{ff}}{A_{fr}} \tag{3.6}$$

The compactness σ of the SorTech AG RCS 08 results 0.674.

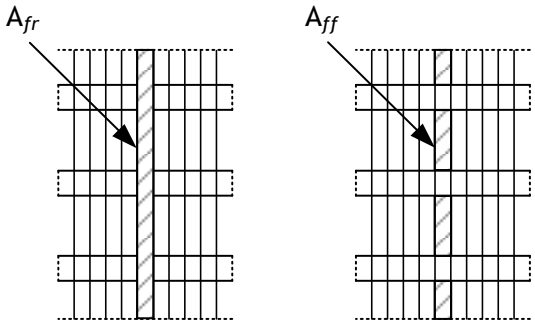

Figure 3.7 Frontal and minimum free flow area of a single air passage

The internal heat transfer area A_i is calculated accounting for the total number of tubes N_{tubes} and the internal area of a single tube:

$$A_i = \pi \cdot d_i \cdot l_t \cdot N_{tubes} \tag{3.7}$$

The external heat transfer area A_o is the sum of the external prime area of the tubes surface and the A_{fins} finned surface area:

$$A_o = A_{prime} + A_{fins} \tag{3.8}$$

The presence of liquid condensate or frost on the external surface will reduce the minimum free flow area A_{ff} and consequently the heat exchanger compactness σ. The external heat transfer area A_o will be reduced as well. To know how this effects affects the model see chapter 3.

The main geometrical characteristics of the SorTech AG RCS 08 are reported in the following table:

Table 3.1 SorTech AG RCS 08 geometrical characteristics

Geometrical parameter		Unit	Value
Coil	Number of water circuits, $N_{circuits}$	[-]	12
	Number of rows, N_{rows}	[-]	6
	Number of strings, $N_{strings}$	[-]	21
	Frontal area, A_{fr}	[m^2]	1.95
	Heat exchanger compactness, σ	[-]	0.674
	External heat transfer area, A_o	[m^2]	221.4
	Internal heat transfer area, A_i	[m^2]	8.79
Fans	Number of fans, N_{fans}	[-]	2
	Fan casing width, w_{fan}	[m]	1.050
	Fan casing length, l_{fan}	[m]	0.925
Tube	Number of tubes, N_{tubes}	[-]	126
	Transversal tube pitch, P_t	[mm]	25
	Longitudinal tube pitch, P_l	[mm]	50
	Internal tube diameter, d_i	[mm]	12
	External tube diameter, d_o	[mm]	14

Fin	Number of fins, N_{fins}	[-]	767
	Fin thickness, t_{fin}	[mm]	0.15
	Fin spacing, s_{fin}	[mm]	2.4
	Fin concentration, a_{fin}	[1/m]	415

3.1.1 Reference geometry and control volume

In order to simplify and generalize the analysis, it is essential to identify the geometrical modularity of the heat exchanger. This approach is aimed to modeling a reference coil configuration that can work for all the geometrical similar air-to-water heat exchangers despite their real configuration.

Firstly it is possible to recognize an overall modularity given by the number of fans N_{fans}.

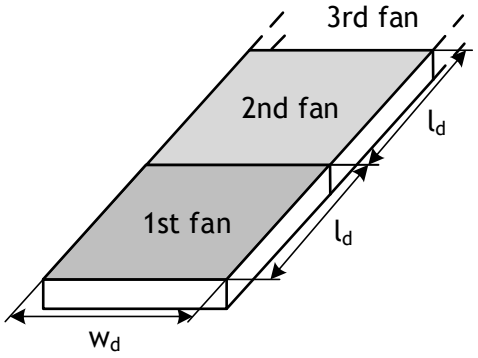

Figure 3.8 Heat exchanger modularity by fan

In fact, the model can be applied to all the heat exchangers realized by applying a series of fans on a bank of finned tubes.

Modeling a reference circuit can lead to a second modularity. Independently of the different circuit pattern present in the coil, the reference circuit pattern can be identified by knowing the number of tubes N_{tubes}, rows N_{rows} and circuits $N_{circuits}$ only.

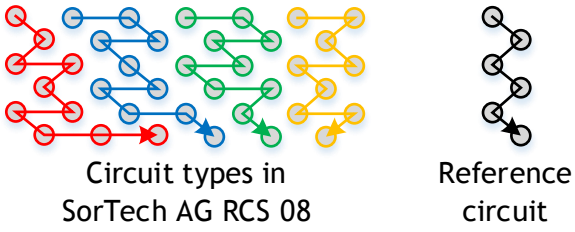

Figure 3.9 Real and reference circuits.

In the model the tubes are organized into $N_{circuits}$ single passes arranged in staggered rows, counterflow respect to the air stream. The single pass identifies the average circuit that can be adopted as reference. Thus, the reference tube length per row $l_{t,REF}$ is related to the real tube length l_t in the following form:

$$l_{t,REF} = l_t \frac{N_{strings}}{N_{circuits}} \tag{3.9}$$

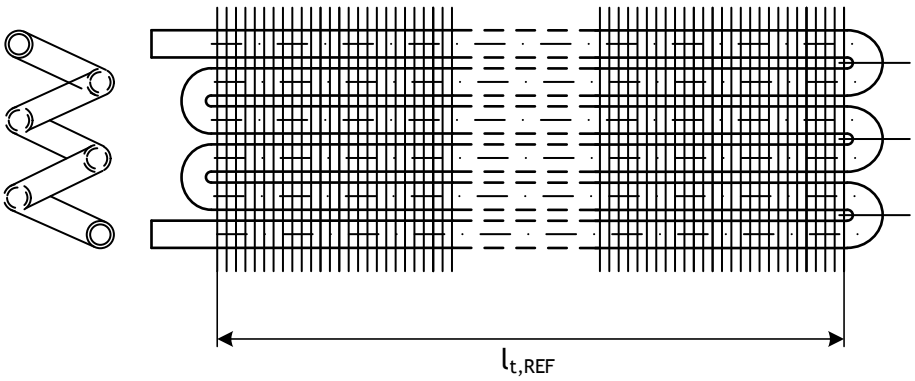

Figure 3.10 Reference circuit as single pass arranged is staggered rows

It is essential to note that this modified circuits pattern has the same internal A_i and external A_o heat transfer area, as well as the same frontal A_{fr} and free flow A_{ff} areas of the real geometry. The only difference consists in the variation of the circuit tube length per row $l_{t,REF}$, becoming a constant average length in the model.

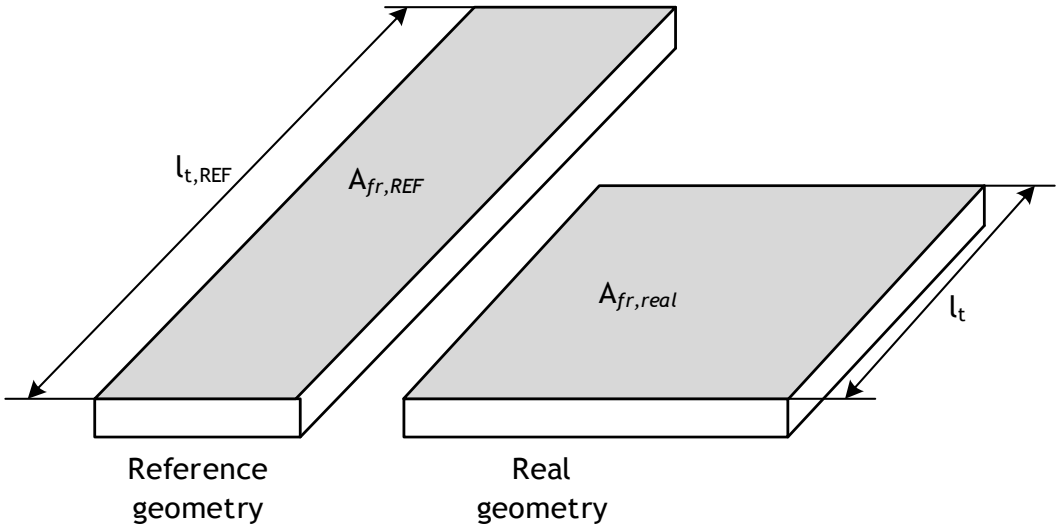

Figure 3.11 Real and reference coil geometry

Dividing the reference circuit in the N_{rows} tube segments of length $l_{t,REF}$ allows to identify the elemental control volume.

Hence, the control volume is identified by a single finned tube with real internal and external diameters and a reference length $l_{t,CV}$:

$$l_{t,CV} = l_{t,REF} \tag{3.10}$$

The dimensions, $w_{fin,CV}$ and $h_{fin,CV}$ of the fins portion considered in the control volume are:

$$w_{fin,CV} = P_t \tag{3.11}$$

and

$$h_{fin,CV} = P_l \tag{3.12}$$

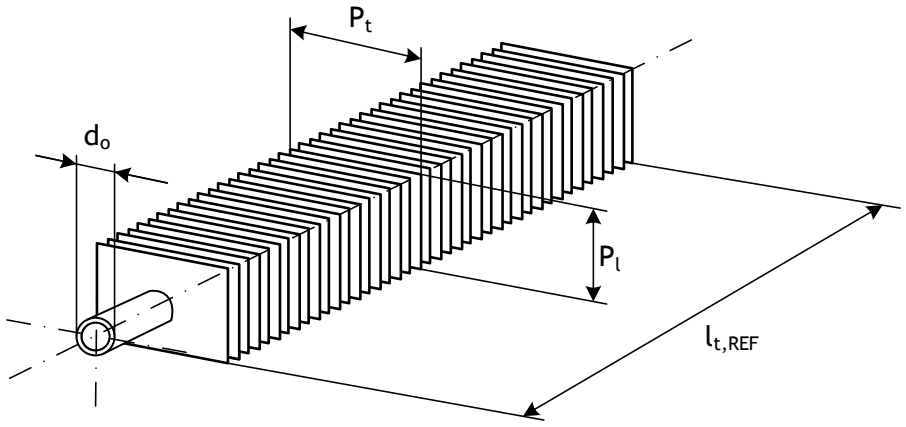

Figure 3.12 Control volume

Consequently, the internal $A_{i,CV}$ and external $A_{o,CV}$ heat exchange areas of the control volume are calculated respectively as

$$A_{i,CV} = (\pi \cdot d_i) \cdot l_{tube,CV} \tag{3.13}$$

and

$$A_{o,CV} = A_{t,prime,CV} + A_{fins,CV} = (\pi \cdot d_o) \cdot \left(l_{tube,CV} - N_{fins} \cdot t_{fin}\right) + 2\left(w_{fin,CV} \cdot h_{fin,CV} - \pi \cdot \frac{{d_o}^2}{4}\right) N_{fins} \tag{3.14}$$

The next figure represent the geometrical modeling process from the real heat exchanger geometry to the definition of the control volume:

As a consequence of assuming the single reference tube as control volume, the inlet and outlet conditions of both fluids (water and air) for each control volume located in a row are the same. Hence, the heat and mass transfer analysis valid for the control volume is also applicable to each single row. In particular, the row heat transfer areas are simply calculated by multiplying the respective control volume value for the number of circuits $N_{circuits}$:

$$A_{i,row} = A_{i,CV} \cdot N_{circuits} = (\pi \cdot d_i) \cdot l_{tube,CV} \cdot N_{circuits} \tag{3.15}$$

and

$$A_{o,row} = A_{t,prime,row} + A_{fins,row} = A_{o,CV} \cdot N_{circuits} = \left((\pi \cdot d_o) \cdot \left(l_{tube,CV} - N_{fins} \cdot t_{fin}\right) + 2\left(w_{fin,CV} \cdot h_{fin,eq} - \pi \cdot \frac{{d_o}^2}{4}\right) N_{fins}\right) N_{circuits} \tag{3.16}$$

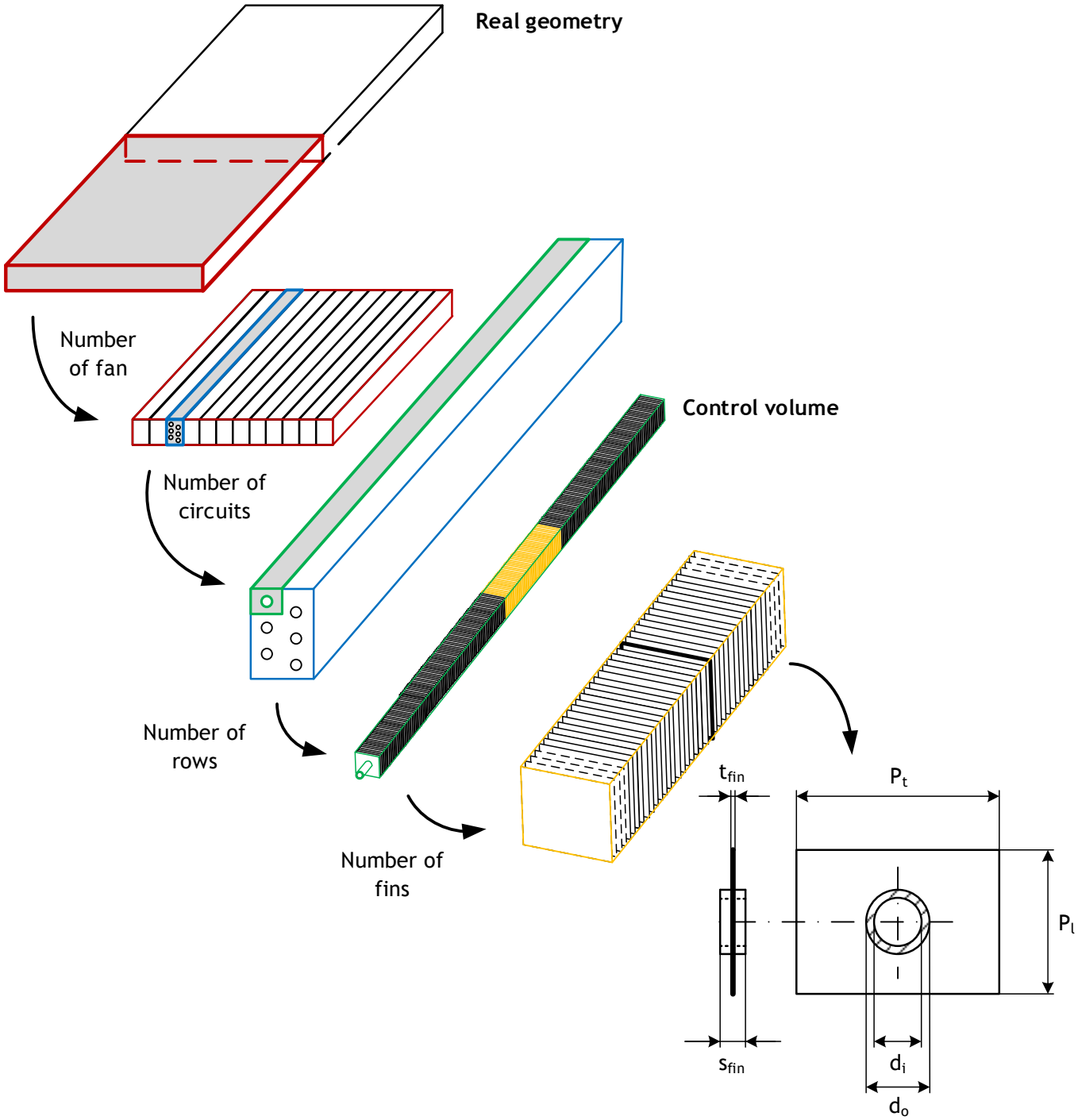

Figure 3.13 Heat exchanger geometrical modelling process

If a frost layer characterized by a thickness t_{frost} is present on a row, its geometrical parameters must be modified as follow. The fin surface area $A_{fins,row}$ becomes:

$$A_{fins,row} = \left(\left((p_t \cdot p_l) - \frac{\pi}{4}\left(d_o + 2 \cdot t_{frost,row}\right)^2\right) \cdot 2 \cdot N_{fins}\right) \cdot N_{strings} \quad (3.17)$$

and consequently, the row-heat transfer area $A_{o,row}$ results:

$$A_{o,row} = A_{fins,row} + A_{t,prime,row} = \left[\left(\left((p_t \cdot p_l) - \frac{\pi}{4}\left(d_o + 2 \cdot t_{frost,row}\right)^2\right) \cdot 2 \cdot N_{fins}\right) + \left(l_{tube,CV} - N_{fins}\left(t_{fin} + 2 \cdot t_{frost,row}\right)\right)\pi \cdot d_o\right] \cdot N_{strings} \quad (3.18)$$

The free flow area A_{ff} of a frosted row is calculated by accounting the obstruction of frosted fins and tubes on the heat exchanger frontal area A_{fr}:

$$A_{ff,row} = A_{fr} - \left[\left(d_o + 2 \cdot t_{frost,row}\right) \cdot \left(l_{tube,CV} - N_{fins} t_{fin} + 2 \cdot t_{frost,row}\right) \cdot N_{strings} + \left(\left(t_{fin} + 2 \cdot t_{frost,row}\right) \cdot w_d\right) \cdot N_{fins}\right] \quad (3.19)$$

According to its definition **Error! Reference source not found.**, the external hydraulic iameter is:

$$d_{h,o,row} = \frac{4 \cdot A_{ff,row} \cdot p_l}{A_{o,row}} \quad (3.20)$$

Also the height $h_{fin,eq}$ of the equivalent circular fin must be corrected accounting for the present of frost:

$$h_{fin,eq,row} = r_{fin,eq} - \frac{\left(d_o + 2 \cdot t_{frost,row}\right)}{2} \quad (3.21)$$

3.2 Main routine

The developed model has been written as FORTRAN© routine and implemented in a new type for dynamic simulations using the TRNSYS©.

The model is structured in modules that are executed in sequent or alternative order as showed in the flow chart reported at the end of this paragraph .

First at all, the type parameters are read in and the congruency with their allowed limits is checked. The following table reports the parameters, the limits of their variability and their default values.

Table 3.2 Model parameters: number, description, allowed variation range and unit

	Parameter description	Symbol	Allowed range (default values)	Unit
1	Number of fans	N_{fans}	$N_{fans} \geq 1$ (2)	-
2	Fan casing length	l_{fan}	$l_{fan} > 0$ (0,925)	m
3	Fan casing width	w_{fan}	$w_{fan} > 0$ (1,050)	m
4	Number of tubes	N_{tubes}	$N_{tubes} \geq N_{rows}$ (126)	-
5	Number of rows	N_{rows}	$1 \leq N_{rows} \leq 20$ (6)	-
6	Number of circuits	$N_{circuits}$	$1 \leq N_{circuits} \leq N_{strings}$	-

				(12)	
7	External tube diameter		d_o	$d_o > 0$ (0,014)	m
8	Internal tube diameter		d_i	$0 < d_i < d_o$ (0,012)	m
9	Fin thickness		t_{fin}	$t_{fin} > 0$ ($1{,}5 \cdot 10^{-4}$)	m
10	Fin spacing		s_{fin}	$s_{fin} > 0$ ($2{,}4 \cdot 10^{-3}$)	m
11	Longitudinal tube pitch		p_l	$p_l > d_o$ (0,025)	m
12	Transversal tube pitch		p_t	$p_t > d_o$ (0,050)	m
13	Type of glycol		GLY	0 or 1 (0)	-
14	Glycol mass concentration		γ	$0 \leq \gamma \leq 1$ (0,4)	% (base 1)
15	Inlet water pressure		$p_{w,in}$	$p_{w,in} > 0$ (1)	bar
16	Thermal conductivity of the fin material		k_{fin}	$k_{fin} > 0$ (752,4)	kJ/(h m^2)
17	Thermal conductivity of the tube material		k_{tube}	$k_{tube} > 0$ (1422)	kJ/(h m^2)
18	Maximal fan rotational speed		ω_{max}	$\omega_{max} > 0$ (900)	rpm
19	Volumetric flow rate induced by a single fan at the maximal rotational speed		$\dot{V}_{fan}(\omega_{max})$	$\dot{V}_{fan}(\omega_{max}) > 0$ (8000)	m^3/h
20	Coefficients for the volumetric flow rate correlation	1st coefficient	$c_{v1,fan}$	(-3,0121)	-
21		2nd coefficient	$c_{v2,fan}$	(7,2403)	-
22		3rd coefficient	$c_{v3,fan}$	(-6,4414)	-
23		4th coefficient	$c_{v4,fan}$	(3,2129)	-
24	Electrical power consumption of a single fan at the maximal rotational speed		$\dot{W}_{el,fan}(\omega_{max})$	$\dot{W}_{el,fan}(\omega_{max}) > 0$ (2520)	kJ/h
25	Coefficients for the electrical power consumption correlation	1st coefficient	$c_{p1,fan}$	(-2,468795)	-
26		2nd coefficient	$c_{p2,fan}$	(4,862549)	-
27		3rdcoefficient	$c_{p3,fan}$	(-1,503527)	-
28		4th coefficient	$c_{p4,fan}$	(0,279464)	-
29		5th coefficient	$c_{p5,fan}$	(0)	-
30	Fan working mode		$MODE$	0; 1; 2; 3 (2)	-
31	Maximal allowed relative rotational speed		$y_{fan,max}$	$y_{fan,min} < y_{fan,max} \leq 1$ (1)	% (base 1)
32	Minimal allowed relative rotational speed		$y_{fan,min}$	$0 \leq y_{fan,min} \leq y_{fan,max}$ (0)	% (base 1)

If one of the parameters exceeds its variation range a fatal error is reported and the simulation will be stopped.

It has to be mentioned that the control on both minimal $y_{fan,min}$ and maximal $y_{fan,max}$ allowed relative rotational speed is needed only when the fan is working in mode 1 or 2. The control on the maximal allowed relative rotational speed $y_{fan,max}$ is maintained also for working mode 0, whereas for the working mode 3 none of this two control is needed.

Once that parameters and input are read, the model proceeds with the calculation of the geometrical characteristics of the heat exchanger that are not influenced by the presence of a frost layer as reported in the previous paragraph. The geometrical characteristics of

the heat exchanger with unfrosted surfaces are calculated are evaluated the first time the type is called and are maintained as long as the type parameters do not change.

The next step consists in the read in and control of the inputs as reported in the following table:

Table 3.3 Model inputs: number, description, symbol, allowed variation range and unit

	Input description	Symbol	Allowed range	Unit
1	Inlet water temperature	$T_{w,in}$	$T_{w,in} \geq 273.15$	°C
2	Water mass flow rate	$\dot{m}_w$	$\dot{m}_w \geq 0$	kg/h
3	Inlet air temperature (dry-bulb)	$T_{a,in}$	$T_{a,in} \geq 273.15$	°C
4	Inlet air relative humidity	$\varphi_{a,in}$	$0 \leq \varphi_{a,in} \leq 1$	% (base 1)
5	Inlet air pressure	$p_{a,in}$	$p_{a,in} > 0$	bar
6	Relative rotational speed set-point (only for working mode 3)	$y_{fan,set}$	$0 \leq y_{fan,set} \leq 1$	% (base 1)
7	Outlet water set-point temperature (only for working mode 0 and 1)	$T_{w,set}$	$T_{w,set} \geq 273.15$	°C
8	Inlet air – outlet water set-point temperature difference (only for working mode 2)	ΔT_{set}	$\Delta T_{set} \geq 0$	°C

After retrieving the stored frost characteristics from the previous time-step, a blockage control is done to check that the air flow channels are not completely obstructed by the accumulated frost.

Before the calculation of the thermal performance is started some bypass-conditions has to be verified. In fact if one of the following condition is verified, it results impossible to heat the water stream. The performance calculation modules will be skipped and the inlet water and air condition are set are outputs while the heat transfer rates results all zero

- no water mass flow rate ($\dot{m}_w = 0$ kg/h);
- inlet water and inlet air have the same temperature ($T_{w,in} = T_{a,in}$);
- relative rotational speed set-point equal to zero ($y_{fan,set} = 0$ %) for working mode 3;
- maximal relative rotational speed equal to zero ($y_{fan,max} = 0$ %) for working mode 0, 1 and 2;
- inlet water temperature greater than the inlet air temperature ($T_{w,in} \geq T_{w,in}$) for working mode 0, 1 and 2;

Calculation modules will be skipped too when the outlet water reference temperature results lower than or equal to the inlet water temperature ($T_{w,ref} \leq T_{w,in}$) (for working mode 0, 1 and 2). In this condition, even if possible, it is not need to heat the water stream.

Fan rotational speed/outlet water temperature convergence and row-inlet water temperature convergence are obtained by applying a bisection method. This algorithm has be chosen because it guarantee the determination of the solution if an appropriate range for the guess value is set and because of its simplicity. The bisection algorithm guides the guess values by reducing their variation range iteration after iteration, until the convergence criterion is satisfied.

Once the heat exchanger are calculated and the convergence on fan rotational speed ω and the outlet water temperature $T_{w,out}$, the type calculate the electrical fan performance as reported in chapter 2 . Then, after the storing of the resulting frost characteristics, the type returns the the following output variables, and the time-step simulation is concluded.

Table 3.4 Model outputs: number, description, symbol and unit

Number	Output description	Symbol	Unit
1 – N_{rows}	Row-Inlet water temperature	T_{w1}	°C
N_{rows}+1 - 2· N_{rows}	Row-Inlet air temperature (dry-bulb)	T_{a1}	°C
2· N_{rows}+1 - 3· N_{rows}	Row-Inlet absolute humidity	x_{a1}	kg_v/kg_a
3· N_{rows}+1 - 4· N_{rows}	Row-Inlet relative humidity	φ_{a1}	% (base 1)
4· N_{rows}+1 - 5· N_{rows}	Row-Outlet water temperature	T_{w2}	°C
5· N_{rows}+1 - 6· N_{rows}	Row-Outlet air temperature (dry-bulb)	T_{a2}	°C
6· N_{rows}+1 - 7· N_{rows}	Row-Outlet absolute humidity	x_{a2}	kg_v/kg_a
7· N_{rows}+1 - 8· N_{rows}	Row-Outlet relative humidity	φ_{a2}	% (base 1)
8· N_{rows}+1 - 9· N_{rows}	Row-Heat transfer rate	$\dot{Q}$	kJ/h
9· N_{rows}+1 - 10· N_{rows}	Row-Latent heat transfer rate	$\dot{Q}_{a,L}$	kJ/h
10· N_{rows}+1 - 11· N_{rows}	Row-Sensible heat transfer rate	$\dot{Q}_{a,S}$	kJ/h
11· N_{rows} + 1	Inlet water temperature	$T_{w,in}$	°C
11· N_{rows} + 2	Inlet air temperature (dry-bulb)	$T_{a,in}$	°C
11· N_{rows} + 3	Inlet absolute humidity	$x_{a,in}$	kg_v/kg_a
11· N_{rows} + 4	Inlet relative humidity	$\varphi_{a,in}$	% (base 1)
11· N_{rows} + 5	Outlet water temperature	$T_{w,out}$	°C
11· N_{rows} + 6	Outlet air temperature (dry-bulb)	$T_{a,out}$	°C
11· N_{rows} + 7	Outlet absolute humidity	$x_{a,out}$	kg_v/kg_a
11· N_{rows} + 8	Outlet relative humidity	$\varphi_{a,out}$	% (base 1)
11· N_{rows} + 9	Total heat transfer rate	$\dot{Q}_{tot}$	kJ/h
11· N_{rows} + 10	Total latent heat transfer rate	$\dot{Q}_{L,tot}$	kJ/h
11· N_{rows} + 11	Total sensible heat transfer rate	$\dot{Q}_{S,tot}$	kJ/h

11· N_{rows} + 12	Water mass flow rate	$\dot{m}_w$	kg/h
11· N_{rows} + 13	Air mass flow rate	$\dot{m}_a$	kg/h
11· N_{rows} + 14	Relative fan rotational speed	y_{fan}	% (base 1)
11· N_{rows} + 15	Electrical power consumption	$\dot{W}_{el,fan}$	kJ/h

Note that the number of outputs is not constant but it vary with the number of rows N_{rows} given as type parameter.

Once the geometry of each row is characterized, the thermophysical properties of the aqueous solution of glycol can be evaluated by calling the internal subroutine *"WaterProperties"*. By specifying the type of glycol GLY, its mass concentration γ and the inlet temperature $T_{w,in}$ and static pressure $p_{w,in}$, this subroutine returns the values of specific isobaric $c_{p,w}$, thermal conductivity k_w and dynamic viscosity μ_w and Prandtl number Pr_w of the water-glycol mixture heat inputs and outputs of this subroutine. The correlations used in this subroutine are reported in appendix C. If the temperature exceeds their applicability range, a warning message is printed to inform the user of the improper use of those correlations.

Similarly, an internal subroutine named *"AirProperties"* is called to evaluate the thermophysical properties of the moist air. Inputs of this subroutine are the inlet air condition, such as temperature $T_{a,in}$, absolute humidity $x_{a,in}$ and pressure $p_{a,in}$. Using the correlations reported in the appendix D, the subroutine is able to calculate density ρ_a, specific heat $c_{p,a}$, thermal conductivity k_a, dynamic viscosity μ_a and Prandtl Pr_a of the air stream as consequence. The subroutine also evaluate the frost point temperature $T_{a,fp}$ of the air stream at the given pressure $p_{a,in}$. As for the *"WaterProperties"* subroutine, if the temperature exceeds their applicability range, a warning message is printed to inform the user of the improper use of those correlations.

It is important to put in evidence that in the model the moist air properties, such as dry bulb temperature T_a, wet bulb temperature $T_{a,wb}$, relative humidity φ_a, dew point temperature $T_{a,dp}$, humidity ratio x_a, specific enthalpy i_a and density ρ_a are evaluated through the TRNSYS© Type 33, named *"Psychrometrics"*. This type allows the evaluation of the moist air properties using ASHRAE correlations and ideal gas law.

To calculate the water convective heat transfer coefficient h_i, the specific subroutine *"InternalConvection"* has been written. This subroutine implements the relationship presented in chapter 2. It requires the geometrical characteristic of the tube inner side, such as the cross-sectional area A_{cs}, the internal hydraulic diameter $d_{h,i}$ and the length of the tub e in the reference circuit $l_{t,ref}$. Moreover, it also requires the water mass flow rate $\dot{m}_w$, its dynamic viscosity μ_w and thermal conductivity k_w and like the values of Prandtl number Pr_a, Pr_w and inlet temperature $T_{a,in}$, $T_{w,in}$ of air and water.

Once the internal convective heat transfer coefficient h_i has be calculated, the internal overall heat transfer coefficient $(UA)_i$ and number of transport NTU_i can be calculated following the equations reported in chapter 2.

At this point is necessary to identify the fan-working mode because the execution of the incoming modules depends on it.

If the fans are working in mode 0, their rotational speed are set to the allowed maximum value ω_u calculated as:

$$\omega_u = y_{fan,max} \cdot \omega_{max} \tag{3.22}$$

Then, the algorithm to determine the correct value of the outlet water temperature $T_{w,out}$ is run.

For working mode 1, at first it is check if the air stream has the thermal potential to heat the water stream and reach the reference temperature $T_{w,ref}$: if the inlet air temperature $T_{a,in}$ results below the specified outlet reference temperature $T_{w,ref}$, the water stream can be heated but it will never reach the outlet reference temperature $T_{w,ref}$ even if the fan is working at its maximal capacity. In this condition, the execution of the algorithm to determine the correct fan rotational speed will returns the maximum value of the fan rotational speed under the aim to obtain the minimal difference between the actual value of the outlet water temperature $T_{w,out}$ with respect to its reference value $T_{w,ref}$. In order to minimize the computational time, the algorithm to determine the correct value of the outlet water temperature $T_{w,out}$ is applied at the maximal allowed fan rotational speed ω_u. Whereas, if this condition is not verified the algorithm to determine the correct fan rotational speed is applied.

When the fan is working in mode 2, the outlet reference temperature $T_{w,ref}$ can be at maximum equal to the air temperature $T_{a,in}$: this condition is verified when the set-point temperature difference ΔT_{set} is set to zero. In all the other cases the reference temperature $T_{w,ref}$ is calculated by subtracting the set-point temperature difference ΔT_{set} from the inlet air temperature $T_{a,in}$ and it will be implicitly lower than this value. Hence, in mode 2 the algorithm to determine the correct fan rotational speed can directly applied except when the set-point temperature difference ΔT_{set} is set to zero: in this case the the fan rotational speed is set to its maximal allowed value ω_u and the algorithm to determine the correct value of the outlet water temperature $T_{w,out}$ will be applied.

In mode 3, the fan rotational speed is fixed at the given set point ω_{set}, calculated as follows:

$$\omega_{set} = y_{fan,set} \cdot \omega_{max} \tag{3.23}$$

The correct value of the outlet water temperature $T_{w,out}$ is determined by running the specific algorithm as for the working mode 0.

Depending on the selected fan working mode, for each fan rotational speed ω and outlet water temperature $T_{w,out}$ couple of values, it can be determine the total heat transfer rate $\dot{Q}_{tot}$ between air and water streams. This total heat transfer rate $\dot{Q}_{tot}$ is calculated as sum of the heat transfer rate $\dot{Q}$ that are exchanged at each row:

$$\dot{Q}_{tot} = \sum_{1}^{N_{rows}} \dot{Q} \tag{3.24}$$

Table 3.5 Fan-working mode

	Fan working mode 0	Fan working mode 1	Fan working mode 2	Fan working mode 3
Fan rotational speed, ω [rpm]	Maximum or minimum allowed valued ω_l ; ω_u	Variable value between the allowed range $\omega_l \leq \omega \leq \omega_u$	Variable value between the allowed range $\omega_l \leq \omega \leq \omega_u$	Assigned by the set point ω_{set}
Outlet water temperature, $T_{w,out}$ [°C]	Variable between the inlet water and inlet air temperature $T_{w,in} \leq T_{w,out} \leq T_{a,in}$	Assigned by the set point* $T_{w,ref}$	Assigned by the set point* $T_{w,ref}$	Variable between the inlet water and inlet air temperature $T_{w,out} \in (T_{w,in}; T_{a,in})$

* When is impossible to reach the reference value $T_{w,ref}$ in the allowed range for the fan rotational speed ω, the actual value of the outlet water temperature $T_{w,out}$ must be determine

Because the two streams are in overall counterflow, this determination cannot be done directly but, it is necessary to apply a reverse approach. Hence, the rows has been ordered following the air path, as shows in the next figure.

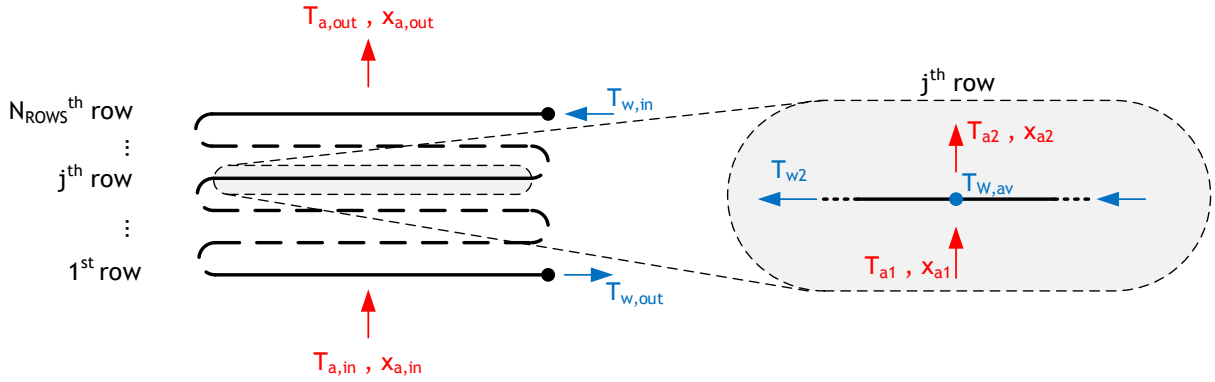

Figure 3.14 Global- and row-inlet/outlet conditions for a water reference circuit

Starting from the first row blown by the air stream (outlet water row), the heat and mass transfer equations reported in the previous chapter are resolve simultaneously, row by row. This results in the sequential determination of inlet and outlet water and air conditions at each row.

Once the inlet water temperature T_{w1} and outlet air condition T_{a2}, x_{a2} of a row are determined, this values becomes the outlet water temperature T_{w2} and the inlet air conditions T_{a1}, x_{a1} of the sequent row and bisection method on T_{w1} can be applied again. This process must be repeated for each row following the air stream, until all the row-performance are determine. Then the the total air heat transfer rate $\dot{Q}_{a,tot}$ can be account

as sum $\sum \dot{Q}_a$ of the single row values. Finally, this value can be compared with the total heat transfer rate of the water $\dot{Q}_{w,tot}$ in order to determine the next couple of outlet water temperature $T_{w,out}$ or fan rotational speed ω as explained in the sequent paragraphs

Each guess value of T_{w1} involves different heat and mass transfer phenomena on the external row-surface due the variation in its temperature. In order to choose between the thermal performance evaluation under wet or dry conditions, the tube temperature T_{tube} on each row has be chosen as critical variable, because it represent the lowest temperature encountered on the row surfaces. For each guess value of the inlet water temperature T_{w1}, the tube temperature T_{tube} is calculated as reported in the paragraph 2.5.

To avoid numerical indetermination in the evaluation of the effective saturation specific heat c_{sat} it is essential to limit the difference between row-outlet T_{w2} and inlet $T_{w,in}$ water temperatures. Hence, when the row-inlet water temperature variation range becomes to small, the saturated air enthalpies to calculate c_{sat} are evaluated at two different temperature around the inlet water value $T_{w,in}$:

$$c_{sat} = \frac{i_{sat,a}(T_{w,in} + dT) - i_{sat,a}(T_{w,in} - dT)}{(T_{w,in} + dT) - (T_{w,in} - dT)} \tag{3.25}$$

It has to be mentioned that this condition is encountered only when the air heat transfer rate equals or exceeds the total heat transfer rate of the water $\dot{Q}_{w,tot}$ before reaching the last rows. In other words, when the inlet water temperature is reached before the last rows. A satisfactory value to limit the row-inlet water temperature variation range can be assume at 10^{-3} °C. In fact, this value allow to avoid numerical problem and at the same time, it does not influence the simulation results. Furthermore, to avoid numerical problem with the calculation of c_{sat} around 0°C, the increment/decrement of the inlet water temperature dT has been set at 1 °C.

To quantify the row-air heat transfer rate $\dot{Q}_a$ two ε-NTU methods has been combined in a single common subroutine called ***"EfffectivenessNTU"***. Some row geometrical characteristics and fluids conditions must be specified: equivalent fin height $h_{fin,eq}$, its thermal conductivity, k_{fin} and thickness t_{fin}, total A_o and finned external area $A_{fins,o}$, internal NTU NTU_i, frost thermal conductivity k_{frost} and thickness t_{fin}, effective air enthalpy at the row-inlet water temperature $i_a(T_{w,1})$, effective saturation specific heat c_{sat}, water $\dot{m}_w$ and air $\dot{m}_a$ mass flow rate, water $c_{p,w}$ and air $c_{p,a}$ specific heat, row-inlet air enthalpy $i_{a,1}$, row-external convective coefficient h_o. To the end of choosing between the air-side effectiveness ε_a expressions also the row-order is required. The subroutine gives the value of the air heat transfer rate $\dot{Q}_a$ and of the fin parameter ξ for the considered row. This last parameter will be needed to calculate the fin temperature T_{fin}.

Once the row-heat transfer rate delivered by air $\dot{Q}_a$ and the received by water $\dot{Q}_w$, it is possible to evaluate sensible $\dot{Q}_{a,S}$ and the latent $\dot{Q}_{a,L}$ heat transfer rate using the bypass factor BF as presented in chapter 2. If the predicted values of temperature $T_{a,2}$ and absolute humidity $x_{a,2}$ are associated to a point in the fog zone, a bisection method is used to determine the outlet saturated air conditions at the given enthalpy value $h_{a,2}$.

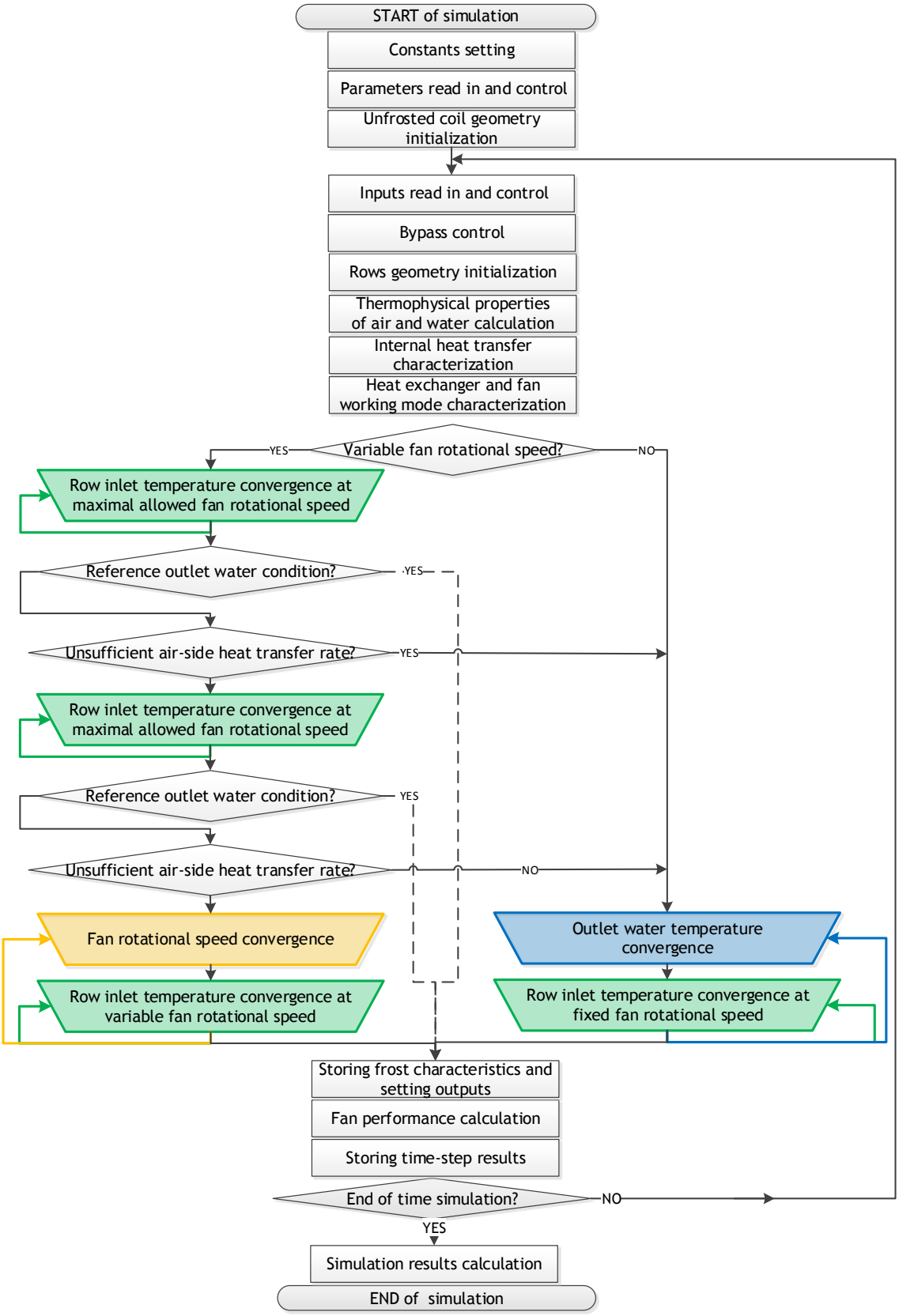

Figure 3.15 Main flow chart

3.2.1 Row-inlet temperature determination

The outlet water temperature T_{w2} and the air inlet conditions T_{a1}, x_{a1} at the first row are known from the reference $T_{a,ref}$ or guess value T_{wout} of the outlet water temperature T_{wout} and the given inlet air condition $T_{a,in}$, $x_{a,in}$. Hence, the thermal performance of the first row can be evaluated by guessing the inlet water temperature and T_{w1} and calculating the associated outlet air conditions T_{a2}, x_{a2}, until the row-heat transfer rates of air $\dot{Q}_a$ and water $\dot{Q}_w$ coincide.

To improve the calculation efficiency at each row, a bisection method is applied to the determine the correct value row-inlet water temperature T_{w1}. The variation range for this temperature will be constrain between the row-outlet water temperature T_{w2} and the (global) inlet water temperature $T_{w,in}$. When the water stream is heated ($T_{a,in} > T_{w,in}$) and the water row-heat transfer $\dot{Q}_w$ results higher than the air one $\dot{Q}_a$, the row-inlet water temperature T_{w1} must decrease, whereas if the $\dot{Q}_w$ results lower than $\dot{Q}_a$, the the row-inlet water temperature T_{w1} must be increased. Similarly, when the water stream is cooled ($T_{a,in} > T_{w,in}$ under fan working mode 3) the behavior of the row-inlet water temperature T_{w1} must be the opposite.

The qualitative trends for the row-heat transfer rates by varying the row inlet water temperature are reported in figure 4.3.

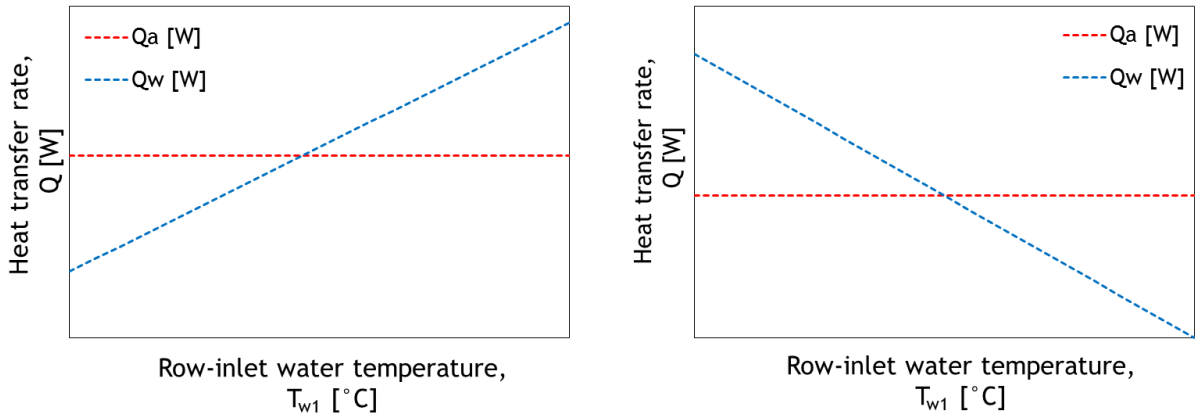

Figure 3.16 Qualitative trend of the row-heat trasnsfer rate of air and water in cooling (left) and heating (right) mode by varying the row-inlet water temperature.

3.2.2 Fan rotational speed determination

When the fan is working in mode 1 or 2 it is necessary to determine the value of the fan rotational speed ω that permits to reach the outlet water temperature $T_{w,ref}$. The correct value of the fan rotational speed ω is reached when the total air heat transfer rate $\dot{Q}_{a,tot}$ coincides with the total heat transfer rate of the water $\dot{Q}_{w,tot}$ when it reach its reference temperature $T_{w,ref}$:

$$\dot{Q}_{w,tot} = (\dot{m}_w c_{p,w}) \cdot (T_{w,out} - T_{w,in}) = (\dot{m}_w c_{p,w}) \cdot (T_{w,ref} - T_{w,in}) \quad (3.26)$$

A bisection method has been implemented to assure the convergence of the fan rotational speed to its correct value ω. First at all, it is necessary do define the upper ω_u and lower limits ω_l of the allowed range of the fan speed. This values can be calculated from the

relative fan rotational speeds, $y_{fan,max}$ and $y_{fan,min}$, and the maximal fan rotational speed ω_{max} given as type parameters:

$$\omega_u = y_{fan,max} \cdot \omega_{max} \tag{3.27}$$

$$\omega_l = y_{fan,min} \cdot \omega_{max} \tag{3.28}$$

When the total air heat transfer rate $\dot{Q}_{a,tot}$ exceeds the total heat transfer rate of the water $\dot{Q}_{w,tot}$ the air mass flow rate $\dot{m}_a$ must decrease and the fan rotational speed ω as consequence must decrease too. At the contrary when the total air heat transfer rate $\dot{Q}_{a,tot}$ is lower than the water value $\dot{Q}_{w,tot}$ the fan rotational speed ω must be increased. This trends is shown in the following figure:

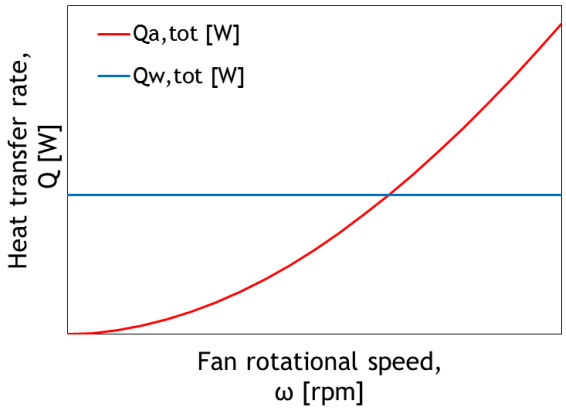

Figure 3.17 Qualitative trend of the total heat trasnsfer rate of air and water in cooling (left) and heating (right) mode by varying the outlet water temperature.

To reduce the computational time before applying the bisection method a first evaluation of the heat exchanger performance at the upper limit speeds ω_u is done. If this evaluation shows that the heat exchanger is not capable to heat up the water stream to its reference temperature $T_{w,ref}$, is not necessary to apply the bisection method to the fan rotational speed: to minimize the difference between the actual outlet water temperature $T_{w,out}$ and the reference value $T_{w,ref}$, the fan will work at its maximal allowed speed ω_u. Here the algorithm to determine the actual outlet water temperature $T_{w,out}$ must be run. If the evaluation at the fan rotational ω_u results in too high total air heat transfer rate $\dot{Q}_{a,tot}$ it means that the reference temperature $T_{w,ref}$ can be reached at lower speed. Hence, if the minimal allowed fan rotational speed ω_l is not null, the heat exchanger performance at this speed the are evaluated. If the total air heat transfer rate $\dot{Q}_{a,tot}$ result again higher than the one transfer to the water $\dot{Q}_{w,tot}$, is not necessary to apply the bisection method to the fan rotational speed: already at the minimal fan rotational speed the outlet water reference will be exceeds. The algorithm to determine the actual outlet water temperature $T_{w,out}$ must be run at the minimal fan rotational speed ω_l.

It has to be mentioned that if the water stream reach exactly the outlet water reference temperature at ω_u or at ω_l and at the same time the two heat transfer rates coincide, no further evaluation are required to determine the fan rotational speed ω and the outlet water temperature $T_{w,out}$.

Thus, only when the two previous evaluation shows that the water stream will exceed the reference temperature at the speed ω_u and not reach $T_{w,ref}$ at the minimal allowed speed ω_l, it will be necessary to apply the bisection method to the fan rotational speed ω.

3.2.3 Outlet water temperature determination

For a fixed value of the fan rotational speed ω (assigned or calculated), it's possible to determine the actual outlet water temperature $T_{w,out}$. As for the fan rotational speed determination, the correct value of the outlet water temperature $T_{w,out}$ is determine when the total heat transfer rates provided by the air stream $\dot{Q}_{a,tot}$ and received by the water flow $\dot{Q}_{w,tot}$ coincide. A bisection method is applied also in this occasion.

The extreme values between which the outlet temperature can vary depending on the condition under which the outlet water temperature must be determined. When fans are working in mode 0, the upper and the lower limit, $T_{w,out,u}$ and $T_{w,out,l}$ are set respectively to the inlet $T_{a,in}$ air and inlet water $T_{w,in}$ temperatures.

The same limits are set with fan working mode 1 or 2 and reference temperature $T_{w,ref}$ higher than or equal to the inlet air value $T_{a,in}$. When the fans are working at maximal allowed fan rotational speed the outlet reference temperature $T_{w,ref}$ can't be reach, the lower limit, $T_{w,out,u}$ and $T_{w,out,l}$ are set respectively to the outlet water reference $T_{w,ref}$ and to the inlet water $T_{w,in}$ temperatures. Whereas, when the fans are running at the minimal allowed fan rotational speed ω_l and the outlet reference temperature $T_{w,ref}$ is exceed, the limits of temperature, $T_{w,out,u}$ and $T_{w,out,l}$, are set to respectively to the outlet reference $T_{w,ref}$ and to the inlet air $T_{a,in}$ temperatures.

At least, when the fan-working mode is set to 3 the upper and lower limits of the outlet water temperature are set respectively at the minimum and at the maximum value between the inlet air $T_{a,in}$ and the inlet water $T_{w,in}$ temperature. In fact, when the fans rotational speed is controlled by an external signal $y_{fan,set}$ no control is done on the heat flow rate verse. In other words the water stream can be heated up or cooled down.

The limits for the outlet water temperature are resumed in the next table:

Table 3.6 Upper and lower limits for the outlet water temperature

Fan rotational speed, ω [rpm] (Fan-working mode)	ω_u(0)	ω_u(1 or 2) $(T_{a,in} < T_{w,ref})$	ω_u(1 or 2) $(T_{w,out}(\omega_u) < T_{w,ref})$	ω_l(1 or 2) $(T_{w,out}(\omega_u) > T_{w,ref})$	ω_{set}(3)
Upper temperature limit, $T_{w,out,u}$ [°C]	$T_{a,in}$	$T_{a,in}$	$T_{w,ref}$	$T_{a,in}$	$max\{T_{a,in}; T_{w,in}\}$
Lower temperature limit, $T_{w,out,l}$ [°C]	$T_{w,in}$	$T_{w,in}$	$T_{w,in}$	$T_{w,ref}$	$min\{T_{a,in}; T_{w,in}\}$

The criteria which the bisection range has to be varied depends on the fact that the water stream is heated or cooled: in the first case when the total air heat transfer rate $\dot{Q}_{a,tot}$ exceeds the total heat transfer rate of the water $\dot{Q}_{w,tot}$, the outlet water temperature $T_{w,out}$ must be increased, whereas if the water stream is cooled (only in mode 3) the outlet water temperature $T_{w,out}$ must decrease. The opposite behavior must be adopted when the total heat transfer rate of the water $\dot{Q}_{w,tot}$, is greater that the air one $\dot{Q}_{a,tot}$.

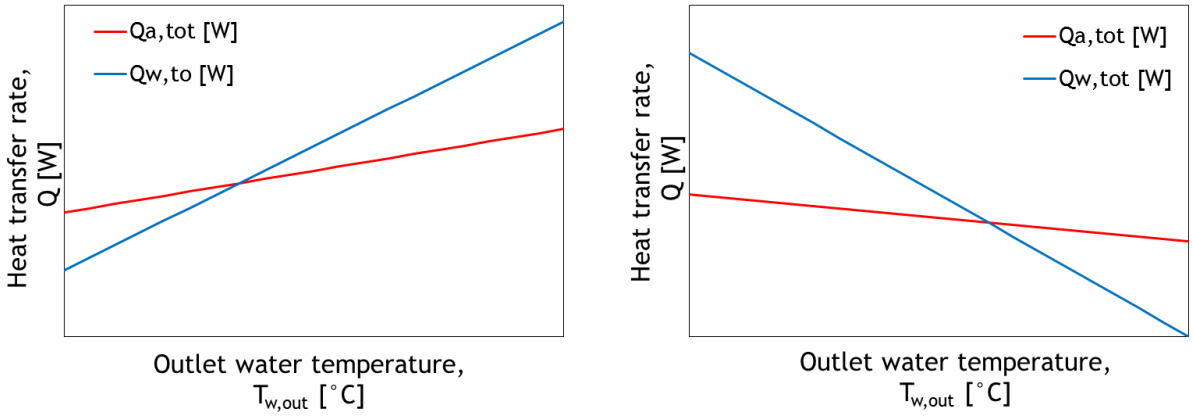

Figure 3.18 Qualitative trend of the total heat trasnsfer rate of air and water in cooling (left) and heating (right) mode by varying the outlet water temperature. Convergence criteria comparison

3.3 Numerical model optimization

In order to reduce the computational time a optimization of both bisection methods, on the fan rotational speed/outlet water temperature $\omega/T_{w,out}$ and on the row-inlet water temperature T_{w1} has done. The computational time has been considered proportional to the cumulative number of iterations on the row-inlet water temperature T_{w1}. Two different set of convergence criterion were compared. Once for the best convergence criterion has detected, the model behavior was inspected for four different tolerance values.

The comparisons were conducted under static condition based on two different set of inlet values for the water flow and for the air stream.

Table 3.7 Inlet conditions for air and water; Simulation condition

	Case A		**Case B**	
	Fan mode 2	Fan mode 3	Fan mode 1	Fan mode 3
Inlet water temperature, $T_{w,in}$ [°C]	-7,50	-7,50	-7,50	-7,50
Water mass flow rate, $\dot{m}_w$ [kg/h]	1200	1200	1200	1200
Inlet air temperature (dry-bulb), $T_{a,in}$ [°C]	-2,50	-2,50	2,00	2,00

Inlet air relative humidity, $\varphi_{a,in}$ [% base 1]	0,60	0,60	0,95	0,95
Inlet air pressure, $p_{a,in}$ [bar]	1,01325	1,01325	1,01325	1,01325
Relative rotational speed set-point, $y_{fan,set}$	/	0.183	/	0.300
Outlet water set-point temperature, T_{set}	/	/	-0.01	/
Inlet air–outlet water set-point temperature difference, ΔT_{set}	1,5	/	/	/
Simulation time step [s]	180 s			
Simulation duration [s]	1 time step (180 s)			
Maximal number of iterations on T_{w1}	100			
Maximal number of iterations on $\omega/T_{w,out}$	100			

This two cases were chosen because they are significant practical signification for the model: case A represent the average resulting condition from the available monitoring data (in this condition only sensible heat transfer is involved); case B is significant because the sensible and latent heat with frost formation are involved and the first convergence criteria fails.

Both cases were simulated for variable fan rotational speed ω and fixed outlet water reference temperature $T_{w,out}$ (Case A -mode 2 and Case B - mode 1) and for variable outlet water temperature $T_{w,out}$ and fixed fan rotational speed ω (Case A – mode 3 and Case B – mode 3).

3.3.1 Bisection converge criteria comparison

The first convergence criterion assures that the correct value for the fan rotational speed/outlet water temperature is determined when the total heat transfer difference $\Delta\dot{Q}_{tot}$ between air and water results under a given total heat transfer tolerance TOL_{tot}:

$$\Delta\dot{Q}_{tot} = \left|\dot{Q}_{w,tot}\right| - \left|\dot{Q}_{a,tot}\right| < TOL_{tot} \quad \text{(e.29)}$$

The same principle is applied for the bisection on the single row, where the correct value of row-inlet water temperature is assume to be reach when the row-heat transfer difference $\Delta\dot{Q}$ between air and water results under a given row-heat transfer tolerance TOL:

$$\Delta\dot{Q} = \left|\dot{Q}_{w}\right| - \left|\dot{Q}_{a}\right| < TOL \quad (3.30)$$

To avoid an erroneous behavior of the model, the total heat transfer tolerance TOL_{tot} should be higher than the row-heat transfer tolerance TOL. In the developed model the two tolerance are related in the following way:

$$TOL_{tot} = N_{rows} \cdot TOL \quad (3.31)$$

This choice permits to reach a total convergence on the fan rotational speed/outlet water temperature in the limit case where all the rows reach their convergence with a value slightly lower than the row-heat transfer tolerance TOL.

The second convergence criterion involves the determination of the absolute difference between the total heat transfer difference $\Delta\dot{Q}_{tot}$ of two consecutive iterations on the fan

rotational speed/outlet water temperature. This different is named total heat transfer error $\varepsilon_{\dot{Q},tot}$:

$$\varepsilon_{\dot{Q},tot} = \left|\Delta\dot{Q}_{tot}\right|^{j} - \left|\Delta\dot{Q}_{tot}\right|^{j-1} \tag{3.32}$$

where the upscript j identifies the iteration order on the fan rotational speed/outlet water temperature $\omega/T_{w,out}$. At the same way, a row-heat transfer error $\varepsilon(\dot{Q})$ can defines as:

$$\varepsilon_{\dot{Q}} = \left|\Delta\dot{Q}\right|^{i} - \left|\Delta\dot{Q}\right|^{i-1} \tag{3.33}$$

where the upscript i represents the iteration order on the row-inlet water temperature T_{w1}. When the row-heat transfer error $\varepsilon_{\dot{Q}}$results under the given value for the tolerance TOL the correct value of row-inlet water temperature is assume to be determined. Similary, the correct value of the fan rotational speed/outlet water temperature is reached when the total heat transfer error $\varepsilon_{\dot{Q},tot}$ is lower than the tolerance TOL. In this cases the use of the same value for the tolerance on the single row and the entire heat exchanger does not imply any erroneous behavior of the model.

For both convergence criteria, the heat transfer tolerance TOL was set to 0,001 W. Four different parameters has been compared for each simulation:

- cumulative number of iterations on the row-inlet temperature;
- number of iterations on the fan rotational speed/outlet water temperature;
- number of iterations on the row-inlet temperature for each fan rotational speed/outlet water temperature iteration;
- difference between the calculated and the given inlet water temperatures, named error on $T_{w,in}$.

Table 3.8 Convergence criteria comparison results

		Cumulative number of iterations on T_{w1} [-]	Number of iteration on ω [-]	Number of iterations on $T_{w,out}$ [-]	Error on $T_{w,in}$ [°C]
Case A fan mode 2	Convergence criterion $\Delta\dot{Q}$, $\Delta\dot{Q}_{tot}$	3148	18	/	$-7.293 \cdot 10^{-7}$
	Convergence criterion $\varepsilon_{\dot{Q}}$, $\varepsilon_{\dot{Q},tot}$	3163	23	/	$-7.293 \cdot 10^{-7}$
Case A fan mode 3	Convergence criterion $\Delta\dot{Q}$, $\Delta\dot{Q}_{tot}$	3474	/	22	$-2.918 \cdot 10^{-6}$
	Convergence criterion $\varepsilon_{\dot{Q}}$, $\varepsilon_{\dot{Q},tot}$	3011	/	24	$-7.293 \cdot 10^{-7}$
Case B fan mode 1	Convergence criterion $\Delta\dot{Q}$, $\Delta\dot{Q}_{tot}$	17874	100*	/	0.000*
	Convergence criterion $\varepsilon_{\dot{Q}}$, $\varepsilon_{\dot{Q},tot}$	3241	22	/	$-9.570 \cdot 10^{-7}$
Case B fan mode 1	Convergence criterion $\Delta\dot{Q}$, $\Delta\dot{Q}_{tot}$	3908	/	23	0.000*
	Convergence criterion $\varepsilon_{\dot{Q}}$, $\varepsilon_{\dot{Q},tot}$	3411	/	25	$-9.884 \cdot 10^{-7}$

* The error on $T_{w,in}$ results zero because on the last row (6th row) the convergence is not achieved and the row-inlet water temperature $T_{w1}(6)$ reach is lower limits, coinciding to the inlet water temperature $T_{w,in}$.

As can be noted from table 9.9, even if the number of iterations on the fan rotational speed/outlet water temperature increase, the cumulative number of iterations on the row-inlet temperature decrease when the convergence criterion based on the heat transfer error is adopted. This in mainly due to the reduced number of iterations on the inlet temperature foe those rows that don't reach convergence during the simulation process. In particular this difference can be noted for the first iterations on the fan rotational speed/outlet water temperature as confirm by the following charts.

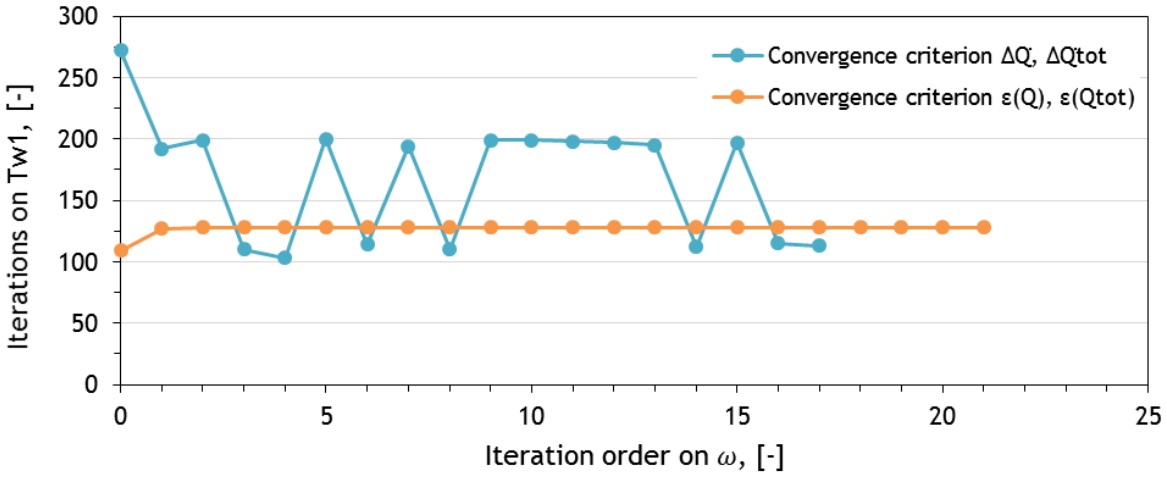

Figure 3.19 Number of iterations on the row-inlet temperature for each fan rotational speed/outlet water temperature (Case a – mode 2)

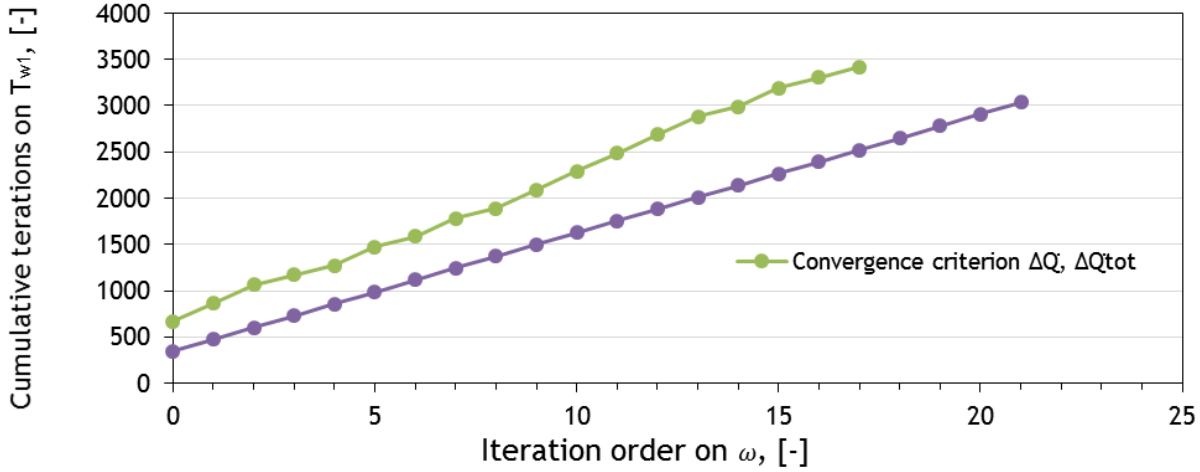

Figure 3.20 Cumulative number of of iterations on the row-inlet temperature (Case a – mode 2)

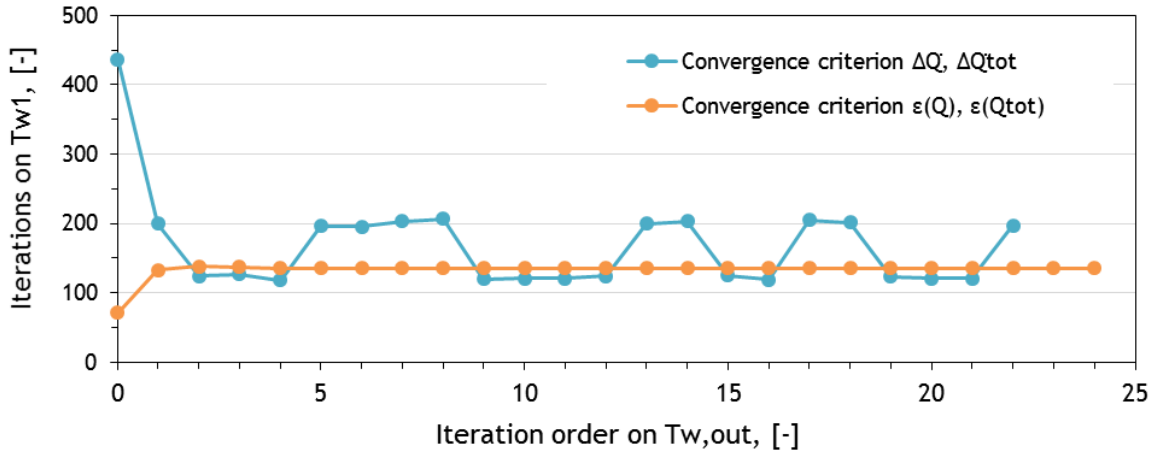

Figure 3.21 Number of iterations on the row-inlet temperature for each fan rotational speed/outlet water temperature (Case B – mode 3)

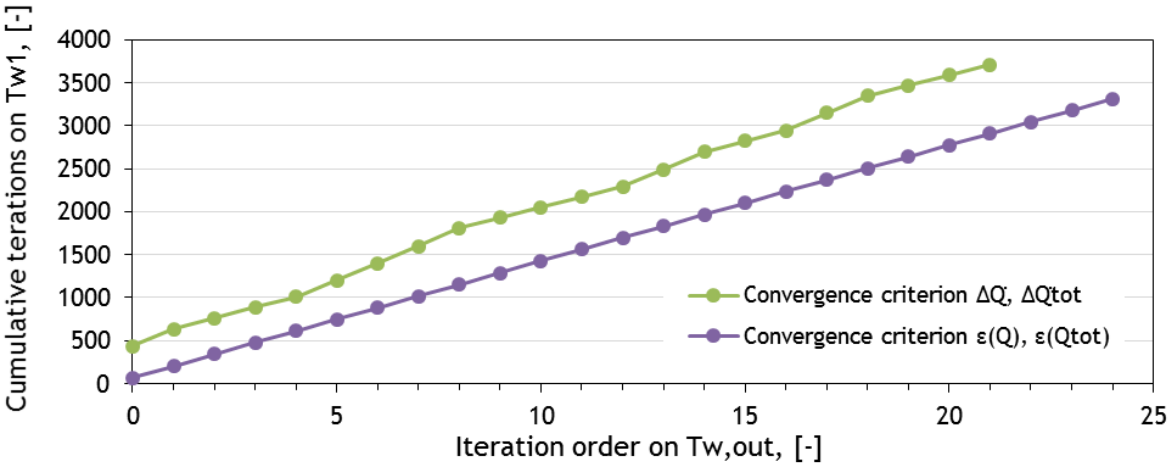

Figure 3.22 Cumulative number of of iterations on the row-inlet temperature (Case B – mode 3)

Another significant aspect that can be noted in the previous charts is the increment of the model stability adopting the convergence criterion based on $\varepsilon_{\dot{Q}}$, $\varepsilon_{Q,tot}$.

Based on the comparison results the convergence criterion on $\varepsilon_{\dot{Q}}$, $\varepsilon_{Q,tot}$ seems to reduce the computational effort and increase the stability of the model.

3.3.2 Tolerance comparison

A comparison between different values of heat transfer tolerance TOL has been done in order to determine the best compromise between model accuracy and computational time. Four values of heat transfer tolerance TOL were compared: 0,001 W, 0,01 W, 0,1 W and 1 W. The afore presented set of inlet water and air conditions (table 9.7) were taken into account for simulations.

The results of the comparison are reported in the following tables and charts.

Table 3.9 Tolerance comparison results (Case A – mode 2)

Compared parameter	Tolerance			
	0,001 W	0,01 W	0,1 W	1 W
Cumulative number of iterations on T_{w1} [-]	3163	2263	1559	1004
Number of iteration on ω [-]	23	20	16	13
Fan rotational speed, ω [rpm]	164,561	164,562	164,564	164,619
Total heat transfer rates provided by the air stream, $\dot{Q}_{a,tot}$ [W]	4309,139	4309,141	4309,126	4308,613
Total heat transfer difference between air and water, $\Delta\dot{Q}_{tot}$ [W]	$-6.595\cdot 10^{-4}$	$1,800\cdot 10^{-3}$	$1,399\cdot 10^{-2}$	$5,261\cdot 10^{-2}$
Total heat transfer error, $\varepsilon(\dot{Q}_{tot})$ [W]	$5,344\cdot 10^{-4}$	$4,275\cdot 10^{-3}$	$6,481\cdot 10^{-2}$	$5,466\cdot 10^{-1}$
Error on $T_{w,in}$ [°C]	$-7,293\cdot 10^{-7}$	$-5,834\cdot 10^{-6}$	$-9,336\cdot 10^{-5}$	$-7,464\cdot 10^{-1}$
Absolute difference between the total air heat transfer rates (with respect to TOL = 0.001 W) [W]	/	$1,111\cdot 10^{-3}$	$1,389\cdot 10^{-2}$	$5,267\cdot 10^{-2}$
Relative difference between the total air heat transfer rates (with respect to TOL = 0.001 W) [W]	/	$2,578\cdot 10^{-7}$	$3,223\cdot 10^{-6}$	$1,224\cdot 10^{-4}$

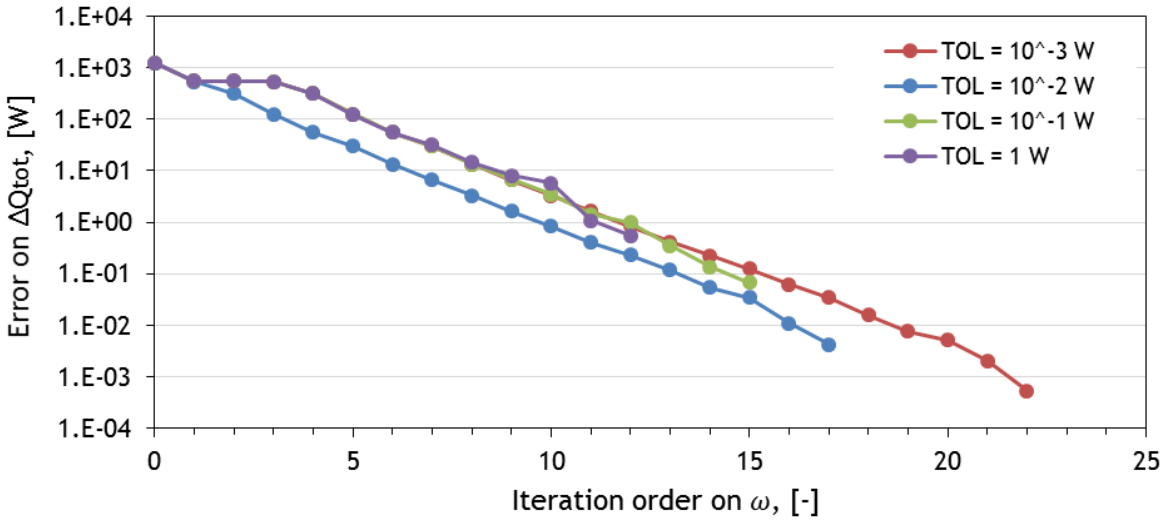

Figure 3.23 Total heat transfer error for different values of tolerance (Case A – mode 2)

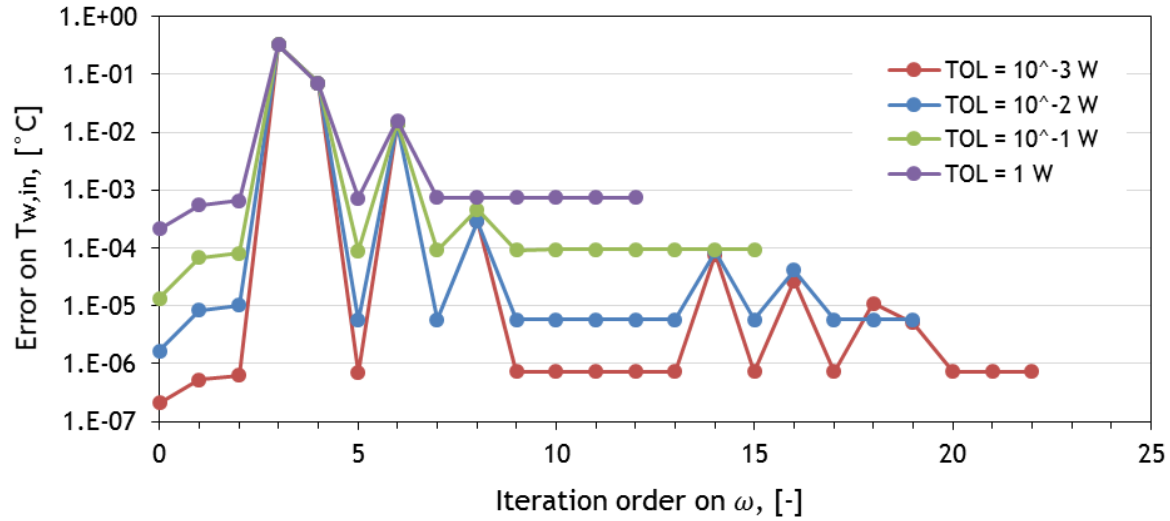

Figure 3.24 Error on the inlet water temperature for different values of tolerance (Case A – mode 2)

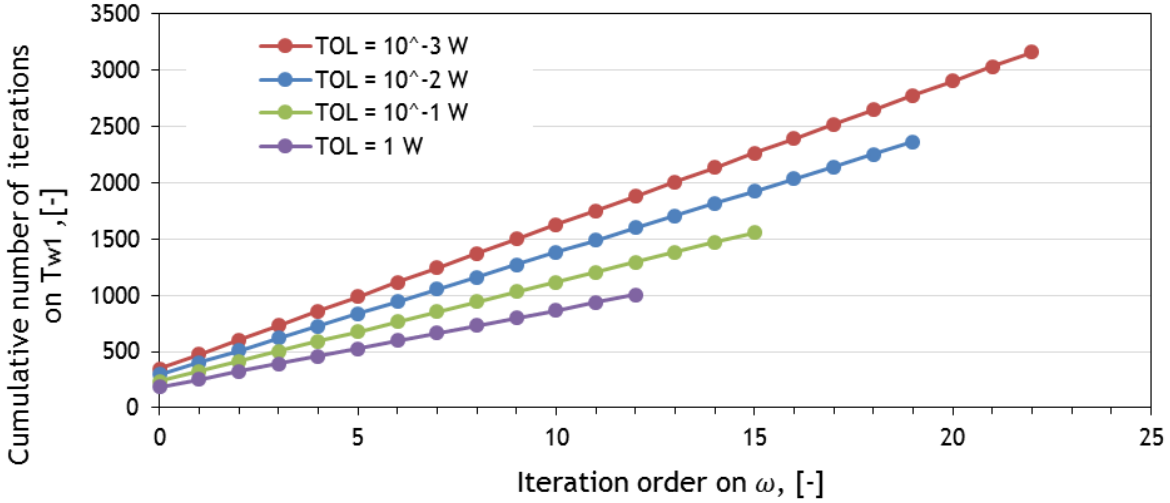

Figure 3.25 Cumulative number of iterations on the row-inlet temperature for different values of tolerance (Case A – mode 2)

Table 3.10 Tolerance comparison results (Case B – mode 3)

Compared parameter	Tolerance [W]			
	0,001	0,01	0,1	1
Cumulative number of iterations on T_{w1} [-]	3314	2381	1674	1094
Number of iteration on $T_{w,out}$ [-]	25	21	18	15
Outlet water temperature, $T_{w,out}$ [°C]	-0,096	-0,096	-0,096	-0,096

Total heat transfer rates provided by the air stream, $\dot{Q}_{a,tot}$ [W]	9115,978	9116,017	9116,057	9112,947
Total heat transfer difference between air and water, $\Delta\dot{Q}_{tot}$ [W]	5,208· 10^{-4}	4,637· 10^{-2}	1,390· 10^{-2}	3,676
Total heat transfer error, $\varepsilon(\dot{Q}_{tot})$ [W]	-9,884· 10^{-7}	-7,907· 10^{-6}	-6,325· 10^{-5}	-3,040· 10^{-3}
Error on $T_{w,in}$ [°C]	6,002· 10^{-4}	9,604· 10^{-3}	7,683· 10^{-2}	6,147· 10^{-1}
Absolute difference between the total air heat transfer rates (with respect to TOL = 0.001 W) [W]	/	3,972· 10^{-2}	7,972· 10^{-2}	3,031
Relative difference between the total air heat transfer rates (with respect to TOL = 0.001 W) [W]	/	4,357· 10^{-6}	8,745· 10^{-6}	3,324· 10^{-4}

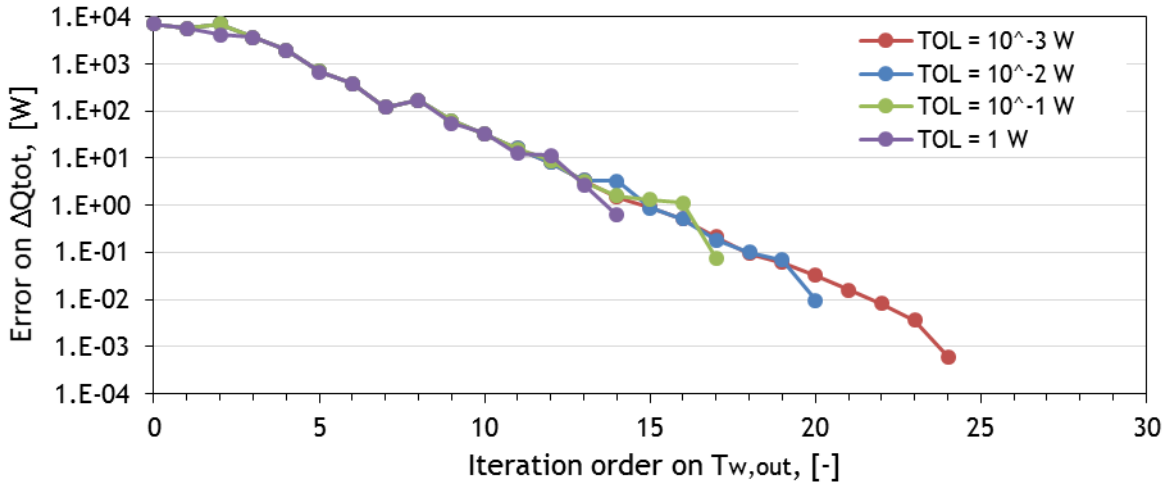

Figure 3.26 Total heat transfer error for different values of tolerance (Case B – mode 3)

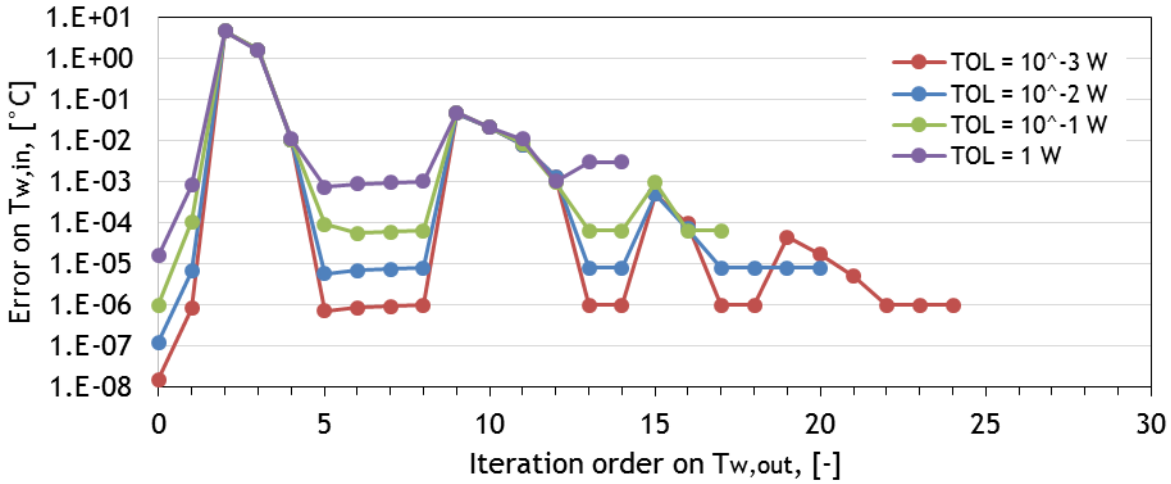

Figure 3.27 Error on the inlet water temperature for different values of tolerance (Case B – mode 3)

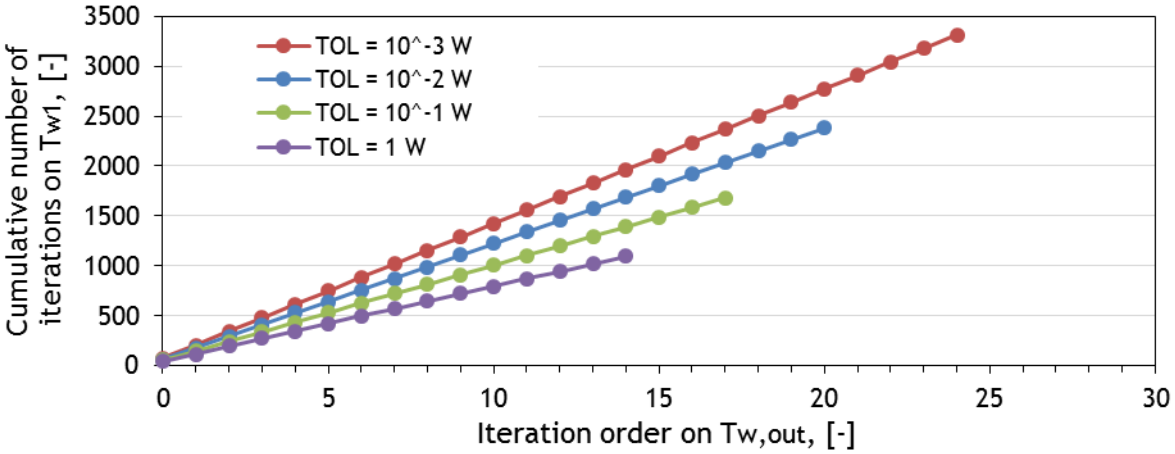

Figure 3.28 Cumulative number of iterations on the row-inlet temperature for different values of tolerance (Case B – mode 3)

As expected, more the tolerance value increase, so more the cumulative number of iteration on Tw1 reduces. This can be justified with a reduction in the number of iteration on both fan rotational speed/outlet water temperature and on the row-inlet temperature for each fan rotational speed/outlet water temperature iteration.

For case A, the difference of the predicted total heat transfer rate on the air side $\dot{Q}_{a,tot}$ between the different simulation is always under 0,1 W, that correspond to a relative difference under 1 %. Simulations results be considered satisfied for a maximal value of tolerance of 0,1 W. For tolerance of 1 W the resulting error on $T_{w,in}$ has been considered to be too high (-7,464· 10^{-1} °C).

For case B, the difference of the predicted total heat transfer rate on the air side $\dot{Q}_{a,tot}$ between the different simulation exceed 1 W at the maximum value of tolerance (1 W). It reaches 3,031 W, that corresponds to a relative difference under 0,1 %.

The monitoring temperature values are measured with a precision of 0,1 °C. In order to maintain the model precision under this value is appropriate to set the model tolerance to 0,01 W. In fact, for case B the error on $T_{w,in}$ results over 0,01 °C for tolerances over 0,1 W. Furthermore, the adoption of a heat transfer tolerance equal to 0,01 W allows a reduction in the cumulative iterations around 1/3 compared to the value at the minimal tolerance (0,001 W).

3.4 Model validation

To validate the developed model, a comparison between the monitoring data and the predicted values of fan electrical consumption, heat transfer rate and outlet water temperature is conducted. Single time-step simulations are run in order to obtain a validation of the model under static condition.

The monitored data are extrapolated from the monitoring results of a real installation during the month of February 2012. The comparison is conducted on selected data that

represent stable heat transfer conditions. A stable condition has been assumed each time the values of the heat transfer rate and the water mass flow rate present small variations around a fixed value.

A total number of 88 comparison are conducted under two fan-working mode. Initially the electrical consumption of the fan is compared under fan-working mode 1. Then, heat transfer rate and outlet water temperature are compared when the fan-working is set to 3.

The first set of simulation were run with the fans working in mode 1 and set-point temperature values assumed equal to the outlet water monitored temperatures. The results of the validation for the electrical fan consumption are shows in the following charts.

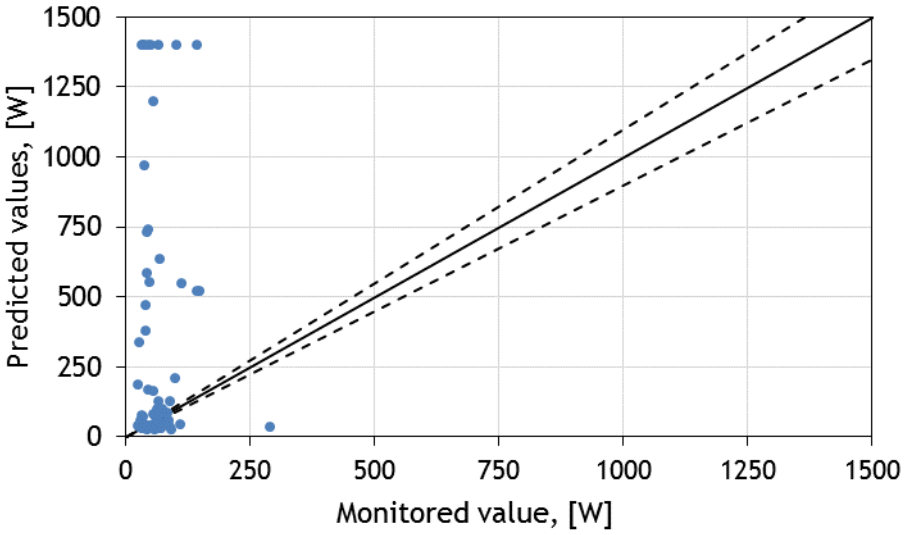

Figure 3.29 Electrical fan consumption comparison between predicted and monitored values

From figure 3.30 it results that the predictions are extremely above the respective monitored values, reflecting a higher prediction of the fan rotational speed. The mean average error results around 450 %.

This trend can be justify primary by measurement uncertainty of the available monitoring data. The temperature sensors have an uncertainty around 0,1 °C. In the encountered winter-heating condition, the temperature differences between inlet air and outlet water result particularly small, between 1,7 °C and 0,3 °C with an average value of 1,1°C. As consequence, the measurement uncertainty can lead to significant discrepancies between real value and monitored data. It has to be mentioned that, this discrepancies may not be recognized under summer-cooling conditions, where the temperature difference is more conspicuous, around 3 °C.

Moreover, the measured electrical power required by the fans in the simulated condition is always far below the maximal value 1400 W. In particular, it results below the 5%. The next figure shows the enlargement of the previous chart between 0 and 100 W. The adopted correlation has been derived from a limited number of monitored data. In particular the lowest electrical fan consumption value is only 90 W. Hence, in the encountered range no valid information are available. In this condition, an absolute

difference under 5% with respect to the maximal fan rotational speed can results in a high percentage of error between predicted and monitored data.

Hence, the comparison between monitored and predicted electrical fan consumption doesn't have to be considered a consistent method to validate the model.

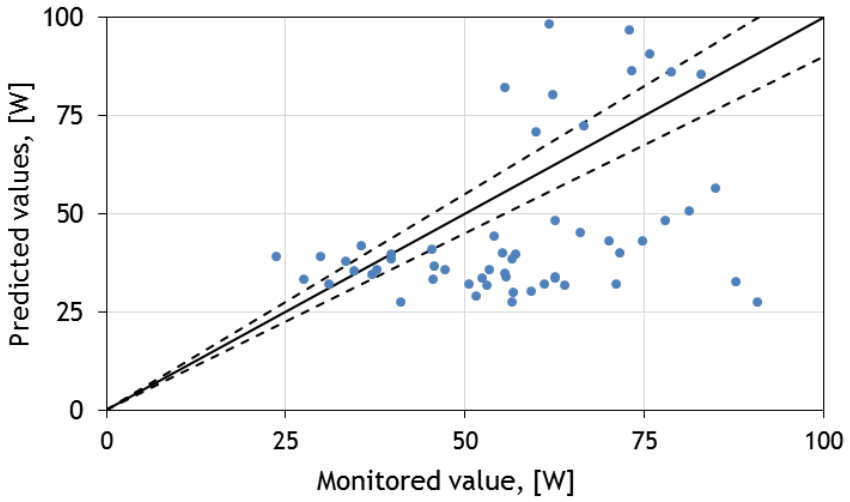

Figure 3.30 (Enlargement) Electrical fan consumption comparison between predicted and monitored values

To show the model prediction of heat transfer rate and outlet water temperature, all the previous simulation have been run under fan-working mode 3. The set-point relative fan speeds are obtained from the monitored values of the electrical fan consumption using the developed correlation in chapter 2.

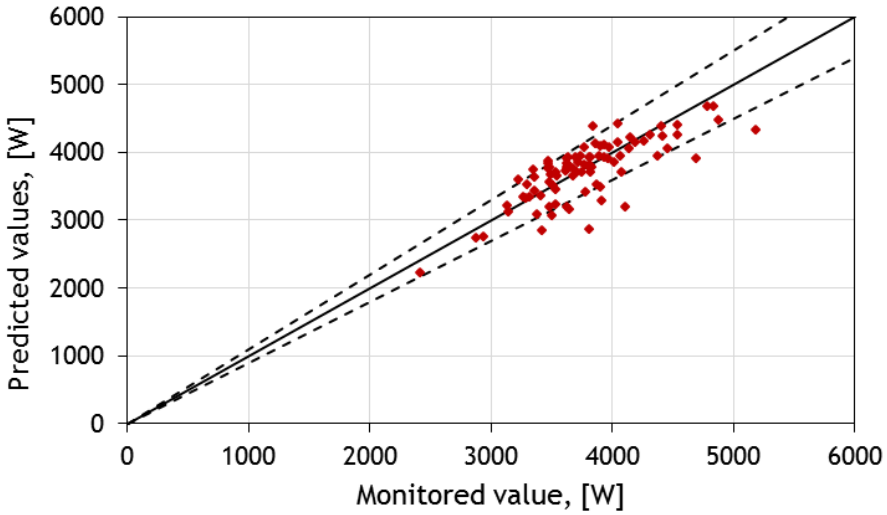

Figure 3.31 Heat transfer rate comparison between predicted and monitored values

The previous chart show a better accuracy in the prediction of the total heat transfer. The average error between monitored and predicted values is lower than 6%. The maximal value of the this error results 24,7 % encountered for the lowest value of the temperature

differences between inlet air and outlet water, 0,3°C. As for the electrical fan consumption comparison, by neglecting all those cases where the temperature differences between inlet air and outlet water becomes lower than 1°C, the average error in the heat transfer rate prediction becomes 4,21 %.

The previous observation about the inaccuracy of this correlation remains valid also for this set of simulation. Furthermore, the tendency to predicted lower fan electrical power, it reflects in an overestimation of the heat transfer rate for most of the simulated cases as can be seen in the enlargement of the next figure:

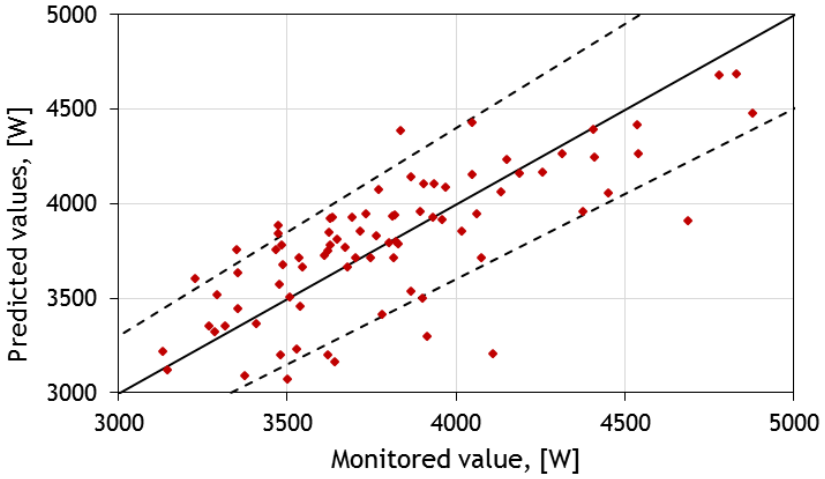

Figure 3.32 (Enlargement) Heat transfer rate comparison between predicted and monitored values

The following chart shows that as consequence also the outlet water temperature is predicted with a good accuracy. Its average error results 6,03 % and it becomes 4,07% by neglecting the cases where the temperature differences between inlet air and outlet water becomes lower than 1°C.

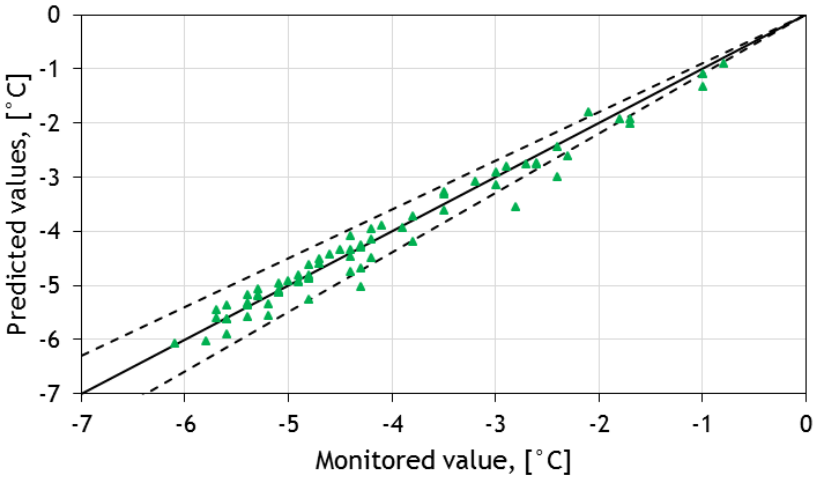

Figure 3.33 Outlet water temperature comparison between predicted and monitored values

4 Parametric analysis

The aim of this analysis is to investigate the behavior of the model under different ambient and working boundary conditions. The considered parameters are the inlet air temperature $T_{a,in}$ and relative humidity $\varphi_{a,in}$, the inlet water temperature $T_{w,in}$ and the set-point temperature difference between inlet air and outlet water ΔT_{set}. To understand the influences of the considered parameters on the heat transfer capacity, each parameter is varied along its typically winter range while the rest of other conditions are maintained in their reference state. The influence of these parameters under cooling conditions has not been take into account.

The investigated geometry is based on the datasheet of the SorTech AG RCS 08 heat exchanger reported in appendix A. The coefficients for the induced volumetric flow rate are set according to Bettoni & D'Antoni work [27]. The coefficients presented in the paragraph 2.7 are used for the calculation of the fan electrical power consumption.

The reference case for the simulations is based on the average conditions of the available monitoring data. These values represent the typical operating conditions during the heating mode. Furthermore, the mass concentration γ of the propylene glycol mixed in the water stream is maintained at the constant rate of 40 % for all the simulations.

The simulations are run for fan-working mode 2 and 3. No upper and lower limits are imposed to the relative fan rotational speed y_{fan}, which can vary between 0 % and 100 %.

The reference conditions are resumed in the next table. This table also reports the simulation results for the reference conditions:

Table 4.1 Reference conditions: simulation inputs and results

Inlet water temperature	$T_{w,in}$	-7,5	°C
Inlet air temperature (dry-bulb)	$T_{a,in}$	-2,5	°C
Inlet absolute humidity	$x_{a,in}$	1,835	g_v/kg_a
Inlet relative humidity	$\varphi_{a,in}$	0,6	% (base 1)
Inlet air pressure	$p_{a,in}$	1,01325	Bar
Relative rotational speed set-point	$y_{fan,set}$	-	% (base 1)
Outlet water set-point temperature	$T_{w,set}$	-	°C
Air–water set-point temperature difference	ΔT_{set}	1,5	°C
Outlet water temperature	$T_{w,out}$	-4,00	°C
Outlet air temperature (dry-bulb)	$T_{a,out}$	-4,29	°C
Outlet absolute humidity	$x_{a,out}$	1,835	g_v/kg_a
Outlet relative humidity	$\varphi_{a,out}$	69,78	% (base 1)
Total heat transfer rate	$\dot{Q}_{tot}$	4309	W
Total latent heat transfer rate	$\dot{Q}_{L,tot}$	0	W
Total sensible heat transfer rate	$\dot{Q}_{S,tot}$	4309	W

Water mass flow rate	$\dot{m}_w$	1200	kg/h
Air mass flow rate	$\dot{m}_a$	8608	kg/h
Fan-working mode		2	
Relative fan rotational speed	y_{fan}	0,183	% (base 1)
Electrical power consumption	$\dot{W}_{el,fan}$	39	W

Figures 4.1 and 4.2 reports sensible $\dot{Q}_S$ and latent $\dot{Q}_L$ heat transfer rates, cumulative total heat transfer rate $\dot{Q}_{tot}$ and the local temperature for air and water at each row.

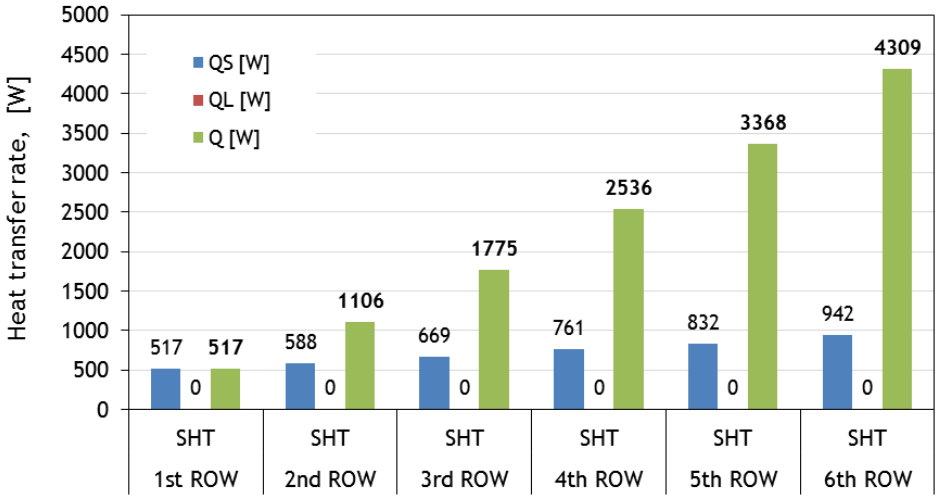

Figure 4.1 Reference case: Row-sensible, row-latent and total heat transfer rates

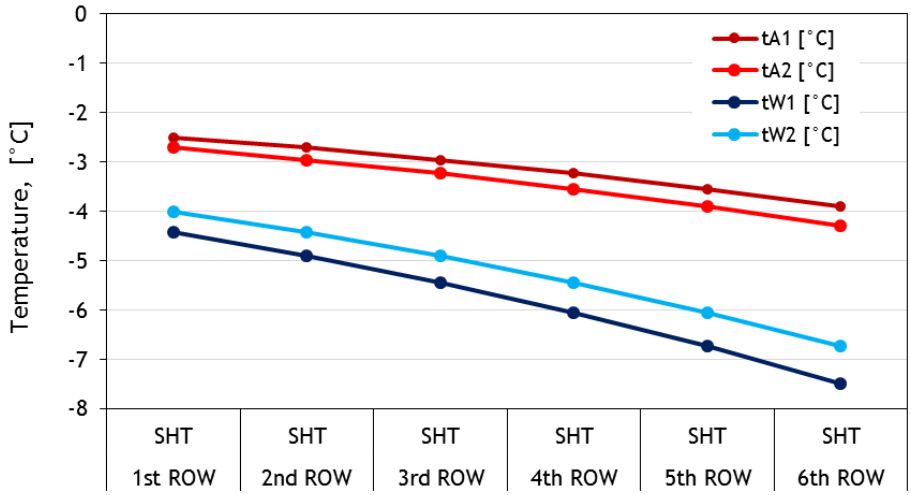

Figure 4.2 Reference case: Row-inlet and row-outlet temperatures for air and water

Under these reference conditions, the air stream does not get dehumidified and only sensible heat transfer occurs. In fact, the interface temperature between air and heat exchanger wall is well above the dew-point temperature as shown in the next figure:

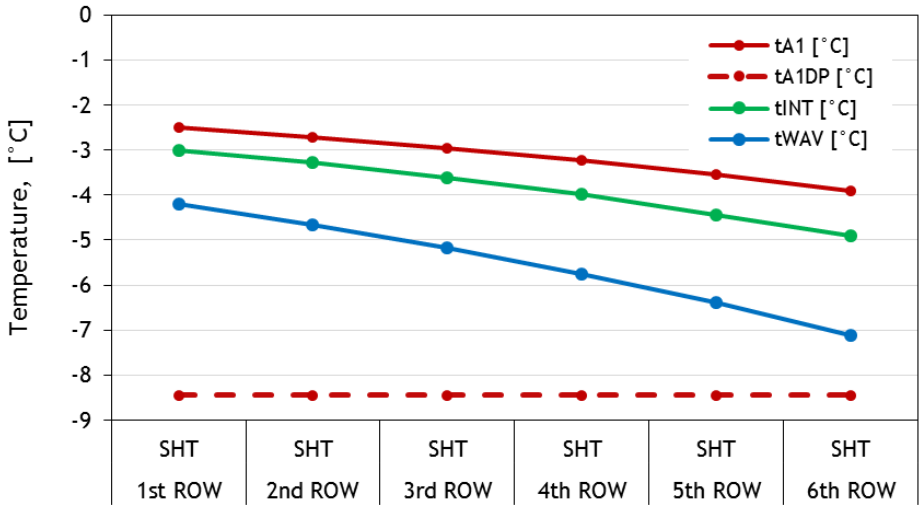

Figure 4.3 Reference case: Inlet air dry bulb air, dew-point, interface and average water temperatures for each row

To investigate the heat transfer prediction under cooling conditions, a single time-step simulation is run under design conditions. For this simulation, the fan-working mode is set to 3 and the set-point relative fan speed y_{set} is associated to the volumetric flow rate $\dot{V}_{fan}$ reported in the brochure. Because glycol mass concentration γ is not reported in the brochure, it is assumed that water with no additional glycol (γ = 0) is flowing. Furthermore, it has been assumed an inlet relative humidity $\varphi_{a,in}$ is equal to 60%.

Table 4.2 Brochure condition: simulation inputs and results

Inlet water temperature	$T_{w,in}$	31,8	°C
Inlet air temperature (dry-bulb)	$T_{a,in}$	24,5	°C
Inlet absolute humidity	$x_{a,in}$	11,539	g_v/kg_a
Inlet relative humidity	$\varphi_{a,in}$	0,6	% (base 1)
Inlet air pressure	$p_{a,in}$	1,01325	Bar
Relative rotational speed set-point	$y_{fan,set}$	0,642	% (base 1)
Outlet water set-point temperature	$T_{w,set}$	-	°C
Inlet air – outlet water set-point temperature difference	ΔT_{set}	1,5	°C
Fan-working mode		3	
Outlet water temperature	$T_{w,out}$	26,93	°C
Outlet air temperature (dry-bulb)	$T_{a,out}$	29,34	°C
Outlet absolute humidity	$x_{a,out}$	11,539	g_v/kg_a
Outlet relative humidity	$\varphi_{a,out}$	45,15	% (base 1)
Total heat transfer rate	$\dot{Q}_{tot}$	-20918	W

Total latent heat transfer rate	$\dot{Q}_{L,tot}$	0	W
Total sensible heat transfer rate	$\dot{Q}_{S,tot}$	-20918	W
Water mass flow rate	$\dot{m}_w$	3684	kg/h
Air mass flow rate	$\dot{m}_a$	15301	kg/h
Electrical power consumption	$\dot{W}_{el,fan}$	598	W

The local heat transfer sensible and heat transfer rates values are reported in figure 4.4 whereas figure 4.5 shows the trends of the predicted air and water temperature.

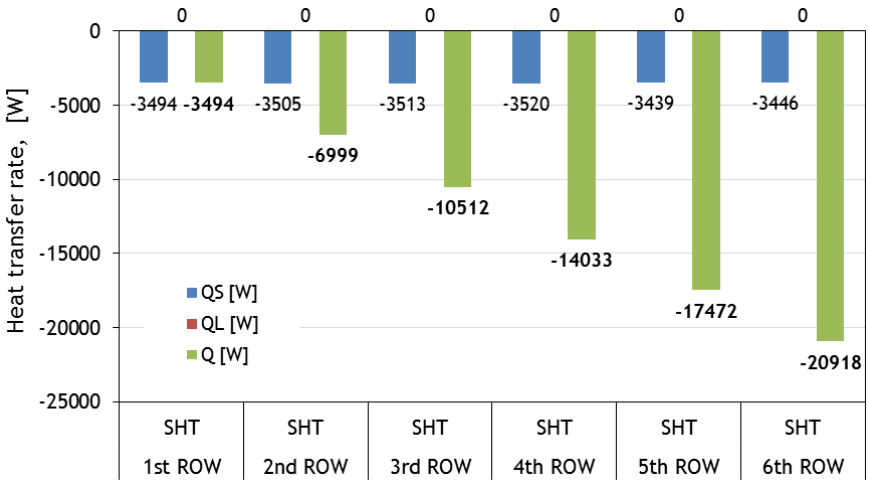

Figure 4.4 Brochure case: Row-sensible, row-latent and total heat transfer rates

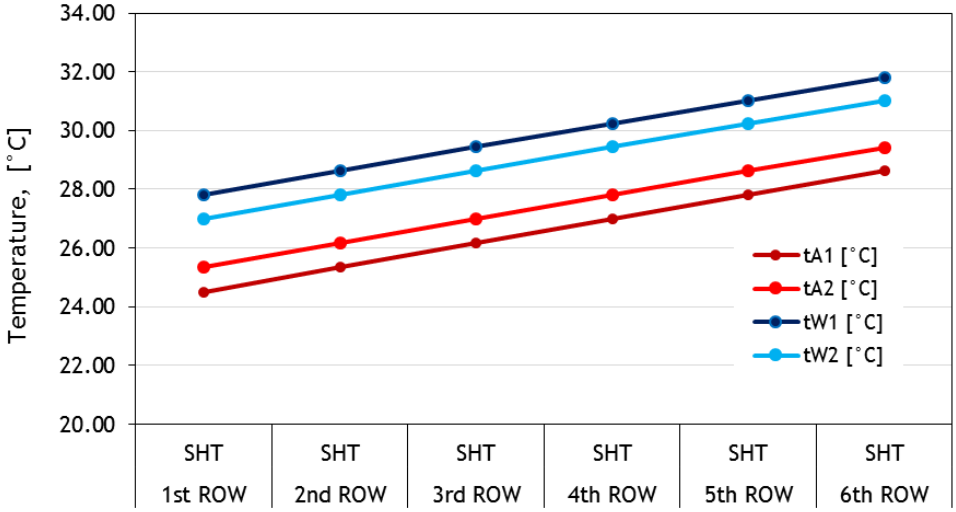

Figure 4.5 Brochure case: Row-inlet and row-outlet temperature for air and water

It can be noted that the temperature differences at each row are almost constant. That reflects a balance in the heat transfer characteristics, typical of design conditions. This balance can also be recognize in the heat transfer rates distribution as reported in figure 4.4 .

The predicted outlet water temperature $T_{w,out}$ results slightly lower than the value reported in the brochure. This underestimation can be caused by the uncertainty on the glycol mass concentration which directly affects the specific heat $c_{p,w}$ of the water mixture. Consequentially, the predicted water temperature difference is not equal to the reported value. However, the relative difference between predicted and reported values of $T_{w,out}$ is lower than 0,025 %. Thus, it can be consider satisfying results.

4.1 Inlet air and water temperatures influences at low humidity

The first investigated parameter under heating conditions is the inlet air temperature $T_{a,in}$. Simulations are run for a low value of humidity $\varphi_{a,in}$ (60 %) and variable inlet temperature values between -7,5 °C (inlet water temperature) and 15°C every 2,5°C.

Sensible $\dot{Q}_{S,tot}$ and latent $\dot{Q}_{L,tot}$ heat transfer rates for the different cases are reported in the next chart. The chart also reports the resulting trend of the relative fan rotational speed y_{fan}.

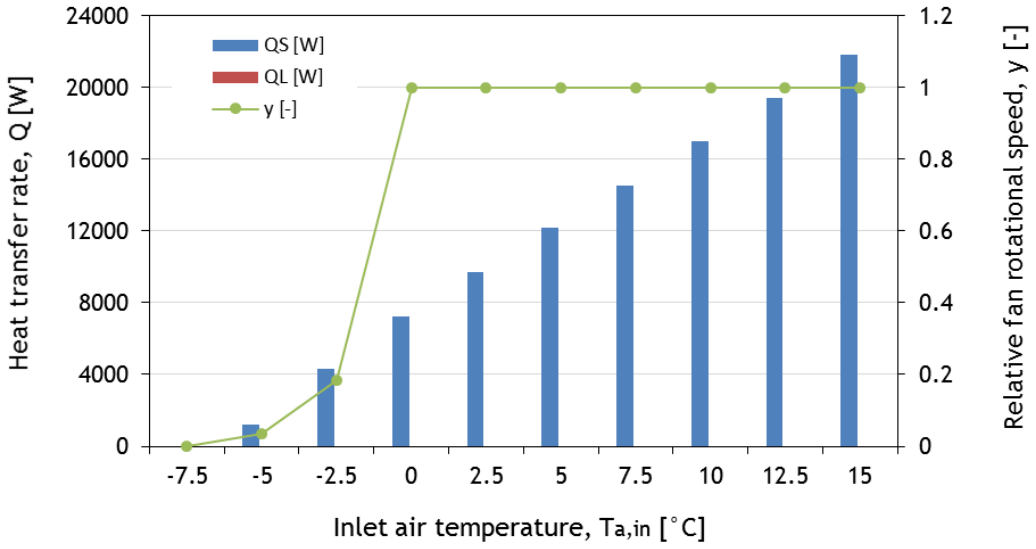

Figure 4.6 Sensible and latent heat transfer rates, relative fan rotational speed for different inlet air temperatures and low relative humidity

In the previous figure, it can be noted that under those conditions only sensible heat transfer occurs. An increment in the inlet air temperature $T_{a,in}$ with a fixed value of the inlet water temperature $T_{w,in}$ corresponds to increase the heat rate potentially transferred from the air stream to the water. In fact, under dry conditions, the heat transfer potential is directly proportional to the inlet temperature difference between air and water.

As a results of the fans working in mode 2, increasing $T_{a,in}$ corresponds to an increase in the outlet water reference temperature $T_{w,ref}$ and the required heat transfer rate $\dot{Q}_{ref}$ This can be seen from the relative fan rotational speed y_{fan} trend, when the outlet water reference temperature $T_{w,ref}$ becomes higher (i.e. over 0°C) due the augmentation of $T_{a,in}$, the heat exchanger cannot supply the adequate heat transfer rate and the fan system works at its maximal capacity (y_{fan} = 1).

The next parameter under investigation is the inlet water temperature $T_{w,in}$. Its variation corresponds to a variation of the inlet-outlet reference water temperature difference and, consequentially, of the required $\dot{Q}_{ref}$. As mentioned before, the heat transfer potential will vary with it, due the changing in the inlet temperature difference between air and water streams. The inlet water temperature $T_{w,in}$ has been varied from -20°C to -2,5°C with steps of 2,5 °C.

The trends of sensible and latent heat transfer rates, like the relative fan rotational speeds are reported in the next figure:

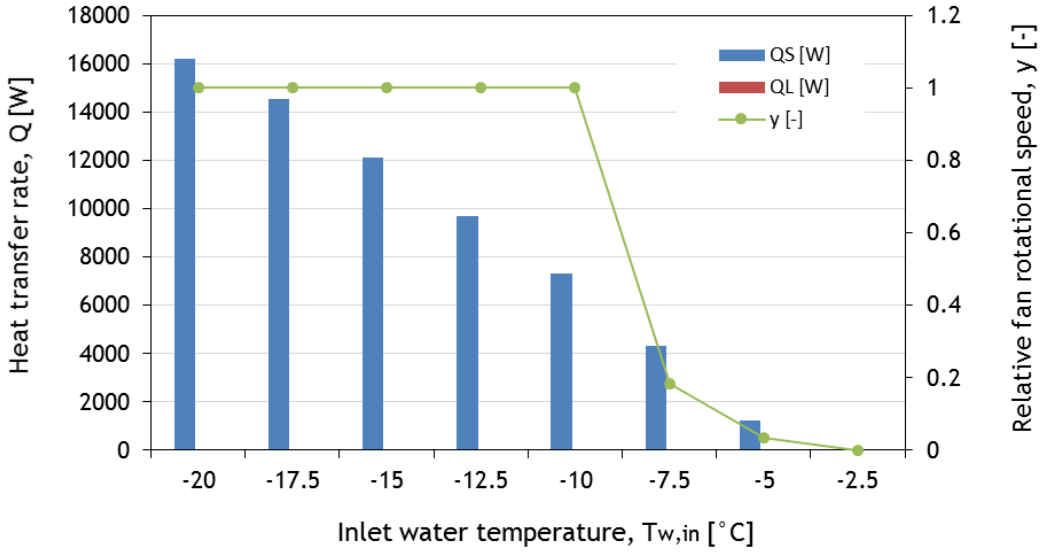

Figure 4.7 Sensible and latent heat transfer rates, relative fan rotational speed for different inlet water temperatures

Also in these cases, only sensible heat is transferred. This can be seen in the chart of figure 4.7, the heat exchanger supplies (y_{fan} < 1) the required heat transfer rate $\dot{Q}_{ref}$ only when the inlet-outlet reference water temperature difference is low (three last simulations).

4.2 Set-point temperature difference influence

At this point, it is appropriate to investigate the model behavior for different values of the set-point temperature difference ΔT_{set}. This variation range corresponds to change the values of the outlet water temperature $T_{w,ref}$. This temperature is usually a function of the water mass flow rate $\dot{m}_w$ and the required heat transfer rate $\dot{Q}_{ref}$, which depend (directly or indirectly) on the rest of the heat pump system.

During the simulations, the water reference temperature $T_{w,ref}$ is varied from the inlet air temperature value $T_{a,in}$ (-2,5°C) to the inlet water temperature value $T_{w,in}$ (-7,5°C) each 0,5 °C. This variation corresponds to a set-point temperature difference ΔT_{set} that goes from 0°C to 5°C.

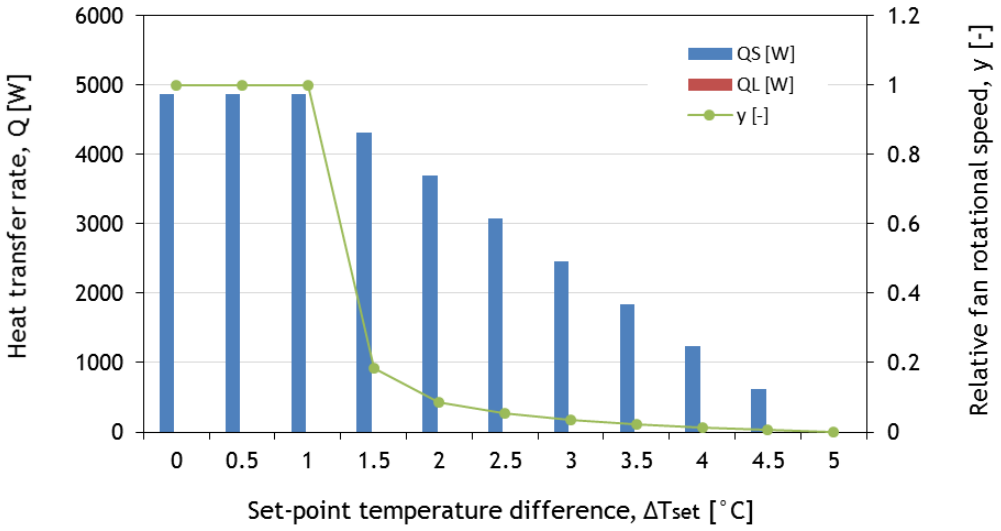

Figure 4.8 Sensible and latent heat transfer rates, relative fan rotational speed for different air-water temperature differences

As expected, the simulations show that the water stream is capable of reaching the outlet water temperature $T_{w,ref}$ (y_{fan} < 1) only for values of ΔT_{set} higher than 1°C. In other words, when the required heat transfer rate $\dot{Q}_{ref}$ decreases under the maximal thermal capacity of the heat exchanger under reference conditions (slightly over 4800 W). This also corresponds to having an outlet water temperature $T_{w,ref}$ close enough to the inlet water temperature $T_{w,in}$. Figure 4.8 shows that the relative fan rotational speed y_{fan} decreases until the limit condition when the outlet water temperature $T_{w,ref}$ coincides with the inlet water temperature $T_{w,in}$ and no heat transfer is required.

To investigate the model behavior when a frost layer is present on the row surface, the last set of simulations is repeated assuming that an initial frost layer is present on the heat exchanger. For each case, an initial 6 hour simulation is run under a high level of humidity ($\varphi_{a,in}$ 90 %). This initial simulation assures the presence of a frost layer on half of the heat exchanger (last three rows). After this 6 hours simulation, a single time step simulation is run under reference conditions and variable set-point temperature difference ΔT_{set}. The results are compared with the unfrosted condition, reported in figure 4.8 .

The following figure shows the comparison between frosted and unfrosted conditions. It is clear that under frosted conditions, the heat exchanger performance are limited with respect to the results of the previous set of simulations. This limitations are mainly due to the additional thermal resistance of the frost layer and to its blockage effect on the air flow channel.

As can be noted, for the first values of the set-point temperature difference ΔT_{set}, (where the heat exchanger is not capable of providing the necessary air mass flow rate $\dot{m}_a$) the total heat transfer $\dot{Q}_{tot}$ under frost conditions results reduced. The value of the maximal reachable heat transfer rate decreased around 4600 W. Furthermore, when the water stream can reach its outlet reference temperature $T_{w,ref}$, the necessary fan rotational speed y_{fan} is smaller without frost on the heat exchanger. This tendency is clearly visible

at the highest values of the heat transfer rate and tends to disappear when the heat transfer rate becomes smaller.

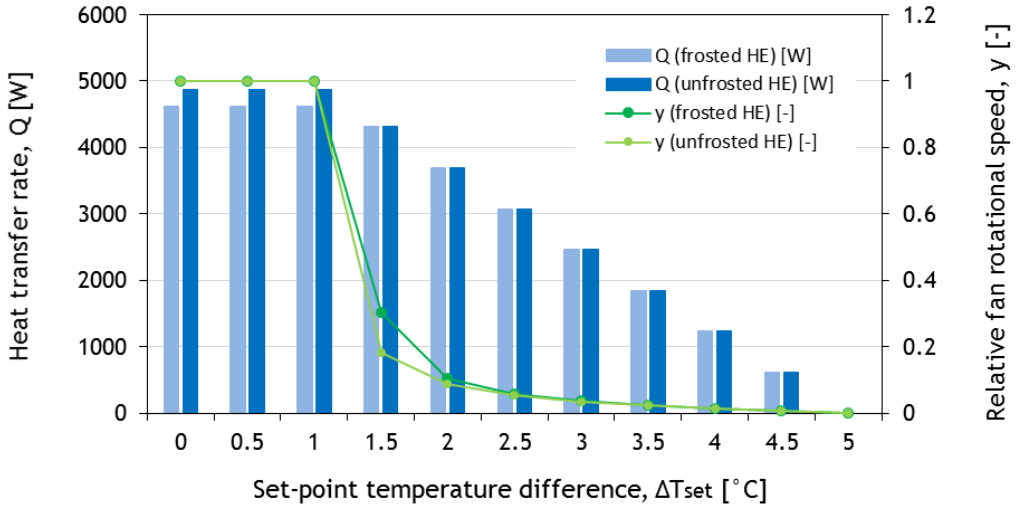

Figure 4.9 Sensible and latent heat transfer rates, relative fan rotational speed of a frosted heat exchagner for different air-water temperature difference

4.3 Inlet air humidity influence

Since all the previous simulated cases involve sensible heat transfer only, it is interesting to investigate the model behavior when sensible and latent heat transfer occur. Therefore, the inlet air relative humidity $\varphi_{a,in}$ is increased from 60 % to 100 % with steps of 5%.

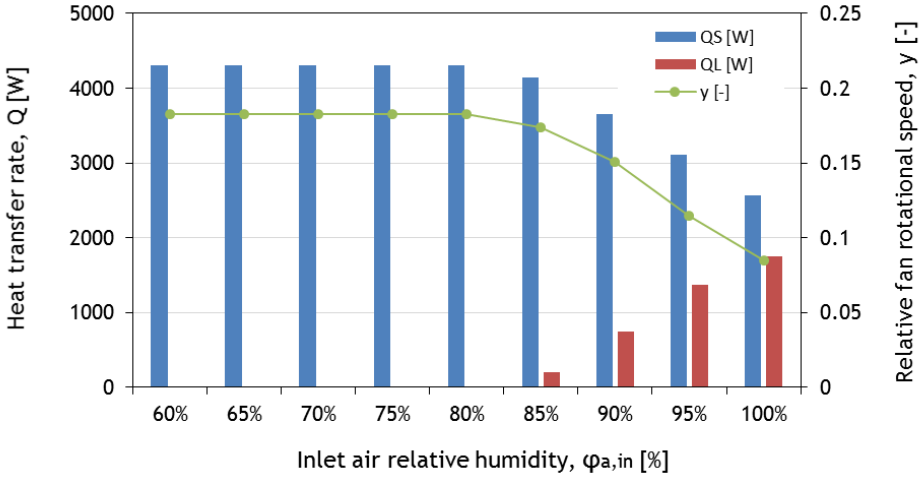

Figure 4.10 Sensible and latent heat transfer rates, relative fan rotational speed for different inlet air relative humidity

As can be seen in figure 4.10, condensing phenomena occurs on the external surface only at the highest levels of the inlet air humidity (over 80 %). This can be justified by noting

that the simulated conditions are well below the design point. In fact, the SorTech AG RCS 08 heat exchanger is designed for heat transfer rate $\dot{Q}_w$ around 21 kW and water mass flow rate $\dot{m}_w$ around 3600 kg/h. Consequentially, the required air mass flow rate is relatively low. The fan speed y_{fan} values are always under 20 %. Hence, the low flowing air speed values involves a reduced external convection and smaller difference between the air inlet $T_{a,in}$ and the interface T_{int} temperatures. The interface T_{int} temperature results close to the inlet air temperature (see figure 4.12). In order to obtain condensing condition, the relative humidity $\varphi_{a,in}$ must be increased to high values so that the dew-point temperature $T_{a,dp}$ results particularly close to the dry-bulb value $T_{a,in}$.

Moreover, as the relative humidity $\varphi_{a,in}$ increases, the latent heat transfer rate $\dot{Q}_{L,tot}$ becomes greater, whereas the total heat transfer rate supplied by the air stream $\dot{Q}_{tot}$ remains constant. Simultaneously the sensible heat fraction $\dot{Q}_{S,tot}$ becomes smaller and the required fan speed y_{fan} decreases with it. The increment in the latent heat $\dot{Q}_{L,tot}$ with the inlet humidity $\varphi_{a,in}$, reflects the enhancement of the vapour content $x_{a,in}$ in the air stream and of its enthalpy transfer potential as consequence. Furthermore, it can be noted that the only the latent heat potential is increased with a higher level of inlet air humidity $\varphi_{a,in}$. In fact, since the air temperature $T_{a,in}$ does not change, the sensible heat potentially transferred remains constant.

The decrease of the fan rotational speed y_{fan} involves a reduction of the fan electrical power that goes from nearly 5% (for $\varphi_{a,in}$ at 85 %) to 45% (for $\varphi_{a,in}$ at 100 %).

To show, the local heat transfer rates, temperatures and air absolute humidity trends, the results of a single simulation are reported in the following chart. The chosen case is the simulation for a relative humidity value equal to 90 %.

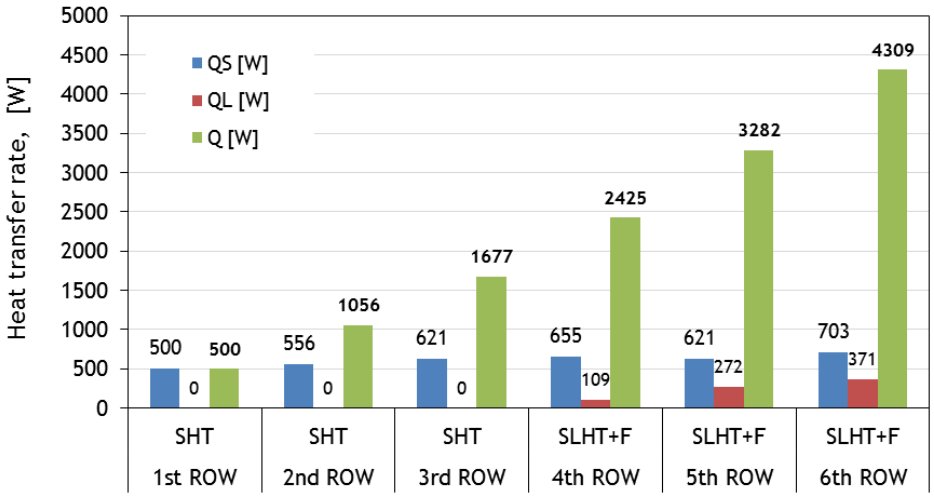

Figure 4.11 Inlet relative humidity 90 %: Row-sensible, row-latent and total heat transfer rates

As showed in the next chart, on the second half of the heat exchanger the row-interface temperatures T_{int} are below the dew-point temperature $T_{a,dp}$. As consequence, simultaneous sensible and latent heat transfer occurs and the air stream is dehumidified.

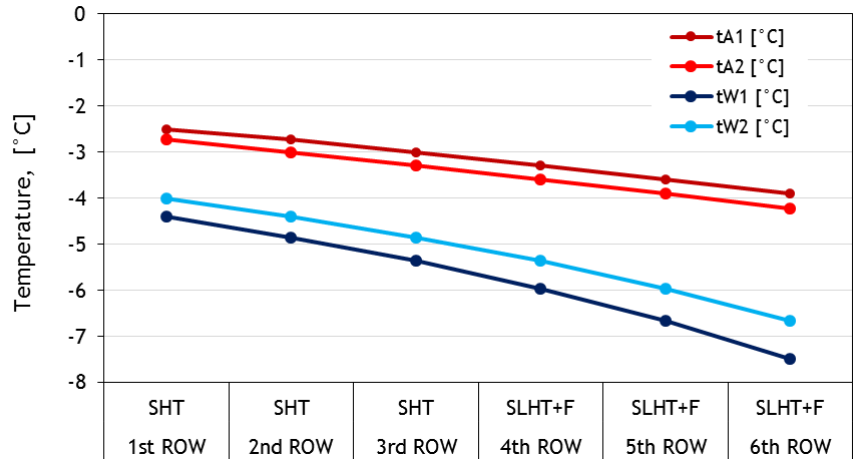

Figure 4.12 Inlet relative humidity 90 %: Row-inlet and row-outlet temperature for air and water

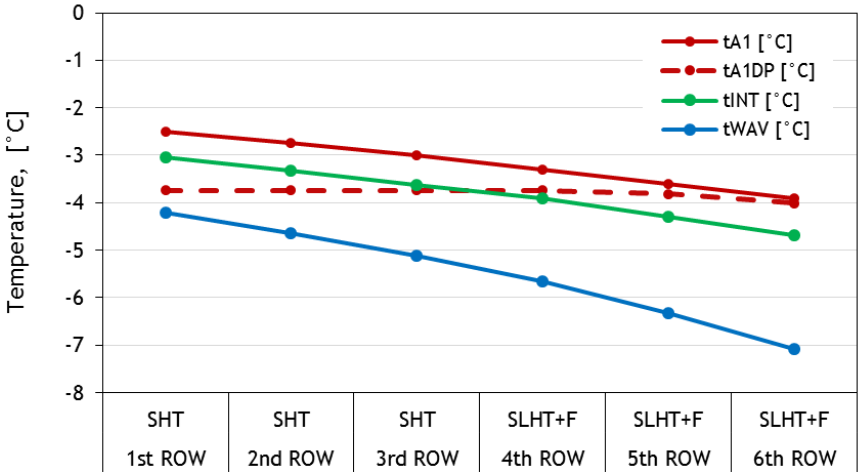

Figure 4.13 Inlet relative humidity 90 %: air dry bulb air, dew-point, interface and average water temperatures at each row

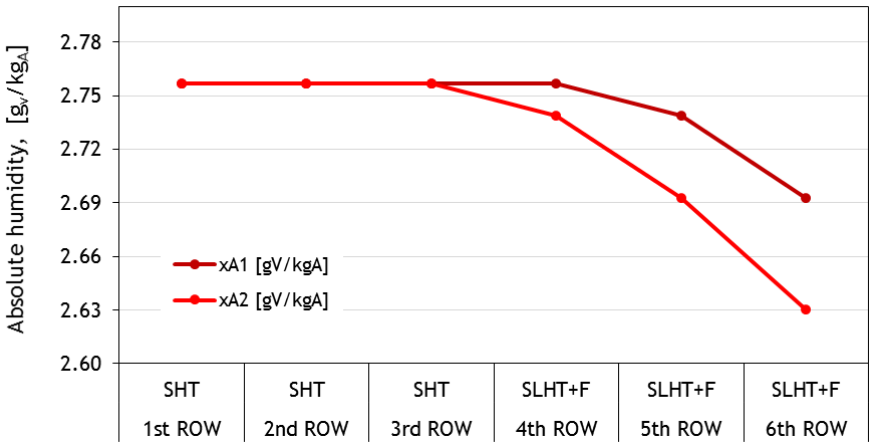

Figure 4.14 Inlet relative humidity 90 %: Row-inlet and row-outlet air absloute humidty

From figure 4.14 it is clear that the row-interface temperature T_{int} is always below the air frost point temperature (around 0°C). Hence, when the vapour contained in the air stream condenses, it freezes and frost formation occurs. The following chart reports the frost layer conditions at each row at the end of the simulated time-step.

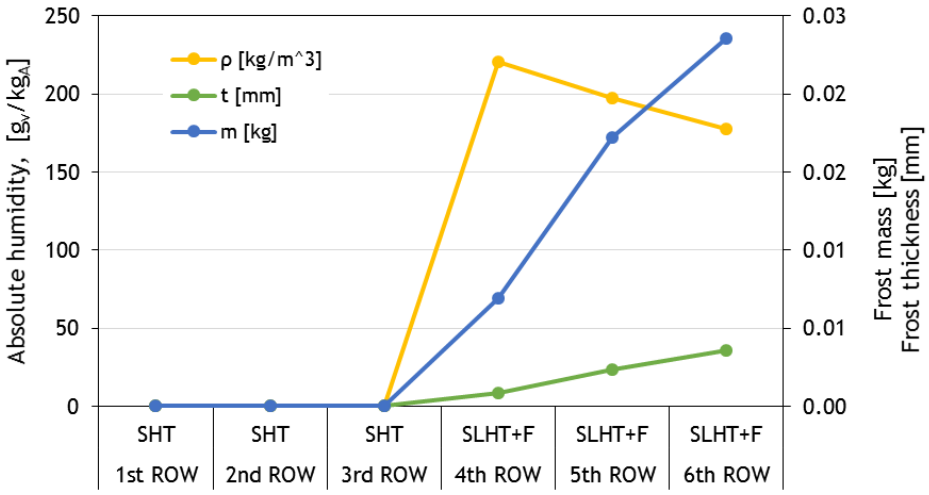

Figure 4.15 Frost mass, thickness and density at each row

By comparing the row-heat transfer rates and the absolute humidity trends for different values of the inlet humidity, it can be noted that as this last parameter increases, it increases the number of row where condensation occurs. This involves two aspect: the total latent heat transfer increase whereas the row-latent heat transfer potential decrease due the drop of the inlet absolute humidity at each row. This last effect can be noted in figure 4.17 for the last two rows when the humidity change from 90 to 100%

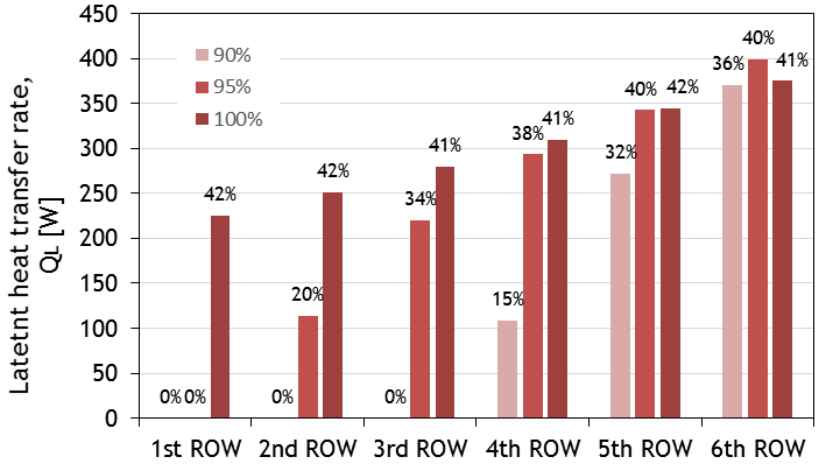

Figure 4.16 Row-latent and percentage with respect to the total heat tranfer rate for different values of the inlet relative humidity

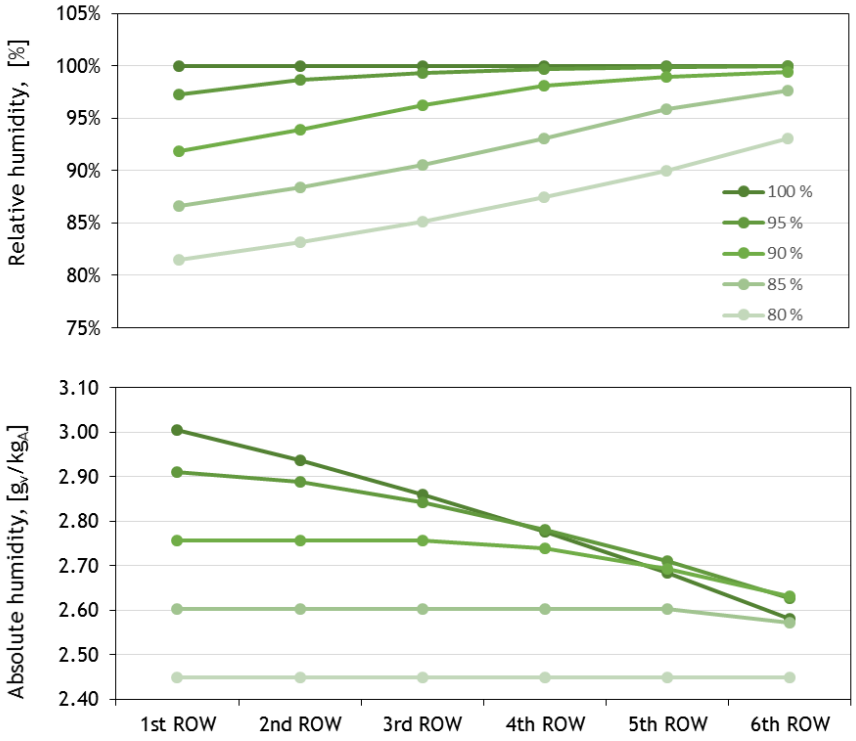

Figure 4.17 Row-outlet absolute and relative humidity trends for different values of the inlet relative humidity

4.4 Inlet air temperature influence at high humidity

Since the inlet air temperature $T_{a,in}$ in the previous simulation is set at the constant value of -2,5°C, the interface between air and heat exchanger wall results always under the frost point. Hence, latent heat transfer in this conditions is always caused by water vapour sublimation on the row-surface.

In order to investigates, the model behaviour when the vapour condenses into liquid water, the first set of simulation (variable inlet air temperature) is repeated, adopting an higher value of inlet air humidity $\varphi_{a,in}$. To assure the involving of latent heat transfer, a value of 90 % and 95 % for the inlet air relative humidity $\varphi_{a,in}$ are chosen. This analysis is particular indicated to understand the effect on the latent heat transfer under different ambient boundary condition as the inlet air humidity $\varphi_{a,in}$ and temperature $T_{a,in}$. As the inlet air temperature $T_{a,in}$ increases, the total heat transfer rate $\dot{Q}_{tot}$ becomes greater.

For a constant value of humidity, the increase in the latent heat transfer $\dot{Q}_{L,tot}$ results super linear with respect to the total heat transfer rate $\dot{Q}_{tot}$. In fact increasing the inlet air temperature corresponded not only to an increase in the sensible heat transfer potential but also to the increase of the latent heat transfer potential. In fact as can be seen in the following charts, the ratio between latent and total heat transfer rates increase with the temperature $T_{a,in}$. This is due to the increment in the vapour content (quantifies by the air absolute humidity $x_{a,in}$) for constant relative humidity $\varphi_{a,in}$ as the inlet air temperature $T_{a,in}$ increase.

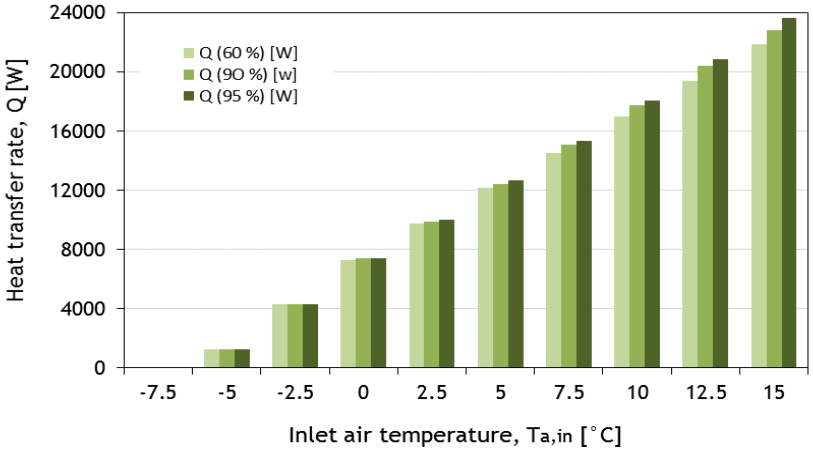

Figure 4.18 Total heat transfer rates comparison for different inlet air temperatures and different rates of relative humidity

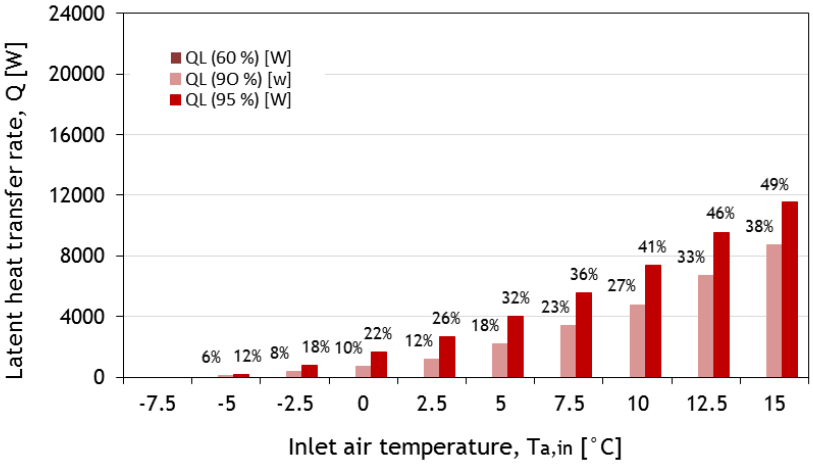

Figure 4.19 Latent heat transfer rates comparison for different inlet air temperatures and different levels of relative humidity

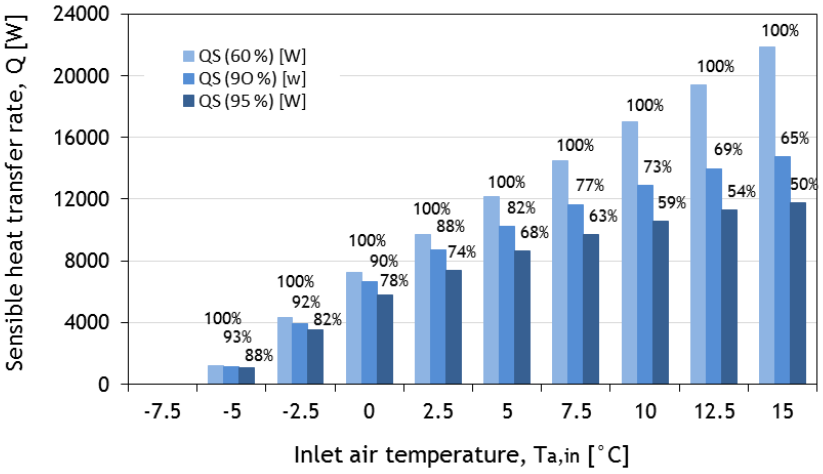

Figure 4.20 Sensible heat transfer rates and relative fan rotational speed comparison for different inlet air temperatures and different levels of relative humidity

By comparing the last results under dehumidifying condition with that obtained for only sensible heat transfer (at $\varphi_{a,in}$ 60 %), it results clear the decrease of the required sensible heat transfer rate $\dot{Q}_{S,tot}$ and of the required relative fan speed y_{fan} as consequence, when latent heat transfer increase.

From the previous charts it can be observed that under dehumidifying condition as the inlet air $T_{a,in}$ increases its value, the augmentation of the total heat transfer rate $\dot{Q}_{tot}$ is mainly due to the increase of its latent fraction $\dot{Q}_{L,tot}$. Whereas, the sensible heat transfer rate $\dot{Q}_{S,tot}$ after an initial reduction tends to become constant and to reduce its percentage with respect to the total heat transfer rate $\dot{Q}_{tot}$.

To analyze the model behavior with respect to the frost formation and accumulation phenomena, an additional set of simulation are conducted: for inlet relative humidity $\varphi_{a,in}$ between 80 % and 92,5 % the air inlet temperature is varied between -10°C and 5°C. Furthermore, the difference between the inlet air and the inlet water temperature is maintained constant and equal to 5°C. In order to verify the frost accumulation prediction the simulation time is increased from 3 minutes (single time-step) to 6 hours.

The resulting accumulated frost mass during the different simulation conditions is reported in figure 4.21. The accumulated frost mass increase with the inlet relative humidity $\varphi_{a,in}$: this reflects the increment of the water vapour containment in the moist air. Moreover, at highest humidity $\varphi_{a,in}$ level, frost formation occurs on more rows than at the lowest value. This can be justified with higher value of the dew-point temperature $T_{a,dp}$ with higher value of the inlet humidity $\varphi_{a,in}$. Hence, it results easier to work under sublimating condition for the similar interface temperature T_{int}. For the same reason, the inlet air temperature $T_{a,in}$ corresponding to the peak of the accumulated frost mass increases with the inlet relative humidity $\varphi_{a,in}$ value.

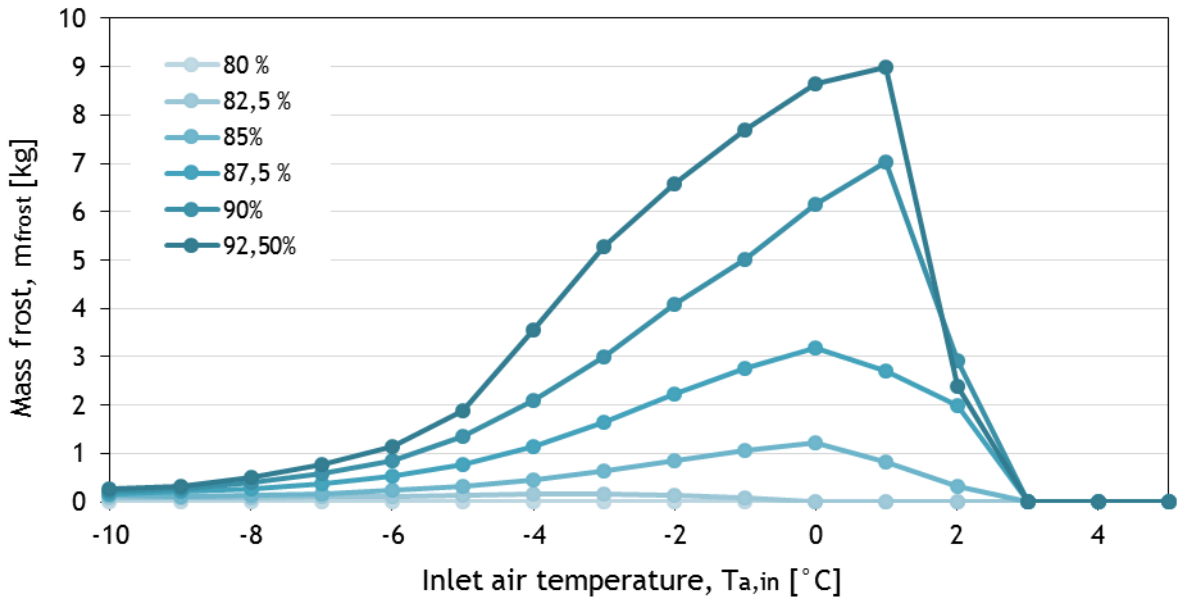

Figure 4.21 Accumulated frost mass for different inlet relative humidity and variable inlet air temperature

4.5 Ambient and working conditions influence

To better understand the influences of the ambient boundary conditions on the heat exchanger performance under condensing and frosting condition a last set of simulations is run. The aim of this analysis is to investigate the conditions under which the total heat transfer rate is enhanced due to the combined latent and sensible heat transfer. Moreover it also useful to evaluate under which conditions frost formation occurs.

Referring to the reference condition reported in table 4.1, simulations are run for different values of the inlet water temperature $T_{w,in}$ by changing the inlet air temperature $T_{a,in}$ and humidity $\varphi_{a,in}$. For these simulations, the fan rotational speed is maintained constant: its relative value y_{fan} is set to 30 % of the maximal allowed value. The inlet air relative humidity $\varphi_{a,in}$ is varied from 70 % to 90 % each 5 %, whereas the air inlet temperature $T_{a,in}$ is varied from -5 °C to 10 °C with step of 2,5°C for each humidity level $\varphi_{a,in}$. The resulting combinations of the different air inlet condition are investigated by varying the inlet water temperature $T_{w,in}$ each 2,5 °C in the range between -7,5°C and 5°C. These variability ranges are consider being a good representation of the ambient and working conditions during the heating season.

The analysis conducts to the graphical representations of the total heat transfer rate $\dot{Q}_{tot}$, the ratio between latent and total heat transfer rates $\dot{Q}_{L,tot}/\dot{Q}_{tot}$.

The charts reported in the next pages confirm that the total and latent heat transfer trends reported in the previous paragraph: an increase in the difference between the inlet temperature of water $T_{w,in}$ and air $T_{a,in}$ corresponds to an enhancement of the total heat transfer rate $\dot{Q}_{tot}$. Furthermore, as the humidity $\varphi_{a,in}$ grows, the latent heat $\dot{Q}_{L,tot}$ is increased and the total heat with it $\dot{Q}_{tot}$.

Under condensing condition increasing the relative humidity $\varphi_{a,in}$ causes and increase of the latent heat transfer. By changing the humidity from 70% to 90% at maximal inlet temperature differences ($T_{a,in}$ = 10°C and $T_{w,in}$ = -7.5°C) the latent heat transfer rate $\dot{Q}_{L,tot}$ increase is around 5500 W where the total heat transfer rate increase is around 1900 W. The difference of 3600 W in the sensible heat transfer rate corresponds to a decrease of the mass flow rate that the fans must provide and of their electrical consumption as consequence. This power is proportional to the sensible heat transfer rate $\dot{Q}_{S,tot}$. Hence, when simultaneous latent and sensible heat transfer occurs not only the total heat transfer is increased but also the electrical fan consumption is reduced.

It can be noted that the decrease in the inlet temperatures difference affects significantly the latent fraction with respect to the total heat transfer rate. At $T_{a,in}$ and $\varphi_{a,in}$ equal to 10°C and 90% respectively, changing the inlet water temperature $T_{w,in}$ from -5°C to 0°C, reduces the total heat transfer from around 12000 W to around 7000 W that corresponds to a relative decrease around 40%; the latent fraction reduces from 35% to the 25%, around 2400 W and a relative decrease of 64 %.

Moreover, it can be say that for given inlet air condition $\varphi_{a,in}$ and $T_{a,in}$, to encounter condensation phenomenon it necessary to decrease the surface temperature. To cause this decrease the inlet water temperature $T_{w,in}$ must be diminished. For decreased values of inlet air temperature $T_{a,in}$, condensation start at lower inlet water temperature $T_{w,in}$. Once condensation begin, further decrease of the inlet water temperature increase the latent heat transfer rate $\dot{Q}_{L,tot}$ For the simulated condition the latent heat transfer does not achieve the 40 % of the total heat transfer also for temperature difference far above the usual working condition.

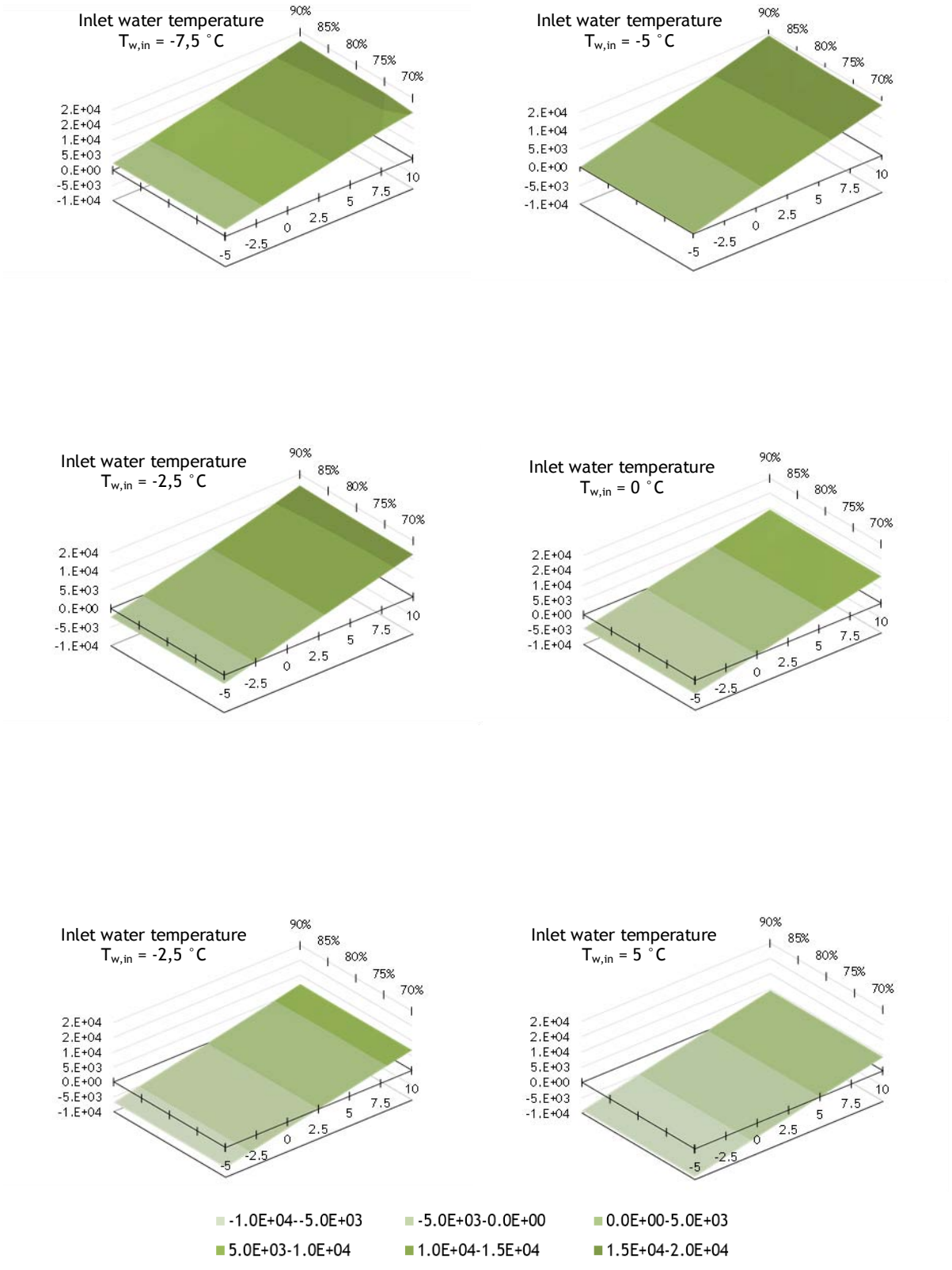

Figure 4.22 Total heat transfer rate for different inlet water temperatures by varying the air inlet conditions

Figure 4.23 Percentage of latent heat transfer rate with respect to the total heat tranfer rate for different inlet water temperatures by varying the air inlet conditions

As mentioned before, a decrease of the inlet water temperature $T_{w,in}$ cause an enhancement of the latent heat transfer rate. At high level of humidity $\varphi_{a,in}$ when the air temperature is around 0°C, frosting phenomena appear on the heat transfer surface. For

further diminishment of the inlet water temperature $T_{w,in}$, frost begins to form for a wider range of humidity $\varphi_{a,in}$ and air temperature $T_{a,in}$ as show in the next figure.

At lower temperature the in addition to have a wide range of air condition that involve frosting phenomena, the quantity of accumulated frost is increase. As the time past the accumulation of frost lead to a decrease of the heat transfer performance that cannot be balance by the enhancement on the heat transfer condition under condensing condition. Hence, this condition are to avoid

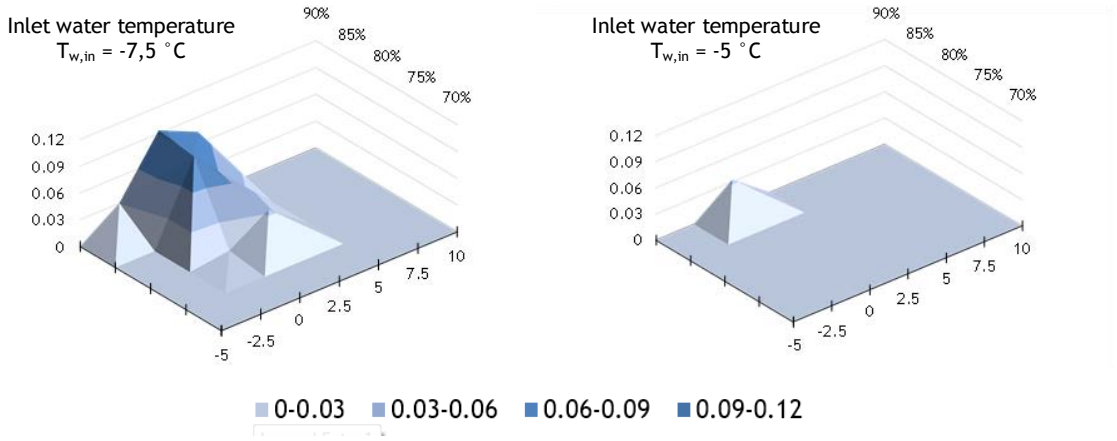

Figure 4.24 Accumulated mass frost for different inlet water temperatures by varying the air inlet conditions

4.6 Parametric analysis conclusion

As results from the previous parametric analysis, it is not easy to define the condition under which condensing and frosting phenomena occurs. Condensation occurs with the simultaneous combination of several condition that affect air dew-point $T_{a,dp}$ and external surface T_{int} temperatures. These temperatures are influenced by geometrical and thermal characteristics of the heat exchanger, by the fan system behavior, as well as by ambient and working boundary condition. It results essential to dispose of a valid model that can help in the prediction of those combinations.

For the SorTech AG RCS 08 the previous parametric analysis leads to the definition of some limit conditions where condensation/sublimation occurs. In the encountered water working-temperature range (between -8,5°C and -4,5°C) condensation/sublimation occurs only at highest level of air humidity $\varphi_{a,in}$. Typically condensing phenomenon appears on the last row where water reaches the lowest temperature when the inlet air relative humidity is over 70%.

As excepted, under condensing/sublimating condition the heat transfer capacity of the heat exchanger is increased. In specific, the total heat transfer rate can be exchanged with lower electrical fan consumption. It is also clear that, even at this high levels of humidity, the low temperature of the outdoor air during winter involves pour vapour contentment $x_{a,in}$, (lower than 10 g_v/kg_a). The main consequence is that for a constant fan rotational speed, the latent heat transfer rate $\dot{Q}_{L,tot}$ reaches difficulty the 20% of the total heat transfer rate $\dot{Q}_{tot}$. Moreover, the total heat transfer rate $\dot{Q}_{tot}$ is only slightly increased with respect to only sensible heat transfer condition. The decrease of the fan rotational speed y_{fan} under condensing condition involves a reduction of the fan electrical power up to 45% (for extremely humid condition $\varphi_{a,in}$ at 100 %).

Because water and air temperature are usually both below the air frost point temperature $T_{a,fp}$ (around 0 °C), latent heat transfer is often sustained by sublimation and frost formation.

The reduction of the heat exchanger performance depends greatly on the duration of the period under frosting condition. As seen, the protracting of frosting condition brings to a decline in the heat transfer capacity of the heat exchanger and to a simultaneous increase of the electrical consumption. The highest influences on the heat exchanger performance by the frost presence is associated to air temperature around the frost point and at high level of humidity, typically greater than 80 %. It must be observed that this situation does not coincides with the maximal accumulated frost mass m_{frost}. As reported in literature [75] [77] [78], in this condition, the frost layer results highly porous with low thermal conductivity.
In fact, the low surface temperature causes the rapid formation of a frost layer that present a low density (compared to that of the pure ice), causing a high insulation effect. Simultaneously, the high level of humidity continues to provide a good amount of sublimating vapour that increases the frost layer thickness. Both effects cause a drop of the heat transfer capacity.

5 Conclusion

In this thesis, the influences of the ambient and working boundary conditions on the performance of an air-to-water heat exchanger have been investigated. The focus of this work was pointed on air-source heat pump system in heating seasons.

Initially a survey of the available literature on condensation and on frost accumulation had been conducted. From this review, a physical model for coupled heat and mass transfer under transient boundary conditions has been derived. A dry cooler model developed at the Institute for Renewable Energy of the European Research Academy of Bolzano was used as starting point. The model has been significantly improved and expanded from the earlier version. Numerous modifications has been made. A row-by-row approach has been involved in order to enhance the calculation accuracy and trace the air and surface temperature locally. The water circuits were modelled and simplified to a reference geometry is introduced in order to analyze complex water circuitry. Airside heat transfer has been updated by adding mass transfer evaluation; sensible/latent heat transfer and frost accumulation models were combined. Finally, corrections and additions on the calculation correlations and algorithms are made. The resulting model has been presented as FORTRAN® routine. This routine has become the basis of a TRNSYS type that can be adopted for complex dynamic simulation.

The developed model can be applied to all air-to-water heat exchanger that present multirow-multipass overall counterflow configuration with unmixed crossflow at each row. The model is capable of computing the energy consumption of coupled heat exchanger-fan system under condensing and frosting conditions. Sensible and latent heat rates of a sized heat exchanger can be calculate for variable degree of water-vapour condensation and frost formation. Outlet water temperature and electrical fan power consumption can be calculated as well.

The so derived numerical code has been validated through monitored data of a real system installation. Thermal and electrical power calculated by the code have been compared with analogous monitored quantities. Heat transfer rate and outlet water temperature predictions are in good agreement with the monitored data. The average errors are both around 6%. The comparison of the fan rotational speed leads to a high discrepancy between predicted and monitored values. This can be justified by the fact that the temperature measurement uncertainty is really close to the amount of the measurement itself. Furthermore, the correlations used to predict the volumetric air flow and the electrical fan consumption may be imprecise in the encountered range of the fan rotational speed.

The main results of this validation is that the use of the developed model in simulations under dynamic boundary conditions allows to predict good estimations of the heat exchanger performance. This possibility can improve significantly the efficiency in the use and the control of the thermal systems, in which the heat exchanger could be installed (typically air-source heat pump). In particular, it possible to define some limit conditions under which the heat exchanger performance can be increased by condensation.

To better understand the influences of the boundary conditions that affect latent heat transfer and frost formation, a parametric analysis has been conducted on a real heat exchanger configuration. Simulations have been run to derive some quantitative

considerations on the influences of the ambient and working conditions on the heat and mass transfer capacity.

For unvaried ambient conditions, increasing the air-water temperature difference leads to increase the heat transfer capacity and to reduce the fan electrical consumption. This can be done by lowering the inlet water temperature.

Under typically winter condition it results clear that latent heat transfer only occurs at high level of relative humidity, typically over 70%. As the humidity increases, starting from the last row, the number of rows under condensing condition increased. Increasing the air temperature increased the amount of vapour that condenses on the row surfaces. Both effects lead to an augment of the latent and the total heat transfer rates at constant fan rotational speed. In the encountered water and air condition the latent to total heat transfer ratio borders on 50 % at maximum. The highest amount of saved electrical fan power under condensing condition has been reached for 100 % of inlet air humidity.

Furthermore, attention should be pay when working with high humidity and surface temperature around 0°C. In this condition, frost forms very rapidly on the row surfaces. Heat transfer capacity results decreased and fans must work at higher fan rotational speed. Independently of the water inlet temperature, the worst scenario has been encountered at relative humidity over 90% and inlet air temperature between -1°C and 1°C. The temperature at which the highest amount of accumulated frost is formed decreases by decreasing the inlet relative humidity. Simultaneously it decreases the accumulated frost mass. For relative humidity under 80 %, frosting has never been predicted. As results, when ambient temperature and humidity rise, it is better to contain the difference between water and air temperature, in order to avoid surface temperature below the frost point.

It has to be mentioned that, in order to improve the applicability of the model further improvement are possible. First at all, detailed study on the fan performance at low relative speed can reduce the discrepancy between monitored and predicted electrical consumption value. Moreover, monitoring the outlet air conditions can allow a better understand the accuracy of the model. To this end, some specific experiments under controlled ambient and work condition should be run. These experiments can lead to a validation of the latent heat transfer and frost formation under dynamic conditions. The capacity to predict frost accumulation can lead to developed new control strategies of defrosting cycle.

Because the model is capable to predict the evolution in the air condition across the heat exchanger, it can be adopted to model dehumidifying-cooling coil for air conditioning application.

6 Literature reference

[1] Incropera, F., & D. DeWitt – Introduction to heat transfer – 6th ed., John Wiley and Sons Inc. (2007)

[2] Colburn, A. P. (1933) – Trans. Am. Inst. Chem. Eng. 29, 174

[3] Chilton, T. H. & A. P. Colburn (1934) – Mass transfer (absorption) coefficients-prediction from data on heat transfer and fluid function - Ind. Eng. Chem. 26, 1183-1186

[4] Kays, W. M. & A. L. London – Compact Heat exchangers – 3rd ed., Krieger Publishing Company, Malabar (1994)

[5] ESDU 86018 - Effectiveness-NTU Relations for the Design and Performance Evaluation of Two stream Heat Exchangers – in: Engineering Science Data Unit 86018 with Amendment A, ESDU Int. plc, 92-107 London (1991)LAWSKOWSKY

[6] Laskowski, R. (2011) - The concept of a new approximate relation for exchanger heat transfer effectiveness for a cross-flow heat exchanger with unmixed waters – J. Power Techn. 91, 93–101

[7] Colburn, A. J. & O. A. Hougen (1934)– Design of cooler condensers for mixture of vapours with noncondensing gases – Ind. Eng. Chem. 26, 1178-1182

[8] Mirth, D. R. & S. Ramadhyani (1993) – Comparison of methods of modeling the air side heat transfer in chilled water cooling coils – ASHRAE Transactions 99, 285-299

[9] Vardhan, A. & P.L. Dhar (1998) – A new procedure for performance prediction of air conditioning coils – Int. J. Refrigeration 21, 77-83

[10] Wang J. & E. Hihara (2003) – Prediction of air coil performance under partially wet radial fin assembly under wet cooling conditions using equivalent dry-bulb temperature method, Int. J. Refrigeration 26, 293-301

[11] Threlkeld, J. L. – Thermal environmental engineering – Prentice-Hall Inc., New York USA (1970)

[12] Kröger, D. G. – Air Cooled heat exchangers and cooling tower: thermal-flow performance evaluation and design – PennWell Corporation, Tulsa (2004)

[13] Braun, J. E. – Methodologies for the design and control of central cooling plants – PhD thesis, University of Wisconsin, Madison USA (1988)

[14] McQuiston, F. C. (1975) – Fin efficiency with combined heat and mass transfer – ASHRAE transaction Pt.1 81, 350-355

[15] Braun, J.E., S.A Klein & T.W. Mitchell (1989)– Effectiveness models for cooling towers and cooling coil – ASHRAE Trans. 99, 164-174

[16] Kays, W.M. & M.E. Crawford – Convective heat and Mass transfer – 3rd ed., McGraw-Hill Inc., New York (1993)

[17] Hausen, H. Z. (1943) – Darstellung des Wärmeübergangs im Rohren durch verallgemeinerte Potenzbeziehungen – VDI Beih. Verfahrenstech. 4, 91

[18] Sleicher, C. A., A. S. Awad & R. H. Notter (1973) – Temperature and Eddy diffusivity profiles in NaK – Int. J. Heat and Mass Transfer 16, 1565-1575

[19] Sieder, E.N. & G. E. Tate (1936) - Heat transfer and pressure drop in liquids in tubes - Industrial and Engineering Chemistry 28, No. 12, 1429-1435

[20] Shah, R. K., & A. L. London (1978) - Laminar Flow Forced Convection in Ducts - Suppl. 1 to Advances in Heat Transfer, Academic Press, New York.

[21] Shah, R. K. and M. S. Bhatti, in S. Kakac, R. K. Shah & W. Aung, Eds – Handbook of single-phase convection heat transfer – Wiley-Interscience, New York (1987)

[22] Necati Özışık, M. - Heat transfer: a basic approach – McGraw-Hill Inc., New York (1985)

[23] Bonacina, C., A. Cavallini & L. Mattarolo – Trasmissione del calore – 3a ed., CLEUP Editore, Padova (1992)

[24] Winterton, R. H. S. (1998) - Where did the Dittus and Boelter equation come from? – Int. J. Heat and Mass Transfer 41, 809-810

[25] Gnielinski, V. (1976) – New equation for heat and mass transfer in turbulent pipe and channel flow, Int. Chem. Eng 16, 359-368

[26] Petukhov, B. S. – Heat transfer and friction in turbulent pipe flow with variable physical properties – Advances in Heat transfer 6, J. P. Hartnett & T. F. Irvine Ed., Academic Press, New York (1970)

[27] Bettoni, D. & M. D'Antoni (2012) – Type 880 Dry cooler. Mathematical description – Eurac Research, Institute for renewable energy

[28] Somerscales, E. F. C. & J. G. Knudsen – Fouling of heat Transfer equipment, Hemisphere, Washington (1980)

[29] Ma, R. S. T. & Epstein (1981) – Optimum cycles for falling rate process – Can. J. Chem. Eng. 59, 631-633

[30] Coney, J. E. R., G. W. Sheppard & E. A. M. El-Shafei (1989) – Fin performance with condensation from humid air: A numerical investigation - Int. J. Heat and Fluid Flow 10, 224-231

[31] Coney, J.E.R., H. Kazeminejad & C.G.W. Sheppard (1989b) - Dehumidification of turbulent air flow over a thick fin: An experimental study - Proceedings of the Institute of Mechanical Engineers 203, 177-188

[32] Coetzee, D. & D.G. Kröger (1986) – Analysis and measurement of contact and gap resistances in extruded bi-metallic finned tubes – Heat recovery systems 6, 503-513

[33] Elsherbini, A.I., A.M. Jacobi & P.S. Hrnjak (2003) – Experimental investigation of thermal contact resistance in a plain-fin-and-tube evaporators with collarless fins – Int. J. Refrigeration 26, 527-536

[34] Filonenko, G. K. (1954), Teploénergetika 4.

[35] Elmahdy, A. H. & R. C. Biggs (1979) - Finned tube heat exchanger: Correlation of dry surface heat transfer data – ASHRAE Transactions 85,262-273

[36] Park, Y.-G. & A. M. Jacobi - Air-side performance characteristics of round- and flat-tube heat exchangers: a literature review, analysis and comparison - Air Conditioning and Refrigeration Center, University of Illinois, Urbana USA (2001)

[37] McQuiston, F. C. (1978) - Heat, mass, and momentum transfer data for five plate-fin-tube heat transfer surfaces - ASHRAE Trans. 84, 266-293

[38] McQuiston, F. C. (1978) - Correlation of heat, mass, and momentum transport coefficients for plate-fin-tube heat transfer surfaces with staggered tubes - ASHRAE Trans. 109, 294-308

[39] Guillory, J. L. & F. C. McQuiston, (1973) - An Experimental Investigation of Air Dehumidification in a Parallel Plate Exchanger - ASHRAE Trans. 79, 146-151

[40] Tree, D. R. & W. A. Helmer (1976) - Experimental heat and mass transfer data for condensing flow in a parallel plate heat exchanger - ASHRAE Trans. 82, 289-299.

[41] Jacobi, A. M. & V.W. Goldschmidt (1990) - Low Reynolds number heat and mass transfer measurements of an overall counterflow, baffled, finned-tube, condensing heat exchanger - Int. J. Heat Mass Transfer 33, 755-765

[42] Korte, C. M. & A. M. Jacobi - Condensate retention and shedding effects of air-side heat exchanger performance - Master thesis, University of Illinois at Urbana-Champaign, Illinois, USA (1997)

[43] Wang, C. c., Y.C. Hsieh & Y. T. Lin (1997) - Performance of plate finned tube heat exchangers under dehumidifying conditions - J. Heat Transfer 119, 109-117

[44] Hong, K. T. & R. L. Webb, R.L. (1996) - Calculation of fin efficiency for wet and dry fins - HVAC&R Research 2, 27-41

[45] Emery, A. F. & B. L. Siegel (1990) -Experimental measurements of the effects of frost formation on heat exchanger performance," ASME - HTD 139, 1-7

[46] Rite, R. W. & R. R. Crawford - The effect of frosting on the performance of domestic refrigerator-freezer finned tube evaporator coils - ACRC TR-I, University of Illinois at Urbana-Champaign, Illinois USA (1990)

[47] Kondepudi, S. N. & D.L. O'Neal (1989) - The Performance of Finned Tube Heat Exchanger under Frosting Conditions - ASME - HTD 123, 193-200.

[48] Gardner, K. A. (1945) – Efficiency of extended surfaces – Trans. ASME 67, 621-631

[49] Schmidt, T. E. (1945) - La production calorifique des surfaces munies d'ailettes - Bulletin de l'Institut International du Froid, Annexe G-5

[50] Perrotin, T. & D. Clodic (2003) - Fin efficiency calculation in enhanced fin-and-tube heat exchangers in dry conditions – Int. Cong. of Refrigeration, Washington DC, 1-8

[51] Schmidt, T. E. (1949) - Heat Transfer Calculations for Extended Surfaces – Refrigerating Engineering 57, 351-357

[52] Park, Y.-G. & A. M. Jacobi (2011) – A simple air-side data analysis method for partially wet flat-tube heat exchangers – Heat transfer Engineering 32, 133-140.

[53] Xia, Y. & A.M. Jacobi (2005) – Air side data interpretation and performance analysis for heat exchanger with simultaneous heat and mass transfer: wet and frosted surfaces – Int. J. Heat and Mass 48, 5089-5102

[54] Wang, C.-C. (2008) – On the heat and mass analogy of fin-and-tube heat exchanger – Int. J. Heat and Mass Transfer 51, 2055-2059

[55] Pirompugd, W., C. C. Wang & S. Wongwives (2007) – Finite circular fin method for heat and mass transfer characteristics for plain fin-and-tube heat exchanger under fully and partially wet surface conditions – Int. J. Heat and Mass Transfer 50, 552-565

[56] Dopazo, J. A., J. Fernandez-Seara, F.J. Uhìa & R. Diz (2010) – Modelling and experimental validation of the hot-gas defrost process of an air-cooled evaporator – Int. J. Refrigeration 33, 829-839

[57] ARI Standard 410-81 - Forced circulation air-cooling and air-heating coils - Air Conditioning and Refrigeration Institute, 1972

[58] Ware, C. D. & T. H. Hacha (1960) - Heat transfer from humid air to fin and tube extended surface cooling coils - ASME Paper 60-HT-17

[59] Chen, L.-T. (1991) – Two-dimensional fin efficiency with combined heat and mass transfer between water-wetted fin surface and moving moist airstream – Int. J. Heat and Fluid Flow 12, 71-76

[60] Srinivasan, V. & R. K. Shah (1997) – Fin efficiency of extended surfaces in two-phase flow – Int. J. Heat and Fluid flow 18, 419-429

[61] Kim, J.S., K.-S. Lee & S.J. Yook (2009) – Frost behavior on a fin considering the heat conduction of heat exchangers fins – Int. J. Heat and Mass Transfer 52, 2581-2588

[62] Tso, C.P., Y.C. Cheng & A.C.K. Lai (2006) – An improved model for predicting performance of finned tube heat exchanger under frosting condition, with frost thickness variation along fin – Appl. Thermal Eng. 26, 111-120

[63] Getu H. M. & P. K. Bansal (2011) – New frost property correlations for a flat-finned tube heat exchanger – Int. J. Thermal Sciences 50, 544-557

[64] Cui, J., W.Z. Li & Y.S. Zhao (2010) – A new model for predicting performance of fin-and-tube heat exchanger under frost condition – Int. J. Heat and Fluid Flow 32, 249-260

[65] Rogers, R.R. & M.K. Yau – A short course in cloud physics – 3rd edition, Pergamon Press (1989)

[66] Cui, J., W.Z. Li, Y. Liu & Z.Y. Jiang (2011) – A new time and space-dependent model for predicting frost formation – Appl. Thermal Engineering 31. 447-457

[67] O'Neal, D.L. & D.R. Tree (1985) – A review of frost formation in simple geometries – ASHRAE Trans. 91, 267-281

[68] Padki, M.M., S.A. Sherif & R.M. Nelson (1989) – A simple method for modeling the frost formation phenomenon in different geometries – ASHRAE Trans. 95, 1127-1137

[69] Da Silva, D.L., C.J. Hermes & C. Melo (2010) – Experimental study of frost accumulation of fan-supplied tube-fin evaporators – Appl. Thermal Engineering 31, 1013-1020

[70] X. Jia, C.P. Tso, P. Jolly & P.K. Chia (1995) - A distributed model for prediction of the transient response of an evaporator - Int. J. Refrigeration 18, 336–342.

[71] Y. Yao, Y.Q. Jiang, S.M. Deng & Z.L. Ma (2004) - A study on the performance of the airside heat exchanger under frosting in an air source heat pump water heater/chiller unit - Int. J. Heat Mass Transfer 47, 3745–3756

[72] Lenic, K., A. Trp & B. Frankovic (2009) – Prediction of an effective cooling output of the fin-and-tube heat exchanger under frosting conditions – Appl. Thermal Eng. 29, 2534-2543

[73] Sanders C.T. – The influence of frost formation and defrosting on the performance of air coolers – Ph. D. thesis, Delft Technical University, Delft (1974)

[74] Xao, Y.X., R.W. Besant, K.S. Reykallah (2003)– A mathematical model for predicting the densification and growth of frost on a flat plate – Int. J. Heat and Mass transfer 46, 3789-3796

[75] Hayashi, Y., A. Aoki & H. Yuhana (1977) – Study on frost properties correlating with frost formation types – J. Heat transfer 6, 77 – 94.

[76] Lee, K.S., W.S. Kim & T.H. Lee (1997) – A one-dimensional model for frost formation on a cold surface - Int. J. Heat and Mass Transfer 40, 4359-4365

[77] Le Gall, R., J.M. Grillot 6 C. Jallut (1997) – Modelling of frost growth and densification – Int. J. of Heat and Mass transfer 40, 4359-4363

[78] Lenic K. – Analysis of heat and mass transfer during frost formation on a fin-and-tube heat exchanger, Ph.D. thesis, Faculty of Engineering University of Rjjeka, Rjjeka Croatia (2006)

[79] Seker, D., H. Karatas & N. Egrican (2004) – Frost formation on fin-and-tube heat exchanger. Part I – Modeling of frost formation on fin-and-tube heat exchangers – Int. J. Refrigeration 27, 367-374

[80] Bullard, C. W. & Chandrasekharan R. – Analysis of design trade-offs for display case evaporators – University of Illinois, Urbana (2004)

[81] Sherwood, T.R. & R.L. Pigford – Absorption and extraction – McGraw-Hill, New York (1956)

[82] Yonko, J. D. & C. F. Sepsy (1967) – An investigation of thermal conductivity of frost while forming on a flat horizontal plate – ASHRAE Trans. 73, 1.1 - 1.11

[83] Cengel, Y.A. & A.J. Ghajar – Heat and Mass transfer: fundamentals and applications – 4th ed. McGraw-Hill, New York (2010)

[84] Kerschbaumer, H.G. & C.H. Machielsen (1989) - Influence of frost formation and defrosting on the performance of air coolers: standards and dimensionless coefficients for the system designer – Int. J. Refrig. 12, 283–290.

[85] McKetta, J., et al. – Heat transfer design methods – Macel Dekker Inc., New York (1992)

Appendices

Appendix A - SorTech AG RCS 08 characteristics

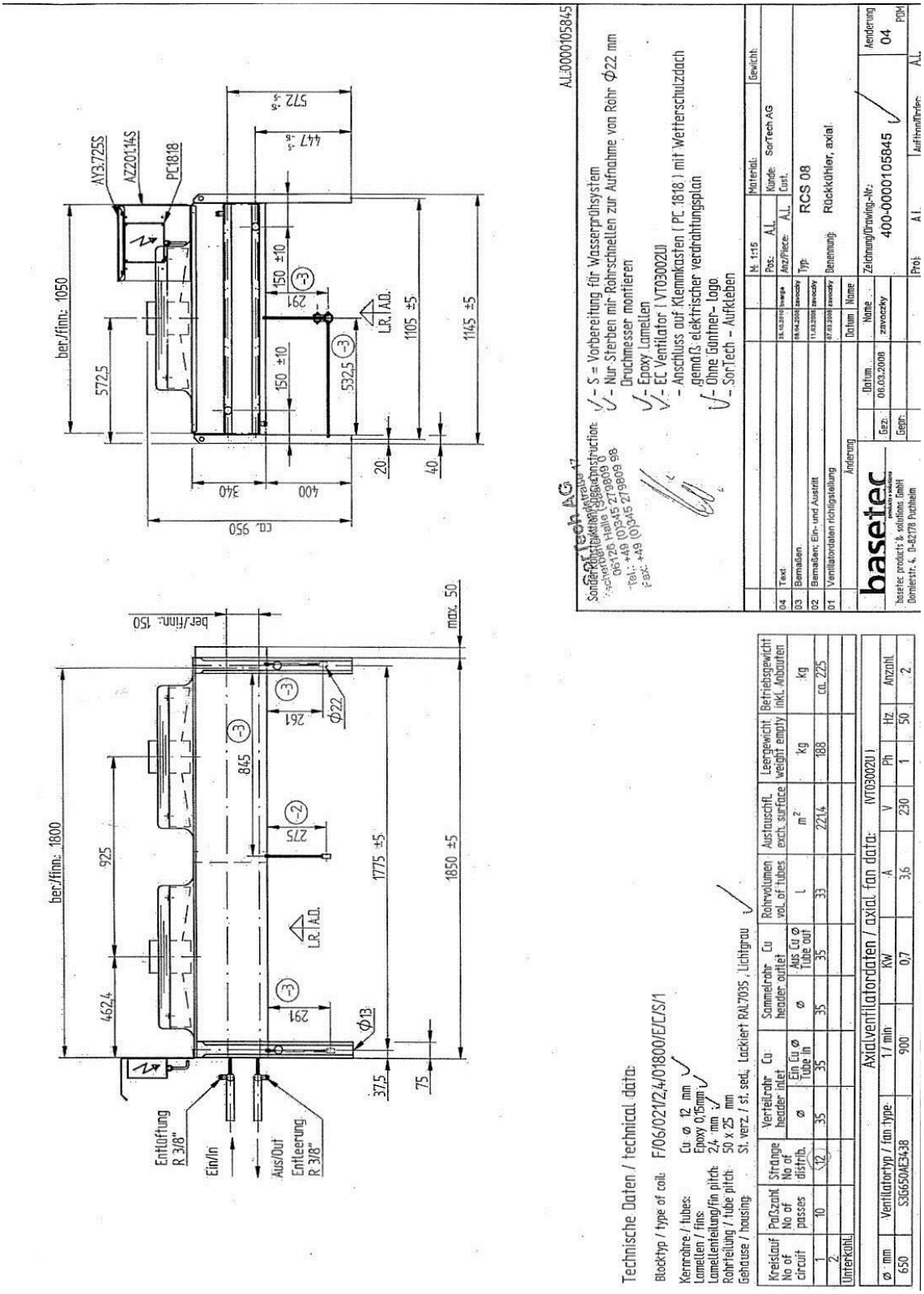

Appendix B – ε-NTU method

The ε-NTU method [B.1], is a non-dimensional method that allows to group numerous variables related to the heat performance of a heat exchanger in a smaller number of readily visualized physical significant parameters. These non-dimensional parameters are also useful in allowing a graphical representation of the heat transfer performance.

The exchanger heat transfer effectiveness ε of is defined as:

$$\varepsilon = \frac{\dot{Q}}{\dot{Q}_{max}} = \frac{C_{hot}(T_{in} - T_{out})_{hot}}{C_{min}(T_{hot,in} - T_{cold,in})} = \frac{C_{cold}(T_{out} - T_{in})_{cold}}{C_{min}(T_{hot,in} - T_{cold,in})} \quad \text{(B.1)}$$

where $\dot{Q}$ is the actual heat transfer rate and $\dot{Q}_{max}$ is the thermodynamically limited maximum heat transfer rate from one steam to the other, as would be realized only in a perfect counterflow exchanger of infinite heat transfer area. Thus, the parameter ε has the significance of effectiveness of the heat exchanger from a thermodynamic point of view. The effectiveness ε is usually expressed as function of overall number of heat transfer units NTU and the thermal capacity-rate ratio c_r through a specified flow arrangements function in the form:

$$\varepsilon = f(NTU,\ c_r, flow\ arrangement) \quad \text{(B.2)}$$

Generally this function has an asymptotic trend for a given capacity-rate ratio: the effectiveness ε approaches asymptomatically the limit imposed by the flow arrangement and thermodynamical considerations, when NTU increase from smaller to larger value.

The thermal capacity-rate C simply expresses the product of the mass flow rate $\dot{m}$ and specific heat capacity c_p of one fluid stream. The thermal capacity-rate ratio c_r and is defined as:

$$c_r = \frac{C_{min}}{C_{max}} = \frac{\min\{C_{hot},\ C_{cold}\}}{\max\{C_{hot},\ C_{cold}\}} \quad \text{(B.3)}$$

where C_{min} and C_{max} are, respectively, the smaller and the larger magnitude of the two fluids heat capacity rate C_{cold} and C_{hot}, expressed as:

$$C_{cold} = \left(\dot{m}\ c_p\right)_{cold} \quad \text{(B.4)}$$

$$C_{hot} = \left(\dot{m}\ c_p\right)_{hot} \quad \text{(B.5)}$$

The overall number of heat transfer units NTU is a non-dimensional parameter to express the heat transfer size of the exchanger. It is defined as follow:

$$NTU = \frac{\overline{U} A_{tot}}{C_{min}} \quad \text{(B.6)}$$

The last non-dimensional parameter, which provides the basis for the heat transfer aspects of exchanger design, is the flow arrangement. Typical flow arrangements are counterflow, parallel flow, parallel counterflow, crossflow and all the possible combinations of these basic arrangements.

The overall NTU can be expressed in terms of terms of the cold fluid NTU_{cold} and hot fluid NTU_{hot} numbers:

$$C_{min} = C_{cold} \qquad NTU = \frac{NTU_{cold}}{1 + \frac{NTU_{cold}}{NTU_{hot}}\left(\frac{C_{cold}}{C_{hot}}\right)} \quad \text{(B.7)}$$

or

$$C_{min} = C_{hot} \qquad NTU = \frac{NTU_{cold}}{1 + \frac{NTU_{cold}}{NTU_{hot}}\left(\frac{C_{cold}}{C_{hot}}\right)\frac{1}{c_r}} \tag{B.8}$$

where the cold fluid and the hot fluid NTU number are defined as follow:

$$NTU_{cold} = \frac{\overline{U}_{cold} A_{cold}}{C_{cold}} \tag{B.9}$$

and

$$NTU_{hot} = \frac{\overline{U}_{hot} A_{hot}}{C_{hot}} \tag{B.10}$$

The cold side heat transfer coefficient $\overline{U}_{cold}$ takes into account of the thermal resistances between cold fluid bulk condition and the cold side wall. This heat transfer coefficient refers to the cold side heat transfer area A_{cold}. Similary, the hot side heat transfer coefficient $\overline{U}_{hot}$ takes into account of the thermal resistances between hot fluid bulk condition and the cold side wall and refers to the cold side heat transfer area A_{hot}. The wall thermal resistance can be added to the cold side or the hot side heat transfer coefficient with refer to the respective heat transfer area.

Temperature-based and enthalpy-based ε-NTU methods comparison

This paragraph shows that the temperature-based ε-NTU method originally developed by Kays & London [B.1] can be described by the enthalpy-based ε-NTU method proposed by Braun et al. [B.2]. For this purpose, it is necessary that the expression of the maximal heat transfer rate $\dot{Q}_{max}$ and of the heat exchanger effectiveness ε have the same form when only sensible heat transfer occurs.

Assuming that the air stream present the minimum of the heat capacity, hence $C_{min} = C_a$, both ε-NTU methods calculate the heat transfer rate $\dot{Q}$ as:

$$\dot{Q} = \varepsilon_a \cdot \dot{Q}_{a,max} \tag{B.11}$$

The temperature-based ε-NTU method evaluates the maximal heat transfer rate that the air stream can provide $\dot{Q}_{a,max}$ as:

$$\dot{Q}_{a,max} = \dot{m}_a \cdot c_{p,a} \cdot \left(T_{a,in} - T_{w,in}\right) \tag{B.12}$$

Whereas, in the enthalpy-based ε-NTU method, the definition of $\dot{Q}_{a,max}$ involves the maximal enthalpy difference between the inlet air $i_{a,in}$ and the saturated air at the inlet water temperature $i_{sat}\left(t_{w,in}\right)$, which represent the lowest enthalpy value reachable by the air stream in a theoretical perfect heat exchanger:

$$\begin{aligned}\dot{Q}_{a,max} = \dot{m}_a \cdot \left(i_{a,in} - i_{sat}\left(T_{w,in}\right)\right) \\ = \dot{m}_a \\ \cdot \left(c_{p,da} \cdot \left(T_{a,in} - T_{w,in}\right) + i_L \cdot \left(x_{a,in} - x_{sat}\left(T_{w,in}\right)\right) + c_{p,v}\right. \\ \left. \cdot \left(x_{a,in} \cdot T_{a,in} - x_{sat}\left(T_{w,in}\right) \cdot T_{w,in}\right)\right)\end{aligned} \tag{B.13}$$

When only sensible heat transfer occurs, the air stream is not dehumidified, and the lowest enthalpy value reachable by air stream is evaluated at the inlet water temperature but at the same absolute humidity of the inlet air $x_{sat}\left(T_{w,in}\right) = x_{a,in}$.

Thus, when only sensible heat transfer is involved, the maximal heat transfer rate $\dot{Q}_{a,max}$ expressed by the enthalpy-based ε-NTU method can be rewritten in the following form:

$$\begin{aligned}\dot{Q}_{a,max} &= \dot{m}_a \cdot \left(i_{a,in} - i_{sat}(T_{w,in})\right) \\ &= \dot{m}_a \cdot \left(c_{p,da} \cdot (T_{a,in} - T_{w,in}) + x_{a,in} \cdot c_{p,v} \cdot (T_{a,in} - T_{w,in})\right)\end{aligned} \tag{B.14}$$

Under the assumption that the moist air specific heat $c_{p,a}$ can be confused with the combination of dry-air $c_{p,da}$ and vapour $c_{p,v}$ specific heats ($c_{p,da} + x_{a,in} \cdot c_{p,v} \approx c_{p,a}$), the heat transfer rate $\dot{Q}$ expressed by the enthalpy-based ε-NTU method assumes the same form provided for temperature based ε-NTU method:

$$\dot{Q}_{a,max} \approx \dot{m}_a \cdot c_{p,a} \cdot (T_{a,in} - T_{w,in}) \tag{B.15}$$

The temperature-based ε-NTU method present the air-side effectiveness ε_a as function of the overall number of heat transfer units NTU and the thermal capacity-rate ratio c_r:

$$\varepsilon_a = f(NTU, c_r) \tag{B.16}$$

Whereas, the enthalpy-based ε-NTU method uses the same expression for the air-side effectiveness ε_a and substitutes the thermal capacity-rate ratio c_r for the effective mass capacities ratio m_r:

$$\varepsilon_a = f(NTU, m_r) \tag{B.17}$$

The mass capacities ratio m_r is dependent from the effective saturation specific heat c_{sat} as reported below:

$$m_r = \frac{\dot{M}_a}{\dot{M}_w} = \frac{\dot{m}_a}{\dot{m}_w \cdot \frac{c_{p,w}}{c_{sat}}} \tag{B.18}$$

$$c_{sat} = \frac{i_{sat}(T_{w,out}) - i_{sat}(T_{w,in})}{(T_{w,out} - T_{w,in})} \tag{B.19}$$

Again, when only sensible heat transfer occurs, the air stream does not change it absolute humidity value. The enthalpy values of saturated air at the outlet $i_{sat}(T_{w,out})$ and inlet $i_{sat}(T_{w,in})$ water temperature must be substitute by the enthalpy value evaluated at the inlet air absolute humidity ($x_{sat}(T_{w,in}) = x_{sat}(T_{w,out}) = x_{a,in}$) and at the two values of temperature, $T_{w,out}$ and $T_{w,in}$, respectively. Hence, the effective saturation specific heat c_{sat} becomes:

$$c_{sat} = \frac{c_{p,da} \cdot (t_{w,out} - t_{w,in}) + x_{a,in} \cdot c_{p,v} \cdot (t_{a,out} - t_{w,in})}{(t_{w,out} - t_{w,in})} \tag{B.20}$$

By maintaining the approximation $c_{p,a} \approx c_{p,da} + x_{a,in} \cdot c_{p,v}$, results that for only sensible heat transfer, the effective saturation specific heat c_{sat} coincides with the moist air specific heat $c_{p,a}$:

$$c_{sat} = \frac{c_{p,a} \cdot (T_{w,out} - T_{w,in})}{(T_{w,out} - T_{w,in})} = c_{p,a} \tag{B.21}$$

As consequence, the expression of the effective mass capacities ratio m_r becomes the same of the thermal capacity-rate ratio c_r :

$$m_r = \frac{\dot{m}_a}{\dot{m}_w \cdot \frac{c_{p,w}}{c_{p,a}}} = \frac{\dot{m}_a \cdot c_{p,a}}{\dot{m}_w \cdot c_{p,w}} = c_r \tag{B.22}$$

Appendix C - Thermophysical properties of water

In heat pump, air conditioning and solar thermal applications, two of the most common brines are aqueous solutions of ethylene and propylene glycol. This kind of mixture combines the good heat transfer characteristics of water and increase the range of applicable temperature by reducing the freezing point (with respect to water). The typical glycol mass concentration γ in solar thermal and heat pump application is typically between 30 % and 40 %. With too low concentrations, aqueous solutions are subject to bio-organism contamination and bio-film fouling. At too high concentrations (i.e. above 60 %) the heat transfer efficiency will fall off with no additional solution freezing point decrease.

Once the type of glycol and its mass concentration are known, the thermophysical properties of the solution (called water for simplicity) can be evaluated as function of the temperature only [C.1].

Depending on the type of glycol, the water specific isobaric heat $c_{p,w}$, the inlet water thermal capacity k_w and the water dynamic viscosity μ_w are correlated to the water temperature T_w and to the glycol mass concentration γ. The properties correlations used in the model for the water and glycol solution are obtained from "Thermophysical properties of brines – Models" [C.1] by M. Conde Engineering.

The thermal conductivity k_w of the water mixture is approximated by the following relationship:

$$k_w = W_{k1} + (W_{k2}\,\gamma) + \left(W_{k3}\left(\frac{273{,}15}{T_w}\right)\right) + \left(W_{k4}\left(\frac{273{,}15}{T_w}\right)\gamma\right) + \left(W_{k5}\left(\frac{273{,}15}{T_w}\right)^2\right) \qquad \left[\frac{\mathrm{W}}{\mathrm{m\ K}}\right] \qquad \text{(C.23)}$$

The specific isobaric heat $c_{p,w}$ (or specific isobaric thermal capacity) of the aqueous solution is evaluated through the equation:

$$c_{p,w} = W_{cp1} + (W_{cp2}\,\gamma) + \left(W_{cp3}\left(\frac{273{,}15}{T_w}\right)\right) + \left(W_{cp4}\left(\frac{273{,}15}{T_w}\right)\gamma\right) + \left(W_{cp5}\left(\frac{273{,}15}{T_w}\right)^2\right) \qquad \left[\frac{\mathrm{J}}{\mathrm{kg\ K}}\right] \qquad \text{(C.24)}$$

The dynamic viscosity μ_w of the water mixture can be evaluated by the following exponential correlations:

$$\mu_w = e^{\left[W_{\mu1}+(A_{\mu2}\cdot\gamma)+\left(W_{\mu3}\left(\left(\frac{273{,}15}{T_w}\right)\right)\right)+\left(W_{\mu4}\left(\left(\frac{273{,}15}{T_w}\right)\right)\gamma\right)+\left(W_{\mu5}\left(\left(\frac{273{,}15}{T_w}\right)\right)^2\right)\right]} \qquad \left[\frac{\mathrm{kg}}{\mathrm{m\ s}}\right] \qquad \text{(C.25)}$$

The solution freezing point $T_{w,fp}$ and the pure water boiling point $T_{w,bp}$ identified the limitations of the data available and may as well represent the applicability limit of the correlation. The pure water boiling point depends on the pressure of the water inside the tubes p_w. The boiling temperature of water for atmospheric pressures can be approximated by Antoine's equation [C.2]:

$$T_{w,bp} = \frac{1730.63}{8.07131 - log_{10}(p_w)} - 233.426 \qquad [°\mathrm{C}] \qquad \text{(C.26)}$$

where p_w is expressed in Torr.

The temperature of freezing point depends upon the concentration of the solution as follows:

$$T_{w,fp} = 273{,}15\left(1 + W_{fp,1} \cdot \gamma + W_{fp,2} \cdot \gamma^2\right) \quad [\mathrm{K}] \qquad (C.27)$$

In all the previous correlations the water temperature T_w must be expressed in Kelvin. The various coefficients $W_{(prop),(order)}$ used are reported in the following table:

Table C.1 Coefficients of all correlations for aqueous solutions of ethylene glycol and of propylene glycol [C.1]

Glycol type		Freezing point temperature W_{fp}	Thermal conductivity W_k	Specific thermal capacity W_{cp}	Dynamic viscosity W_μ
Ethylene glycol	1	-0,06982	0,03818	5,36449	-4,63024
	2	0,35780	-1,37620	0,78863	-2,14817
	3	\	-0,07629	-2,59001	-12,70106
	4	\	1,07720	-2,73187	5,40536
	5	\	-0,20174	1,43759	10,58900
Propylene glycol	1	-0,03736	1,11886	4,47642	-1,0298
	2	-0,40050	-1,49110	0,60863	-10,03298
	3	\	-0,69682	-0,71497	-19,93497
	4	\	14,65802	-1,93855	14,65802
	5	\	14,62050	0,47873	14,62050

According to its definition, the Prandtl number of water is calculated as follow:

$$Pr_w = \frac{\mu_w}{k_w} c_{p,w} \qquad (C.28)$$

The next table shows the absolute and relative variations of the thermophysical properties of aqueous solution with a typical glycol mass concentration γ of 40% in the encountered temperature range (between -10 °C and 15 °C).

Table C.2 Themophysical properties variations of aqueous solution of glycol

Glycol type	Thermal conductivity variation		Specific thermal capacity variation		Dynamic viscosity variation		Prandtl number variation	
	[J/(kg K)]	[%]	[W/(m K)]	[%]	[kg/(m s)]	[%]	[-]	[%]
Propylene glycol	29	0.78	0.006	1.38	0.010	54.54	52.77	58.82
Ethylene glycol	46	1.34	0.002	0.45	0.003	44.97	21.581	44.42

It can be noted that the variations for the thermal conductivity k_w and the specific heat $c_{p,w}$ of the water-glycol mixture are really contained. Since the variations of these properties are limited, in the model they can be evaluated just at the inlet water temperature $T_{w,in}$ without introducing significant errors. The dynamic viscosity μ_w and consequently the Prandtl number Pr_w present higher variability in the considered temperature range. Since in the model these properties are evaluated just to calculate the internal convective heat transfer coefficient h_i, it is more significant to quantify their effects on this coefficient more than their actual values.

For a typical water mass flow rate $\dot{m}_w$ of 1200 kg/h, the error introduced on the internal convective heat transfer coefficient h_i by evaluating the thermophysical properties at the inlet temperature is always below 1.5 %. (The internal convective heat transfer coefficient is calculated as reported in chapter 5). Furthermore it has to be considered that the usual difference between the inlet $T_{w,in}$ and outlet $T_{w,out}$ water temperature is in most of the cases below 5 K. Hence, also the dynamic viscosity μ_w can be evaluated just once at the inlet water temperature $T_{w,in}$ without introducing significant errors in the model.

Appendix D - Thermophysical properties of air

In the model the atmospheric air is treated as binary mixture of air and water vapour. According to Kröger [D.1], the thermophysical properties of moist air can be evaluated as combination between the dry air and the water vapour properties.

The correlations used in the model to evaluate the air thermophysical properties are taken from the appendix A in the second volume of Kröger work "*Air cooled heat exchangers and cooling tower: thermal-flow performance evaluation and design*" [D.1].

The air specific isobaric heat $c_{p,a}$, the thermal conductivity k_a and the dynamic viscosity μ_a resul

$$c_{p,a} = \frac{c_{p,da} + x_a c_{p,v}}{1 + x_a} \qquad \left[\frac{\mathrm{J}}{\mathrm{kg\ K}}\right] \qquad \text{(D.1)}$$

$$k_a = \frac{\left(\frac{1}{1+1608\,x_a}\right) k_{da} MW_{da}^{1/3} + \left(\frac{x_a}{x_a+0.622}\right) k_v MW_v^{1/3}}{\left(\frac{1}{1+1608\,x_a}\right) MW_{da}^{1/3} + \left(\frac{x_a}{x_a+0.622}\right) MW_v^{1/3}} \qquad \left[\frac{\mathrm{W}}{\mathrm{m\ K}}\right] \qquad \text{(D.2)}$$

$$\mu_a = \frac{\left(\frac{1}{1+1608\,x_a}\right) \mu_{da} MW_{da}^{1/2} + \left(\frac{x_a}{x_a+0.622}\right) \mu_v MW_v^{1/2}}{\left(\frac{1}{1+1608\,x_a}\right) MW_{da}^{1/2} + \left(\frac{x_a}{x_a+0.622}\right) MW_v^{1/2}} \qquad \left[\frac{\mathrm{kg}}{\mathrm{m\ s}}\right] \qquad \text{(D.3)}$$

At least the density of the humid air can be evaluated with the following correlation:

$$\rho_a = \left(1 - \frac{x_a}{x_a + 0.62198}\right)(1 + x_a)\frac{p_a}{287.08\,T_a} \qquad \left[\frac{\mathrm{kg}}{\mathrm{m^3}}\right] \qquad \text{(D.4)}$$

where the air pressure p_a must be expressed in Pa.

The dry air specific isobaric heat $c_{p,da}$, the thermal conductivity k_{da} and the dynamic viscosity μ_{da} are calculated as polynomial functions of the absolute air dry-bulb temperature T_a:

$$c_{p,da} = A_{cp,1} + A_{cp,2} \cdot T_a + A_{cp,3} \cdot T_a^2 + A_{cp,4} \cdot T_a^3 \qquad \left[\frac{\mathrm{J}}{\mathrm{kg\ K}}\right] \qquad \text{(D.5)}$$

$$k_{da} = A_{k,1} + A_{k,2} \cdot T_a + A_{k,3} \cdot T_a^2 + A_{k,4} \cdot T_a^3 \qquad \left[\frac{\mathrm{W}}{\mathrm{m\ K}}\right] \qquad \text{(D.6)}$$

$$\mu_{da} = A_{\mu,1} + A_{\mu,2} \cdot T_a + A_{\mu,3} \cdot T_a^2 + A_{\mu,4} \cdot T_a^3 \qquad \left[\frac{\mathrm{kg}}{\mathrm{m\ s}}\right] \qquad \text{(D.7)}$$

where the coefficients $A_{(prop),(order)}$ are reported in the next table:

Table D.1 Coefficients of all correlations for dry air [D.1].

	Specific thermal capacity	Thermal conductivity	Dynamic viscosity
	A_{cp}	A_k	A_μ
1	$1.04536 \cdot 10^{3}$	$-4.937787 \cdot 10^{-4}$	$2.287973 \cdot 10^{-6}$
2	$-3.161783 \cdot 10^{-1}$	$1.018087 \cdot 10^{-4}$	$6.259793 \cdot 10^{-8}$
3	$7.083814 \cdot 10^{-4}$	$-4.627937 \cdot 10^{-8}$	$-3.131956 \cdot 10^{-11}$
4	$-2.705209 \cdot 10^{-7}$	$1.250603 \cdot 10^{-11}$	$8.15038 \cdot 10^{-15}$

These correlations are valid for dry air at standard atmospheric pressure (101325 Pa) and a temperature restrained between 220 K (-53.15°C) and 380 K (106.15°C).

At the same way, the water vapour specific isobaric heat $c_{p,v}$, the thermal conductivity k_v and the dynamic viscosity μ_v are calculated as polynomial functions of the absolute air dry-bulb temperature T_a:

$$c_{p,v} = V_{cp,1} + V_{cp,2} \cdot T_a + V_{cp,3} \cdot T_a^5 + V_{cp,4} \cdot T_a^6 \quad \left[\frac{\mathrm{J}}{\mathrm{kg\ K}}\right] \quad \text{(D.8)}$$

$$k_v = V_{k,1} + V_{k,2} \cdot T_a + V_{k,3} \cdot T_a^2 + V_{k,4} \cdot T_a^3 \quad \left[\frac{\mathrm{W}}{\mathrm{m\ K}}\right] \quad \text{(D.9)}$$

$$\mu_v = V_{\mu,1} + V_{\mu,2} \cdot T_a + V_{\mu,3} \cdot T_a^2 + V_{\mu,4} \cdot T_a^3 \quad \left[\frac{\mathrm{kg}}{\mathrm{m\ s}}\right] \quad \text{(D.10)}$$

where the coefficients $V_{(prop),(order)}$ are reported in the next table:

Table D.2 Coefficients of all correlations for water vapour [D.1].

	Specific thermal capacity	Thermal conductivity	Dynamic viscosity
	V_{cp}	V_k	V_μ
1	$1.3605 \cdot 10^{3}$	$1.3046 \cdot 10^{-2}$	$2.562435 \cdot 10^{-6}$
2	2.31334	$-3.756191 \cdot 10^{-5}$	$1.816683 \cdot 10^{-8}$
3	$-2.46784 \cdot 10^{-10}$	$-2.217964 \cdot 10^{-7}$	$2.579066 \cdot 10^{-11}$
4	$+5.91332 \cdot 10^{-13}$	$-1.11562 \cdot 10^{-10}$	$-1.067299 \cdot 10^{-14}$

These correlations are valid for dry air at standard atmospheric pressure (101325 Pa) and a temperature restrained between 273.15 K (0°C) and 380 K (106.15°C). –In the model these correlation are extended to the whole range of encountered temperatures.

The air Prandtl number Pr_a is then simply calculated by applying its definition:

$$Pr_a = \frac{\mu_a}{k_a} c_{p,a} \tag{D.11}$$

The dew-point temperature $T_{a,dp}$ is the temperature at which water vapour condensation first occurs at the same pressure and (absolute) humidity content, when cooling a given sample of moist air. In the model the dew-point temperature $T_{a,dp}$ is evaluated with the "*Psychrometrics"* subroutine.

The air frost-point temperature $T_{a,fp}$ is the temperature under which the condensed vapour contained in the humid air starts to freeze. Its value coincides with the water freezing-point temperature. In the model the frost-point temperature $T_{a,fp}$ is evaluated at the atmospheric pressure p_a through the correlation given by Zemansky & Dittman [D.2]:

$$T_{a,fp} = T_{w,tp}\left(1 - \frac{p_a - p_{w,tp}}{3950 \cdot 10^5}\right)^{1/9} \quad [\mathrm{K}] \tag{D.12}$$

where $T_{w,tp}$ and $p_{w,tp}$ are the triple-point water temperature (273,16 K, 0,01 °C) and triple-point water pressure (611.2 Pa), respectively.

It can be noted that in winter, the presence of water vapour in the atmospheric air doesn't affect significantly the thermophysical properties of air like specific heat, thermal conductivity and dynamic viscosity. Its effect is negligible, because the ratio between vapour mass and dry air mass contained is limited in the order of 1/1000 even at high relative humidity. Thus, the water vapour contribution at the thermophysical properties of the moist air is really low. As consequence the values of moist air properties in this condition are really closed to those of the dry air.

The moist air properties variations along the typical winter air temperature range from -10 °C to 20 °C are really restrained. The relative difference of the dry air specific heat $c_{p,a}$ is always far below 1 %.

Furthermore, in practice the temperature difference between inlet and outlet air results usually around few Kelvin. Hence, the model evaluates the air properties as function of the only inlet air temperature $T_{a,in}$ and absolute humidity $x_{a,in}$. These calculated values are considered constant for the entire air stream.

The fans present on the Sortech AG RCS 08 at the maximal allowed fan rotational speed, can elaborate a total volumetric air flow rate around 16000 m^3/s. At this flow rate, assuming constant properties of air leads to a maximal error on the external convective heat transfer coefficient h_o below 5 %. (The external convective heat transfer coefficient is calculated as reported in chapter 2).

Appendices literature reference

[B.1] Kays, W. M. & A. L. London – Compact Heat exchangers – 3rd ed., Krieger Publishing Company, Malabar (1994)

[B.2] Braun, J.E., S.A Klein & T.W. Mitchell (1989)– Effectiveness models for cooling towers and cooling coil – ASHRAE Trans. 99, 164-174

[C.1] M. Conde Engineering – Thermophysical properties of brines. Models - Zurich (2011).

[C.2] Antoine, C. (188) – Tensions des vapeurs; nouvelle realation entre les tensions e les températurs – Comptes Rendus des Séances de l'Académie des Sciences 107, 681-684, 778-780, 836-837

[D.1] Kröger, D. G. – Air cooled heat exchangers and cooling tower: thermal-flow performance evaluation and design – PennWell Corporation, Tulsa (2004).

[D.2] Zemansky, M. W. & R. H. Dittman - Heat and thermodynamics : an intermediate textbook - 7th Ed. McGraw-Hill, New York, London (1997)